The Role of Organics in the Chemical Composition and Reactivity at the Surface of Halide Solutions Relevant for Marine Aerosol or Ocean Surface Water

Inauguraldissertation
der Philosophisch-naturwissenschaftlichen Fakultät
der Universität Bern

vorgelegt von
Ming-Tao Lee
aus Taiwan Chinesisches Taipei

Leiter der Arbeit:
Prof. Dr. Andreas Türler
Departement für Chemie und Biochemie

The Role of Organics in the Chemical Composition and Reactivity at the Surface of Halide Solutions Relevant for Marine Aerosol or Ocean Surface Water

Inauguraldissertation
der Philosophisch-naturwissenschaftlichen Fakultät
der Universität Bern

vorgelegt von
Ming-Tao Lee
aus Taiwan Chinesisches Taipei

Leiter der Arbeit:
Prof. Dr. Andreas Türler
Departement für Chemie und Biochemie

Von der Philosophisch-naturwissenschaftlichen Fakultät angenommen.

Bern, 30.10.2015

Der Dekan:

Prof. Dr. Gilberto Colangelo

What is matter? —Never mind. What is mind? —No matter.
— Thomas Hewitt Key

u^b

b
UNIVERSITÄT
BERN

Anmeldung zur Doktorprüfung

Vorname: Ming-Tao   Name: Lee

Heimatort: Taiwan   Geburtsdatum: 19.10.1982

Matrikelnummer: 11-118-734

Adresse: Birkenstrasse 5, 5210 Windisch

Titel der Dissertation: The Role of Organics in the Chemical Composition and Reactivity at the Surface of Halide Solutions Relevant for Marine Aerosol or Ocean Surface Water

Hauptfach: Chemie und Molekulare Wissenschaften

Leiter der Dissertation: Prof. A. Türler

Koreferent: Prof. H. Bluhm

Vorsitz: Prof. M. Albrecht

PrüfendeR 1: Prof. M. Albrecht
PrüfendeR 2: Prof. A. Türler
PrüfendeR 3: Prof. M. Ammann
Ausweis in: dt. und engl.

Anmeldung: 14.08.2015

Prüfungsort: DCB, S379

Prüfungsdatum: 30.10.2015

Prüfungszeit: 14:00

Prüfungsart: Vortrag

Dissertation, Referat und Koreferat fällig bis: 06.10.2015

Abstract

Oceans cover approximately 71% of the Earth's surface and are playing a key role in climate regulation via a large number of physical and chemical processes. Seawater constitutes a complex aqueous electrolyte with an average salt concentration of 0.5 molar, the dominant ionic solutes being Na^+ and Cl^- (followed by Mg^{2+}, SO^{4-}, Br^-, and I^- to mention a few). While present in much lower concentrations, organic materials are highly important in affecting the surface-specific chemistry of sea-water aqueous systems, given their high surface propensity. The overall aim of the present project is to develop a detailed insight into the behavior of sodium halide species at mixed organic/aqueous liquid surfaces. Specific goals include: Firstly, establishing an understanding of the interplay of sodium halide ions and organic solutes at the air-water interface at a molecular level. The primary approach to achieve these goals will be to perform synchrotron-based studies using near-ambient pressure X-ray photoelectron spectroscopy, at the Swiss Light Source. Secondly, laboratory experiments related to the structure and heterogeneous reactivity of aqueous halide solutions in the context of atmospheric chemistry in marine environments and further investigations on how such surface reactions are affected by the presence of various relevant organic compounds.

Thesis outline

The scope of the thesis was to give a detailed look into ion behavior at mixed organic/aqueous liquid-vapor interfaces both from the perspective of surface sensitive spectroscopy and the perspective of chemical reactivity. This is crucial for understanding the chemistry at the ocean surface or at and within sea spray particles on a molecular level. The reaction of ozone (O_3) with bromide (Br^-) is used as a probe reaction for assessing interfacial reactivity. Aspects of the kinetics of this reaction, and especially its enhanced kinetics at the surface, are still open to debate. To better understand the interface of the marine boundary layer including the phenomenon of surface enhancement of halides, an important aspect of organics may be that they compete for surface sites with the halide ions at the interface.

In this thesis we would like to better understand the heterogeneous kinetics of the reaction of O_3 with Br^- and especially explore the presence of a surface reaction and the way it is affected by relevant organics. Assessing a surface reaction requires probing the surface, even though in the field of atmospheric chemistry this assessment has been traditionally done by looking at the kinetics of gas uptake alone. For the first time, the aim is measuring the composition of inorganic and/or organic aqueous solutions at the aqueous solution−vapor interface. Our choice of measurement technique has fallen on liquid microjet (LJ) XPS. These aspects are discussed in more detail in Chapter 1, which serves as the introduction into this thesis. Part of the material presented therein has been published in papers II and III.

Chapter 2 introduces the LJ-XPS/UPS technique, as well as the design of the Near Ambient Pressure Photoemission (NAPP) endstation (Paper I), and proof-of-principle measurements are described (taken from Papers I and II). Also, the experimental setup for experiments addressing the heterogeneous kinetics of O_3 using a newly developed flow reactor is shown.

Chapter 3 examines the liquid−vapor interface for mixtures of water, sodium chloride, and formic acid, an abundant chemical in the atmosphere. The results of LJ-XPS were compared with surface tension measurements over a wide range of formic acid concentrations (Paper III).

Chapter 4 exploited the liquid−vapor interface for mixtures of water and short chains alcohols or small carboxylic acids (C1-C4), abundant chemicals in the atmosphere. The results of LJ-XPS measurements for all species at 0.5 M bulk concentration were compared with surface tension measurements from the literature (Paper IV).

Chapter 5 covers the investigation into complementary kinetic and LJ-XPS experiments to directly assess the interplay between bromide ions and citric acid and the effect it potentially has on the kinetics of the reaction between O_3 and Br^- in an environment that has relevance for the ocean surface or sea spray particles (Paper V).

Chapter 6, investigates the relative difference with which a carboxylic acid, i.e., butyric acid, or an alcohol, i.e., 1-butanol, surfactants affect the presence of halide ions (bromide, Br^-, and iodide, I^-) and sodium cations (Na^+) at the aqueous liquid−vapor interface. The relevance comes from the importance of the surface chemistry of sea-spray aerosol particles in atmospheric chemistry. Molecular dynamics (MD) simulations of butyric acid and 1-butanol in an aqueous electrolyte solution are used to develop a detailed understanding of the ion-solvent-surfactant interactions in the interfacial region (Paper VI).

Finally, Chapter 7 contains a summary of the experimental achievements, with an outlook to future experiments.

List of Papers

This thesis is based on the following papers, which are referred to in the text by their Roman numbers.

I **A new endstation at the Swiss Light Source for ultraviolet photoelectron spectroscopy, X-ray photoelectron spectroscopy, and X-ray absorption spectroscopy measurements of liquid solutions**
M.A. Brown, A. Beloqui Redondo, I. Jordan, N. Duyckaerts,
M.-T. Lee, M. Ammann, F.Nolting, A. Kleibert, T. Huthwelker, J.-P. Machler,
M. Birrer, J. Honegger, R. Wetter, H.J. Wörner, J.A. van Bokhoven
Review of Scientific Instruments 2013, 84, 073904.

II **Ion spatial distributions at the air- and vacuum-aqueous K_2CO_3 interfaces**
M.A. Brown, M.-T. Lee, A. Kleibert, M. Ammann, J.B. Giorgi
Journal of Physical Chemistry C 2015, 119, 4976-4982.

III **The liquid-vapor interface of formic acid solutions in salt water: A comparison of macroscopic surface tension and microscopic X-ray photoelectron spectroscopy measurements**
J.G. Pruyne, M.-T. Lee, C. Fábri, A. Beloqui Redondo, A. Kleibert,
M. Ammann, M.A. Brown,* M.J. Krisch
Journal of Physical Chemistry C 2014, 118, 29350-29360.

IV **Quantifying the Affinity of C1-C4 Oxygenated Volatile Organic Compounds for the Air−Water Interface using Liquid jet XPS**
M.-T. Lee, M. Ammann, D. J. Donaldson, M. A. Brown
Manuscript in preparation

V **The competition between organics and bromide at the aqueous solution-air interface as seen from O_3 uptake kinetics and X-ray photoelectron spectroscopy**
M.-T. Lee, M.A. Brown, S. Kato, A. Kleibert, A. Türler, M. Ammann
Journal of Physical Chemistry A 2015,119, 4600-4608.

VI **Contrasting the effect of an alcohol and a carboxylic acid surfactant on the ion distribution at the aqueous solution−air interface**
M.-T. Lee, F. Orlando, M. Khabiri, S. Kato, A. Kleibert, M. A. Brown, A. Türler, M. Roselova, M. Ammann
Manuscript in preparation

The following is a list of publications to which I have contributed to but which will not to be covered in this thesis.

1 **Quantitative depth profiling of Ce^{3+} in Pt/CeO$_2$ by *in situ* high-energy XPS in a hydrogen atmosphere**
S. Kato, M. Ammann, T. Huthwelker, C. Paun, M. Lampimäki, M.-T. Lee, M. Rothensteiner, J. A. van Bokhoven
Phys. Chem. Chem. Phys., 2015, **17**, 5078-5083

2 **A new *in situ* cell for near-ambient pressure XPS and electron yield NEXAFS of environmental oxide and frozen solution surfaces**
F. Orlando, A. Waldner, T. Bartels-Rausch, M. Birrer, M.-T. Lee, C. Proff, T. Huthwelker, A. Kleibert, J. A. van Bokhoven, M. Ammann
Revision submitted to Topics in Catalysis

Table of Contents

Chapter 1

1. Introduction

1.1. Ozone and halogen chemistry

Ozone (O_3) is a gas that is naturally present in our atmosphere. Each O_3 molecule contains three atoms of oxygen and is denoted chemically as O_3. O_3 is found primarily in two regions of the atmosphere. About 90% of atmospheric O_3 is in the stratosphere; there are typically a few O_3 molecules for every million air molecules (ppm). O_3 is produced naturally when highly energetic solar radiation breaks molecules of oxygen, O_2, and gives rise to two oxygen atoms (O + O) to split apart in a process called photolysis. The large amount of O_3 in the stratosphere is often referred to as the "O_3 layer". This O_3 layer absorbs a large part of the Sun's biologically harmful ultra-violet (UV) rays and protects life on Earth. The destruction of O_3 occurs as quickly as O_3 is formed. Under natural conditions there is a balance between the formation and destruction of O_3 molecules in the stratosphere. In the 1970s it was discovered that human-made chemicals, which are called chlorofluorocarbons (CFCs), are inducing a net destruction of O_3 in the stratosphere, thus strongly affecting the O_3 budget of the natural stratosphere. This O_3 loss is considered to be related to chlorine and bromine in the stratosphere deriving from human-produced CFCs (Seinfeld and Pandis 1998).

Meanwhile, ground-level O_3 occurs at concentrations from about 20 parts per billion (ppb) in clean marine air to more than 200 ppb in polluted urban air masses (Alvarez, Senff et al. 2011). In the troposphere, O_3 is formed as a result of photochemical processes induced by sunlight as well. While photolysis of O_2 is not possible in the troposphere, sunlight splits nitrogen dioxide (NO_2) into nitric oxide (NO) and an oxygen atom (O). Therefore NO_2 provides the oxygen atom (O) source, which is free to react with an oxygen molecule (O_2) for O_3 formation. Then, O_3 reacts with NO to create NO_2 and O_2. This process occurs naturally and does not result in a net gain of O_3. However, the production of additional O_3 precursors, NO, NO_2, and volatile organic compounds (VOC) by human activity contributes to elevated

levels of O_3 in the troposphere (Finlayson-Pitts and Pitts 1993). The increase of ground-level O_3 may cause adverse effects to human health and ecosystem (Bell, McDermott et al. 2004).

Halogen chemistry is well known for its role in O_3 destruction in the stratosphere; however halogens (e.g. Br atoms and BrO) play also a critical role in the chemistry of the troposphere that is not understood in detail. Read et al. used box model calculations to try to interpret their observations of O_3 concentration and its diurnal variation in the marine boundary layer at the Cape Verde islands (Read, Mahajan et al. 2008). They found that if halogens are excluded from the reaction scheme of the box model the computational results underestimate the total O_3 loss by half and the O_3 concentrations by 12% (annual averages).

Halogens are species containing Cl, Br or I. Halogen species are of significant interest in the atmospheric chemistry of the marine boundary layer. An outline of how halogen release and related O_3 depletion occurs above the sea is shown in Fig. 1.1. By the action of oxidants, halide ions (chloride, Cl^-; bromide, Br^-; iodide, I^-) present in sea water and in sea spray aerosol can be converted into gas phase species such as molecular halogens (Cl_2, Br_2, I_2, and interhalogen compounds such as BrCl). These molecular halogen compounds represent a source of reactive halogen atoms upon photolysis which is of importance for I, Br and to a minor extent Cl. Chlorine atoms typically react extremely efficiently with hydrocarbons, reducing their impact on tropospheric O_3 destruction (Simpson, von Glasow et al. 2007). Other sources of Br and I atoms maybe brominated and iodinated organic compounds including $CHBr_3$, CH_2I_2, CH_3I respectively (part **b** in Fig. 1.1). They predominantly originate from macro algae (seaweed) and micro algae (phytoplankton), which produce organic bromine and iodine species. Both brominated and iodinated organic compounds usually have a short life time, such that they are emitted into the gas phase and are readily photolysed to produce Br and I atoms. These are implicated in catalytic cycles affecting the O_3 budget of the marine boundary layer (MBL) (Foster, Plastridge et al. 2001, Simpson, von Glasow et al. 2007, Saiz-Lopez, Lamarque et al. 2012), as shown in Fig. 1.1. Therefore, they play a major role in the chemistry and oxidizing capacity of the troposphere. In turn, most of the chlorinated organic compounds of marine origin are longer lived halocarbons, which will not be photolysed in the troposphere, but will be transported to the stratosphere and influence stratospheric O_3 levels (Saiz-Lopez and Plane 2004). They are similar to manmade CFCs and their substitutes to initiate O_3 destruction cycles there.
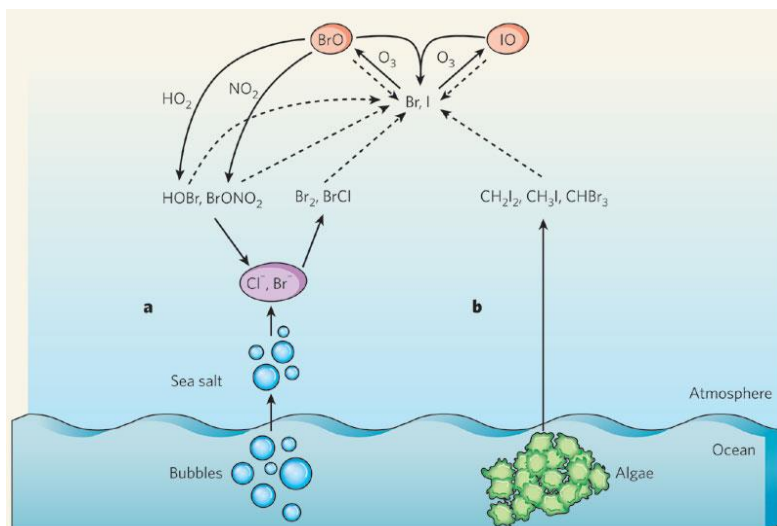
Fig. 1.1. Halogen release and related ozone depletion above the sea. Part a, Sea water contains dissolved chloride and bromide salts that are released into the air in droplets of spray. Solid arrows indicate the dark reactions, and dotted arrows indicate photolysis reactions (will be discussed in the text). Part b, Marine algae produce halogenated species, e.g iodinated organic molecules that are broken by sunlight to generate iodine atoms (I). To be simple, not all possible reactions are discussed nor shown. Figure is adapted from (von Glasow 2008).

1.1.1. Reactive halogen species (RHS) and ozone depletion event (ODE)

Reactive Halogen Species (RHS) cause so-called O_3 depletion events (ODE) in the troposphere through auto-catalytic reactions (Simpson, von Glasow et al. 2007). The main reactions of RHS, and in particular the halogen oxides BrO and IO, in the catalytic reaction cycles, in which halogens destroy O_3, are shown below (denoted by X and Y, where X, Y present Cl, Br, or I):

$$X + O_3 \rightarrow XO + O_2 \tag{1.1}$$

$$Y + O_3 \rightarrow YO + O_2 \tag{1.2}$$

$$XO + YO \rightarrow X + Y + O_2 \tag{1.3}$$

Net: $2O_3 \rightarrow 3O_2$
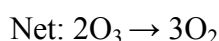
Reaction (1.3) can have other reactive product channels:

$$XO + YO \rightarrow X + Y + O_2$$

$$\rightarrow XY + O_2$$

$$\rightarrow OXO + Y \qquad (1.4)$$
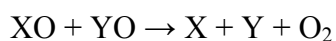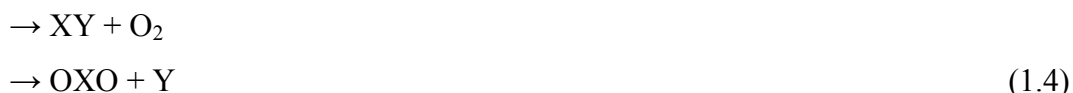
Especially, it would be pointed out the case of $X = Br$, where the major channel (around 85% at room temperature) of the BrO self-reaction produces a pair of Br atoms, the minor one produces Br_2, on the other hand the major products of $BrO + IO$ reaction are OIO and Br and with less $I + Br$ (Atkinson, Baulch et al. 2006). Therefore, the net rates of O_3 loss by reaction (1.3) and the fallowing reactions depend on the halogen species involved. Combining reaction (1.1) with (1.4) forms a catalytic cycle destroying O_3 based on recycling of the halogens by the cross reaction (1.4).

The sequence of another O_3 destruction scheme relates reactions of halogen oxides with HO_2 are shown as following:

$$X + O_3 \rightarrow XO + O_2 \qquad (1.5)$$

$$XO + HO_2 \rightarrow HOX + O_2 \qquad (1.6)$$

$$HOX + hv \rightarrow X + OH \qquad (1.7)$$

$$OH + CO + O_2 \rightarrow CO_2 + HO_2 \qquad (1.8)$$

Net: $CO + O_3 \rightarrow CO_2 + O_2$
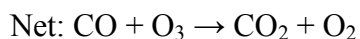
However, all three types of reaction cycles mentioned above including self-reaction (XO+XO), inter-halogen (cross) reaction (XO+YO), and XO+HO_2 do not grow the reactive capital of halogen atoms (X and Y) and halogen oxides (XO and YO) in the atmosphere.

1.1.2. Bromine explosion
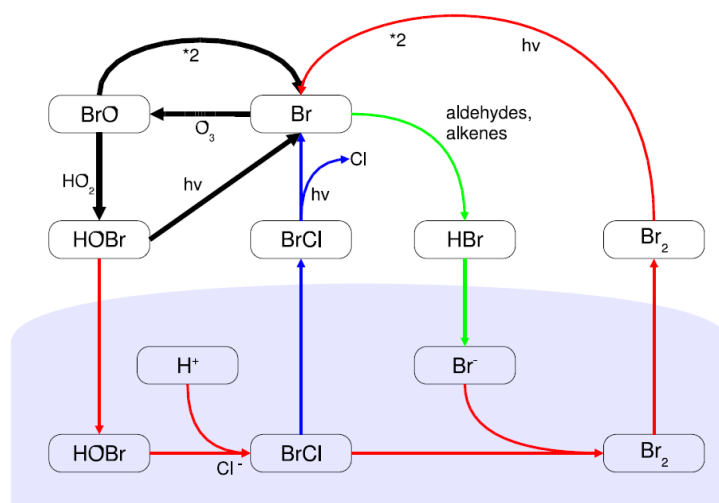
Fig. 1.2. A simplified representation of bromine explosion reactions. The blue zone at the bottom represents the condensed phase (liquid sea-water or ice surface). Figure is adapted from (Simpson, von Glasow et al. 2007).

A special sequence of chemical reactions can produce more reactive halogen gases. This special sequence is called the "*bromine explosion*" reaction sequence, see also Fig. 1.2., which is thought be the origin of the majority of reactive halogens during O_3 depletion events (Fan and Jacob 1992, McConnell, Henderson et al. 1992, Tang and McConnell 1996, Wennberg 1999) The bromine explosion sequence is:

$$HOBr + Br^- + H^+ \xrightarrow{\quad mp \quad} H_2O + Br_2 \tag{1.9}$$

$$Br_2 + hv \rightarrow 2Br \tag{1.10}$$

$$Br + O_3 \rightarrow BrO + O_2 \tag{1.11}$$

$$BrO + HO_2 \rightarrow HOBr + O_2 \tag{1.12}$$

Net: $H^+ + Br^- + HO_2 + O_3 \xrightarrow{\quad mp, hv \quad} Br + H_2O + 2O_2$
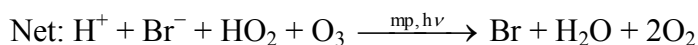
Bromide (Br^-) which is most often derived from sea salt particles and present in solution or on ice surfaces is the source of reactive bromine. In the case of the reactions happening in liquid brine solution, then reaction (1.9) would consist of three sub-reactions. They are HOBr gas uptake to the brine solution, the reaction taking place in brine solution, and degassing of dissolved Br_2 gas. The multiphase reaction cycle is shown in reaction (1.9) by the abbreviation "mp", emphasizing its importance. It is important to note that this sequence of

reactions is autocatalytic which consumes Br$^-$, HO$_x$, and protons (H$^+$). Alternatively, one can neglect the net reaction above, but consider a stock of inactive (e.g. Br$^-$) and reactive bromine species. It means that HOBr may recycle into gas-phase Br$_2$, which will become the precursor of two reactive bromine species (two Br atoms), via condensed-phase interactions. Therefore, one BrOx molecule eventually can be converted rapidly into two by way of oxidizing Br$^-$ at the surface e.g. of brine, sea salt particles, sea ice, or snow (McConnell, Henderson et al. 1992, Mozurkewich 1995, Sander and Crutzen 1996, Tang and McConnell 1996, Vogt, Crutzen et al. 1996, Michalowski, Francisco et al. 2000). This procedure gives rise to an exponential increase of the BrO concentration in the gas phase, to justify the term bromine explosion (Platt and Janssen 1995, Wennberg 1999).

1.2. The kinetics of ozone with bromide ions in aqueous phase

Bromine explosion was proposed to start from the consumption of HOBr (reaction 1.9), and of HOBr by the HO$_2$+BrO (reaction 1.12) to close the reaction cycle. However, light is needed for the production of HO$_2$ through gas phase photochemistry. Therefore, the reaction of O$_3$ with Br$^-$ provides a dark source of HOBr. The reaction of gaseous O$_3$ with Br$^-$containing solutions has been studied before (Haag and Hoigne 1983, Liu, Schurter et al. 2001). In its simplified form, the mechanism is thought to be:

$$O_3 + Br^- + H_2O \rightarrow HOBr + O_2 + OH^- \hspace{4cm} (1.13)$$

$$HOBr + Br^- + H^+ \rightarrow Br_2 + H_2O \hspace{4.5cm} (1.14)$$

The reactions of O$_3$ with Br$^-$ and I$^-$ ions are believed be one of the significant sources of gas phase halogen compounds (Simpson, von Glasow et al. 2007, Carpenter, MacDonald et al. 2013). In a first step, these reactions lead to HOBr and HOI, respectively, which then react further with halide ions to form BrCl or Br$_2$ and ICl or I$_2$, respectively. It is recognized that O$_3$ oxidizes dissolved Br$^-$ ions to HOBr, which then reacts with HBr to produce molecular bromine (Br$_2$) in the aqueous phase. The following step is degassing of the dissolved Br$_2$ into the gas phase. On the one hand, the reaction between O$_3$ and Br$^-$ in solution is well-investigated; however, the reaction in the bulk aqueous phase is fairly slow and HOBr production would not be sufficient to explain observed initial halogen release rates. However, several studies, discuseed in more detail below, have postulated an enhanced rate of this

reaction at the liquid−vapor interface, which would render it an important pathway of halide oxidation.

1.2.1. Surface reactions

Several studies have suggested the involvement of surface specific reactions of O_3 with aqueous Br^- containing solutions (Hunt, Roeselova et al. 2004, Clifford and Donaldson 2007, Oldridge and Abbatt 2011). Hunt et al. has proposed that the Br_2-production-reaction of O_3 with Br^- is taking place at the liquid−vapor interface rather than in the bulk aqueous solution, because the known bulk kinetics would not be sufficient to explain the observations. Another hint was coming from the saturating behavior of the rate of pH increase (consumption of protons in the reaction) as a function of the Br^- concentration at high (M) Br^- concentrations, as indicated by a Langmuir-Hinshelwood (see below) type dependence of the rate on aqueous-phase Br^- concentration (Clifford and Donaldson 2007) under conditions relevant for sea salt aerosols. The most convincing argument was based on the negative dependence of the Br_2 production rate of the O_3 concentration at low Br^- concentration relevant for ocean water (Oldridge and Abbatt 2011). This negative dependence on O_3 can be interpreted in terms of Langmuir-Hinshelwood kinetics, a classical surface reaction mechanism between adsorbed species, which will be discussed in more detail (Ammann, Cox et al. 2013).

1.2.2. Ozone kinetics as affected by organic compounds

The ocean surface water and sea spray aerosol derived thus contain a complex mixture of not only inorganic salts but also organic compounds deriving from marine biota (O'Dowd, Facchini et al. 2004, Kanakidou, Seinfeld et al. 2005, Vignati, Facchini et al. 2010, Donaldson and George 2012). It has been known that organic compounds including amino acids, fatty acids, fatty alcohols, sterols and polysaccharides are enriched in the sea-surface microlayer (SSM), which is the thin interfacial zone (1-1000 μm thickness) at the sea-atmosphere interface. Furthermore, studies point to a significant enrichment of these organics in aerosol particles generated via a variety of processes at the sea surface (Donaldson and Vaida 2006, Keene, Maring et al. 2007). In the context of this thesis, an important aspect of organics is that they may have a significant effect on the way halide ions are distributed at the interface (Krisch, D'Auria et al. 2007), that they hinder the mass transfer between the gas and particle phases e.g., (Rouviere and Ammann 2010) at the liquid−vapor interface or even promote it (Faust, Dempsey et al. 2013, Morris 2013).

1.2.3. Resistance model to describe heterogeneous kinetics

As already mentioned in the previous section, gas-condensed phase interactions are usually described by the uptake coefficient γ, defined as the ratio of the net flux of molecules from the gas phase to the condensed phase to the gas-kinetic collision flux of the molecules to the surface of the condensed phase (Finlayson-Pitts and Pitts, 2000).

$$\gamma = \frac{J_{net}}{J_{coll}} \tag{1.15}$$

The gas kinetic collision flux can be defined as:

$$J_{coll} = \frac{[X]_g \, \omega_x}{4} \tag{1.16}$$

where $[X]_g$ is the concentration of the gas species near the condensed-phase-surface, while ω is the mean molecular velocity of the gaseous species. The uptake of a gas into for example a liquid particle involves several physical and chemical processes.

The first step is diffusion of the gas towards the interface. The gas molecule can then either scatter back to the gas phase or thermally accommodate at the surface. The gaseous diffusion is determined by the gas-phase diffusion coefficient (D_g). The rate of accommodation on the surface is described by the surface accommodation coefficient, defined as the ratio of molecules adsorbed at the surface to the number of gas-surface collisions.

The molecule may then enter and dissolve in the interfacial region. The overall process is described by the bulk accommodation coefficient (α_b), which is the convolution of the surface accommodation and surface to bulk transfer. Surface to bulk transfer of a soluble molecule basically represents its solvation. The diffusion of the dissolved molecule further into the bulk of the solution is determined by the diffusivity in the liquid phase, D_l. If there is no reaction within the liquid phase or the reaction is slow (relative to uptake and diffusion), an equilibrium is finally established between the gas and liquid phase (Henry's law equilibrium), characterized by the Henry's law constant H, where $H = [X]_b / P_x$, with P_x being the gas-phase pressure of X and $[X]_b$ the concentration of X in aqueous solution at equilibrium.

Reaction in the bulk can take place near the surface or over the entire bulk solution depending on the reaction rate compared to the transport rate by diffusion. Reaction at the interface has to be considered in some cases as well. It is involving the molecule X being adsorbed to the surface, which is essentially the formation of a surface complex (e.g., X hydrogen bonding to liquid water or to a solute therein). Such an adsorbed molecule or surface complex may react at the surface before or even without being taken up into the bulk solution. The main type of surface reactions is usually referred to as surface layer reaction (Ammann, Poschl et al. 2003) or a Langmuir-Hinshelwood reaction.

The observed net uptake can be associated with a combination of the processes mentioned above and these chemical and physical processes are often treated in terms of the resistor model for gas-condensed phase interactions (Hanson et al., 1994), which represents a steady state solution to the coupled differential equation system describing the combination all processes. The uptake coefficient represents a normalized loss rate and depends on the elementary processes involved in the condensed phase. The overall resistance to the uptake on a condensed surface would then be (Ammann, Cox et al. 2013):

$$\frac{1}{\gamma} = \frac{1}{\alpha_{\mathrm{s}}} + \frac{1}{\Gamma_{\mathrm{s}} + \left(\frac{1}{\Gamma_{\mathrm{sb}}} + \frac{1}{\Gamma_{\mathrm{b}}}\right)^{-1}}$$

(1.17)

α_{s} represents the surface accommodation coefficient; Γ_{s} the limiting rate for surface reaction, Γ_{sb} the limiting rate for surface to bulk transfer, and Γ_{b} the limiting rate for a reaction in the bulk. Under conditions, where adsorption on the surface and surface to bulk transfer are both not rate limiting (which is likely the case for gas phase O_3 reacting with Br^- in aqueous solution).

Under reasonable assumptions, where reaction in the bulk competes with the diffusive transport of the dissolved trace gas, the limiting rate can be written as,

$$\Gamma_{\mathrm{b}} = \frac{4RTH\sqrt{D_l k_{\mathrm{b}}^{\mathrm{I}}}}{\omega}$$

(1.18)

where R is the gas constant, T is the temperature in Kelvin, H is the Henry's law constant, and D_l is its diffusivity in the liquid phase. $k_{\mathrm{b}}^{\mathrm{I}}$ is the pseudo-first-order reaction rate constant in the

liquid-phase for the gas phase species dissolved in solution. The competition between reaction and diffusion in the liquid phase is best assessed by the so-called reacto-diffusive length, l_{rd}, which is the length within which the bulk concentration of O_3 drops to 1/e of its initial value near the surface:

$$l_{rd} = \sqrt{\frac{D_l}{k_b^I}} \tag{1.19}$$

Therefore, the boundary condition for equation (1.18) representing the limiting rate of uptake is that l_{rd} is much smaller than the thickness of the liquid of interest.

As mentioned above, surface reactions of trace gases on either solid or liquid substrates are often obeying Langmuir-Hinshelwood kinetics. This mechanism has also been suggested for the reaction of O_3 with Br^- (Oldridge and Abbatt 2011). The corresponding limiting uptake coefficient can be described as (Ammann, Cox et al. 2013),

$$\Gamma_s = \frac{4k_s^{II}[Y]_s K_{LangC}(X)N_{max}}{\omega(1 + K_{LangC}(X)[X]_g)} \tag{1.20}$$

Equation (20) demonstrates that Γ_s depends on the gas phase concentration of the trace gas, X, if $K_{LangC}(X)[X]_g$ is similar to or larger than 1 (i.e., at high surface coverage). Here N_{max} is the maximum surface coverage of X on the surface, K_{LangC} is the Langmuir adsorption equilibrium constant of X, $[X]_g$ is the concentration of X in the gas phase, and k_s^I is the pseudo-first-order surface-phase rate constant for the X + Y reaction, given by $k_s^I (s^{-1}) = k_s^{II} \times [Y]_s$, where $[Y]_s$ is the concentration of non-volatile reactant at the surface in units of molecule cm^{-2} and k_s^{II} (cm^2 s^{-1} molecule^{-1}) is the second-order surface-phase rate constant.

1.3. Aqueous solution-air interfaces

The interesting properties of the liquid−vapor interface stem from the fact that this region is inherently an asymmetric environment, which impacts both structure and reactivity. The liquid−vapor interface shows large changes over angstrom-scale distances in properties such as molecular composition, orientation, and density. These qualities can lead to differences in structure and chemistry between the interfacial region and the bulk (Eisenthal 1993, Petersen and Saykally 2006). The spatial distributions of electrolyte ions at the interfaces and their impact on the structure and orientation of the surrounding water molecules is a topic of

significant interest to the atmospheric science community (Hu, Shi et al. 1995, Knipping, Lakin et al. 2000). For example, chemical reactions in the atmosphere frequently occur within atmospheric aerosol, which have high surface to volume ratios. A major fraction of atmospheric aerosols are highly concentrated solutions. In several important cases, reactions between gas and aerosol phase species have a substantial surface component, meaning that a rate limiting reaction channel may exist at the surface as for instance in the case of O_3 reacting with Br^- discussed in this thesis (Ammann, Cox et al. 2013). Differences between the bulk and the liquid−vapor interface in this type of system can have an overall impact on the net chemistry of the atmosphere.

The exclusion from or attraction to the liquid−vapor interface of electrolyte ions is also of fundamental interest (Jungwirth and Tobias 2006), in particular as it relates to developing predictive theories for structure and reactivity. However, before model predictions can be generalized the input parameters and assumptions must be validated by analytical measurements that can provide molecular level insight at the liquid−vapor interface.

With acids and bases, for example, it has become apparent that the interfacial pH can be either more acidic or more basic than the bulk liquid, depending upon the system under examination (Petersen, Iyengar et al. 2004, Buch, Milet et al. 2007, Lewis, Winter et al. 2011). Quantifying these unique properties of the liquid−vapor interface is of practical and great interest.

1.3.1. Surface propensity of (halide) ions at the interface

As mentioned in the previous section, the involvement of surface specific reactions of O_3 with aqueous Br^- containing solutions is an important topic in this thesis. Suggestions for a surface reaction of gas phase O_3 with Br^- ions were partially motivated by the propensity of the larger, more polarizable halide ions i.e. Br^- and I^- for the liquid−vapor interface derived from molecular dynamics (MD) simulation studies (Jungwirth and Tobias 2001, Jungwirth and Tobias 2002). At first sight, this propensity for the interface seemed contrary to the traditional picture that image-charge repulsion should push charged ions away from the surface, which was supported by the experimental observation of an increase of the measured surface tension with increasing salt concentration. This inconsistency had been resolved by Jungwirth and Tobias (Jungwirth and Tobias 2006) by MD simulations demonstrating a relative ion density-profile at the sodium halide salt liquid−vapor interface, see also Fig. 1.3.

These showed a structured layer with the larger, more polarizable halide ions, i.e., I^- and Br^-, enhanced at the outermost surface followed by a layer in which the cation, i.e., Na^+, concentration is enhanced and the I^- or Br^- ion concentration is depleted.
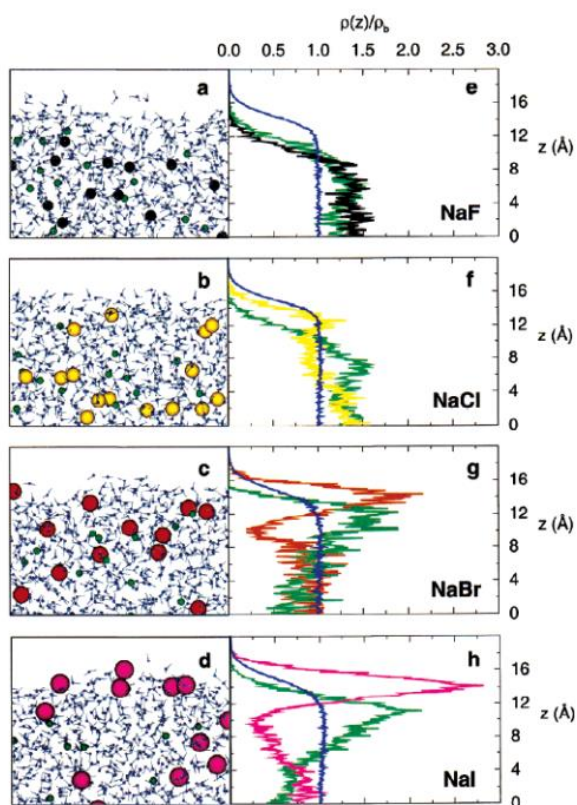
Fig. 1.3. On the left are snapshots from molecular dynamics simulations showing the interfacial distribution of sodium cations and halide anions for sodium halide aqueous solutions. One the right are plots of the corresponding number densities $\rho(z)$ of water oxygen atoms and ions vs distance z from the center of the slabs in the direction normal to the interface, normalized by the bulk water density, ρ_b. The colors of the curves correspond to the coloring of the atoms in the snapshots. The figure is adapted from (Jungwirth and Tobias 2006).

This predicted picture was confirmed by the decrease in anion to cation ratios as experimentally derived from photoelectron spectroscopy experiments when going from shallow probe depth to high probe depth (i.e., averaging over a larger depth) (Ghosal, Hemminger et al. 2005), also see Fig. 1.4, and section 1.4.3 for details on this spectroscopy technique. The surface propensity of the anion relative to the potassium cation (K^+) follows the order $I^- > Br^- > F^-$ and qualitatively agrees with the MD predictions.

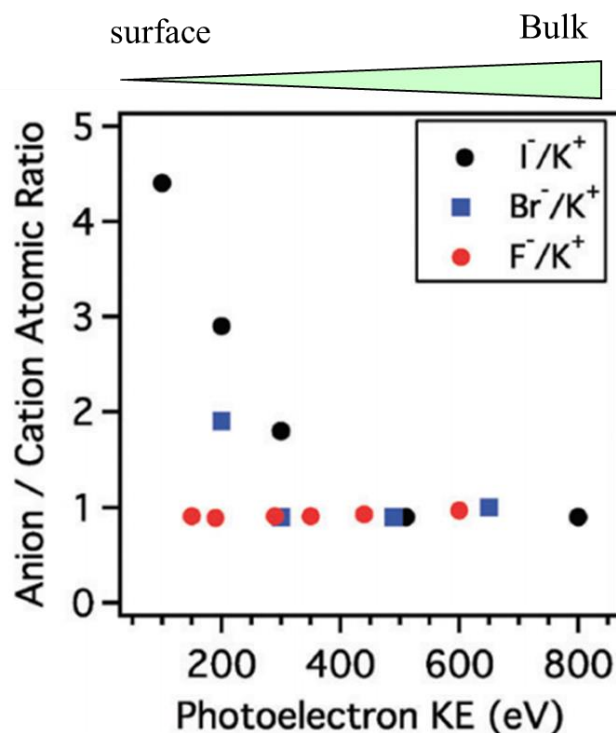**Fig. 1.4.** Ion photoemission signal ratios in solution for KF, KBr and KI as a function of photoelectron kinetic energy. The the F^-/K^+ ion ratio is shown as red circles, the Br^-/K^+ ion ratio is shown as blue squares, and I^-/K^+ ion ratio is shown as black circles. The measurements were done under ambient pressure at the ALS. The figure is adapted from (Brown, Faubel et al. 2009).

1.4. Analytical methods to characterize the liquid−vapor interface

The liquid-vapor interfacial region exhibits properties distinctly different from both the bulk liquid phase and the vapor phase. Selectively examining it is an experimental challenge as many surface-selective experimental techniques require high or ultra-high vacuum for use and cannot be easily applied to liquids with reasonable vapor pressures. Only over the past twenty years progress has been made in the development of surface selective methods that can be used with high vapor pressure liquids such as water. In this regard, five outstanding analytical techniques have recently proved noteworthy complements to the (well established) macroscopic techniques of 1) surface tension (Leroy, Lassin et al. 2010) and 2) surface potential (Frumkin 1924, Jarvis and Scheiman 1968) for the study of air (vacuum)-water interfaces: 3) second harmonic generation (SHG) (Petersen, Johnson et al. 2004, Petersen and Saykally 2004, Petersen and Saykally 2005, Petersen and Saykally 2005, Petersen, Saykally et al. 2005, Petersen and Saykally 2006, Petersen and Saykally 2006, Otten, Petersen et al. 2007, Petersen and Saykally 2008, Bian, Feng et al. 2009, Smolentsev, Chen et al. 2014), 4)

sum-frequency generation (SFG) spectroscopy (Du, Liu et al. 2008, Fan, Chen et al. 2009, Ottosson, Faubel et al. 2010, Hua, Jubb et al. 2011, Tian, Byrnes et al. 2011, Hua, Verreault et al. 2013, Verreault and Allen 2013, Hua, Verreault et al. 2014, Hua, Verreault et al. 2014) and 5) liquid based X-ray photoelectron spectroscopy (XPS) (Winter, Weber et al. 2004, Ghosal, Hemminger et al. 2005, Krisch, D'Auria et al. 2007, Brown, D'Auria et al. 2008, Ghosal, Brown et al. 2008, Baer, Kuo et al. 2009, Brown, Winter et al. 2009, Ottosson, Vacha et al. 2009, Ottosson, Heyda et al. 2010, Lewis, Winter et al. 2011, Lewis, Winter et al. 2011, Cheng, Callahan et al. 2012, Margarella, Perrine et al. 2013, Pruyne, Lee et al. 2014). All of these methods are capable of interrogating the microscopic structure of the air (vacuum)-water interface, and often provide complementary information due to the different properties probed.

1.4.1. Surface tension

Surface tension gives a macroscopic picture of the composition of the interface. In the thermodynamic development of surface tension, it is directly related by the Gibbs equation to the surface excess, Γ_i, of a component i beyond a theoretical dividing plane (referred to as the Gibbs surface) placed parallel to the solution surface (Adamson 1976):

$$\Gamma_i = -\frac{C_i}{RT}\left(\frac{\partial \gamma}{\partial C_i}\right)_T \tag{1.21}$$

where C_i is the mole fraction of component i, R is the universal gas constant and T is the temperature in Kelvin. For simple binary systems, if $\Gamma_i > 0$ and if the Gibbs dividing plane is placed such that the excess of the solvent, i.e., water, is zero, Γ_i is interpreted as surface concentration of molecules. In solutions containing multiple species, different molecular arrangements can give rise to similar measures of surface tension, complicating the direct interpretation of the results. Treatment of the surface tension for these mixtures has been detailed in the literature (Sorjamaa, Svenningsson et al. 2004, Tuckermann 2007, Schwier, Viglione et al. 2013) while a useful review of the interpretation of results is given by Jungwirth and Tobias (Jungwirth and Tobias 2006). Multiple experimental approaches can be used to quantify surface tension but in comparison studies the Wilhelmy plate method has emerged as an accurate and robust approach (Padday and Russell 1960, Soucková, Klomfar et al. 2008). The surface tension is a key parameter in determining atmospheric aerosol

nucleation and growth as well as in cloud droplet nucleation by aerosol particles (Li, Williams et al. 1998, Sorjamaa, Svenningsson et al. 2004).

1.4.2. Sum frequency generation spectroscopy (SFG)

Sum frequency generation spectroscopy (SFG) is a second order non-linear vibrational spectroscopy method typically used to investigate the fundamental OH stretching region (between 3100−3500 cm^{-1}), which provides detailed information on the structure and orientation of water within the non-centrosymmetric region at the interface (Richmond 2002, Gopalakrishnan, Liu et al. 2006, Shen and Ostroverkhov 2006, Fan, Chen et al. 2009). The spectral response in the OH stretch region to the addition of different electrolytes is often used to infer ion distributions at the interface, albeit as there is not a straightforward relationship between the structure of water and the spatial distributions (concentrations) of electrolyte ions in the interface region, this task is nontrivial. Often molecular dynamics (MD) simulations (Jungwirth and Tobias 2006) are leaned on heavily to provide the molecular level detail needed to interpret an SFG spectroscopy experiment.

1.4.3. X-ray photoelectron spectroscopy (XPS)

The photoemission spectroscopy technique is based on the photoelectric effect, first discovered by Heinrich Hertz and Wilhelm Hallwachs in 1887, who pointed out that when a solid is exposed to electromagnetic radiation the radiation is absorbed only above a certain threshold frequency, which is specific for the material, and electrons are emitted from the solid. The early attempts to explain this effect within Maxwell's wave theory of light, according to which the energy of the emitted electrons should increase with the intensity of the radiation, finally failed in 1902 when Philippe Lenard observed that the energy of the emitted electrons is proportional to the frequency of the light. In 1905, Albert Einstein solved this problem by postulating the quantum hypothesis for the electromagnetic radiation, for which he was awarded the Nobel Prize in Physics in 1921. According to Einstein's model, light is composed of discrete quanta, that is, photons, rather than continuous waves. A photon transfers its energy completely to the electron in the solid and, if the energy of the electron exceeds a certain threshold energy (work function), it may leave the surface. Later on, between 1950 and 1960, Kai M. Siegbahn developed the Electron Spectroscopy for Chemical Analysis (ESCA) technique in which the photoemission peaks, i.e., the number of the photoelectrons measured as a function of their kinetic energies are used to determine the

composition and chemical state of the sample surface. The development of ESCA, nowadays commonly known as X-ray Photoelectron Spectroscopy (XPS), led to the award of the Physics Nobel Prize in 1981 to Kai M. Siegbahn. Since then, the experimental study of photoelectron spectroscopy has made remarkable progress – especially with the development of high flux, tunable X-ray sources such as synchrotron facilities.

A deeper theoretical understanding and the development of sophisticated computational methods allowed calculating binding energies of very complex systems. Consequently, the combination of high experimental accuracy and theoretical efforts can now yield relevant information about the chemistry of molecules and solids, and makes XPS one of the most powerful and widely used surface characterization tools. As already discussed, photoemission occurs whenever photons with high enough energy hit the surface and kick out the photoelectrons. Within a one-electron approximation, the kinetic energy (KE) of the photoelectron can be derived from the energy conservation law as

$$KE = h\nu - BE - \phi \qquad\qquad\qquad (1.22)$$

where h is the Planck constant, ν is the frequency of the radiation, BE is the binding energy and ϕ is the specific work function of the material. It is possible to estimate experimental BEs from the XPS spectrum if the other quantities in (1.22) are known. Since the value of the BE is characteristic for each element, XPS can be used for the analysis of the elements in a sample. This chemical specificity is one of the most striking features of the XPS technique. One of the most important properties of photoelectron spectroscopy, namely, the surface sensitivity, is related to the inelastic mean free path (IMFP) of electrons in solids. The IMFP is shown in Fig. 1.5 as a function of the kinetic energy of the electrons in the range of practical interest for a typical XPS experiment. The behavior of the experimental points is described by the dashed 'universal curve' (Seah and Dench 1979). For energies between 10 and 500 eV, for typical relatively dense solid materials, the IMFP is less than 1 nm that means that only the photoelectrons excited within a depth of 1 nm from the surface can be detected causing the high surface sensitivity of the XPS technique. The universal behavior of the IMFP in the interval between 10-500 eV is due to the main scattering mechanism in this energy window, that is, the excitation of conduction electrons (plasmons) whose density is similar in all metals. At lower energies, electron-hole pair formation and electron-phonon scattering become more important, and the distance between inelastic collisions increases. At higher energies, instead, the rise of the IMFP is due to a decrease of the cross-section for

plasmon excitations. The IMFP for soft materials e.g. liquid water and aqueous solutions has only been studied recently and it was found that the minimum of the universal curve for water is shifted towards the higher photoelectron kinetic energy (eKE) side relative to dense solid materials (Ottosson, Faubel et al. 2010). In absence of calibration methods, establishing the IMFP in liquids has remained an open challenge.
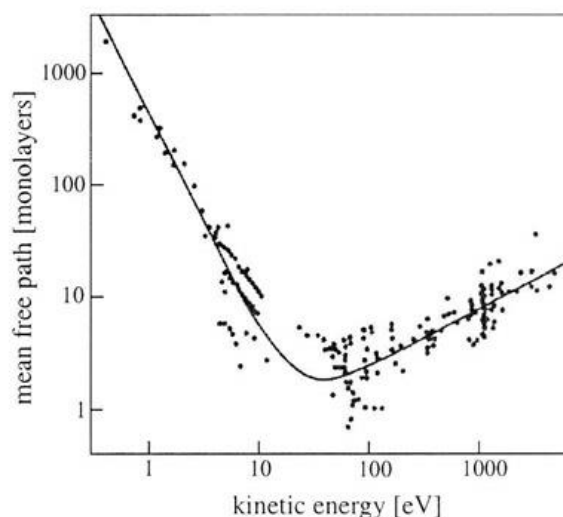

Fig. 1.5. The 'universal' curve of the electron IMFP as a function of the electron kinetic energy. The solid curve shows the theoretical prediction and the data points are taken from a wide variety of materials. Figure is adapted from (Seah and Dench 1979).

1.4.4. X-ray Photoelectron Spectroscopy from liquids

Electron spectroscopy from liquids has a long history that dates to the pioneering work of Siegbahn, *ESCA Applied to Liquids*, published in 1973 (Siegbahn and Siegbahn 1973). In the forty years since Siegbahn's first spectrum of liquid formamide, electron spectroscopy for chemical analysis (ESCA) from liquids has been revolutionized (Winter and Faubel 2006, Jungwirth and Winter 2008, Brown, Faubel et al. 2009, Winter, 2009; Seidel, Thürmer et al. 2011, Brown, Jordan et al. 2013). Three major advances have made this possible. Most important was the advent of third generation synchrotron radiation facilities such as the Swiss Light Source (http://www.psi.ch/sls) (SLS) that produce brilliant tunable X-ray beams that create a flux of photoelectrons from the liquid sample that dwarfs that produced by the conventional anode X-ray source used in the laboratory of Siegbahn. Modern day electron spectrometers have also helped (Grass, Karlsson et al. 2010). They offer increased transmission and detection efficiency and greatly improved resolution that not only increase

the signal-to-noise ratio of a spectrum but now can resolve also near-overlapping electronic structures that in the past went undetected. Finally, the development of a vacuum liquid microjet (Faubel, Steiner et al. 1997, Siegbahn, Asplund et al. 1975, Siegbahn, Svensson et al. 1981) has allowed for studies of high vapor pressure liquids, such as pure water (Winter, Weber et al. 2004, Winter, Faubel et al. 2006), dilute electrolyte solutions (Brown, Winter et al. 2009), and organic solutes (Brown, Vila et al. 2012) under analysis chamber pressures of ca. 10^{-4} mbar. Performing electron spectroscopy of liquids under 10^{-4} mbar eliminates a large fraction of the inelastic scattering the photoelectron experiences during ambient pressure liquid studies (Starr, Wong et al. 2008, Brown, D'Auria et al. 2008) while also reducing the gas phase contribution to the spectrum. Both have helped to reduce ambiguity in spectral assignments.

Using a liquid microjet as the sample delivery platform presents several advantages over studying the liquid−vapor interface of static samples (Winter and Faubel 2006, Jungwirth and Winter 2008, Brown, Faubel et al. 2009, Winter, 2009; Seidel, Thürmer et al. 2011, Brown, Jordan et al. 2013). The liquid microjet provides a continuously refreshed interface that remains free of the adventitious carbon impurities that plague static measurements at the liquid−vapor interface (Krisch, D'Auria et al. 2007). The continuously refreshed interface limits beam damage to the sample (Krisch, D'Auria et al. 2007, Ghosal, Brown et al. 2008). In addition, the liquid microjet makes virtually any liquid sample compatible with electron spectroscopy, which provides an endless array of opportunities for cross-collaboration between research fields and disciplines (Brown, Jordan et al. 2013).

The analytical technique employed in the current study is XPS. However, unlike SFG spectroscopy, XPS is a quantitative tool that can directly interrogate every electrolyte ion and has variable depth resolution (vide infra) but it is largely insensitive to structural changes of water upon addition of electrolytes (geometrical rearrangements of water molecules do not materialize in the core-level O 1s binding energy, and the increase/decrease in the thickness of the non-centrosymmetric interfacial layer probed in SFG spectroscopy with electrolyte addition is a constant in XPS that depends only on the kinetic energy of the outgoing photoelectron). XPS is a valuable complement to SFG spectroscopy (or vice versa) for the study of aqueous electrolyte interfaces.

1.5. The effect of organics on the distribution of ions at the interface

The exact physical origins (such as solute and solvent surface polarization, hydrophobic effects, and so forth) of the high degree of ion specificity are, however, still not well understood. While studies of pure salt solution surfaces are of great importance to our understanding of ion adsorption at real-world water surfaces, however, it is important to realize that they represent oversimplified model systems: Naturally occurring salt water surfaces, such as marine aerosol or ocean surface water, typically consist of both water-soluble and insoluble organic species (Middlebrook, Murphy et al. , Putaud, Van Dingenen et al. 2000). Natural organics presented in the environment, such as long-chain carboxylic acids and alcohols tend to adsorb at the liquid−vapor interface, i.e. behave like surfactants. Oxygenated volatile organic compounds (OVOC) are considered important in atmospheric chemistry to affect the surface tension and gas–particle exchange rates (Donaldson and George 2012). e.g. in the study of Rouviere et al. (Rouviere and Ammann) which has looked at the effect of fatty acids on the O_3 with I^- reaction. They found that the presence of fatty acids in aqueous aerosol particles can potentially decrease the uptake of O_3.

Some OVOC species are acids (carboxylic acids), which are major acidifying species in aerosol particles and cloud droplets. Several studies show an enhanced presence of protonated acids at interface, e.g., (Ottosson, Wernersson et al. 2011, Prisle, Ottosson et al.). The specific acidic environment potentially induced by acids at the liquid−vapor interface may be related to novel acid-catalyzed chemistry recently discovered (Enami, Hoffmann et al. 2008). Since the reaction studied in this thesis, $O_3 + Br^-$, is acid catalyzed (see section 5.4.1), enhanced acidity at the interface could play an important role.

In the context of the thesis, an important aspect of the surface propensity of organics is that they may have a significant effect on the way halide ions are distributed at the interface (Krisch, D'Auria et al. 2007, Tobias and Hemminger 2008, Tang and Allen 2009, Onorato, Otten et al. 2010, Huang, Hua et al. 2013, Huang, Hua et al. 2013). In more detail, the aim is to have a better understanding of the contrasting effect of an alcohol, a carboxylic acid, and even a more complex organic (which has both functional groups) on the ion distribution at the liquid−vapor interface. The primary approaches to study the interplay between the ions and the organics at the interface will be by employing near-ambient pressure X-ray photoelectron spectroscopy, and laboratory based O_3 uptake kinetics experiments. By this aa

more realistic picture of halogen release processes in the marine boundary layer should emerge.

References

Adamson, A. W. (1976). Physical Chemistry of Surfaces. New York, Wiley.

Alvarez, R. J., II, C. J. Senff, A. O. Langford, A. M. Weickmann, D. C. Law, J. L. Machol, D. A. Merritt, R. D. Marchbanks, S. P. Sandberg, W. A. Brewer, R. M. Hardesty and R. M. Banta (2011). "Development and Application of a Compact, Tunable, Solid-State Airborne Ozone Lidar System for Boundary Layer Profiling." Journal of Atmospheric and Oceanic Technology **28**(10): 1258-1272.

Ammann, M., R. A. Cox, J. N. Crowley, M. E. Jenkin, A. Mellouki, M. J. Rossi, J. Troe and T. J. Wallington (2013). "Evaluated kinetic and photochemical data for atmospheric chemistry: Volume VI - heterogeneous reactions with liquid substrates." Atmospheric Chemistry and Physics **13**(16): 8045-8228.

Ammann, M., U. Poschl and Y. Rudich (2003). "Effects of reversible adsorption and Langmuir-Hinshelwood surface reactions on gas uptake by atmospheric particles." Physical Chemistry Chemical Physics **5**(2): 351-356.

Atkinson, R., D. L. Baulch, R. A. Cox, J. N. Crowley, R. F. Hampson, R. G. Hynes, M. E. Jenkin, M. J. Rossi and J. Troe (2006). "Evaluated kinetic and photochemical data for atmospheric chemistry: Volume II - gas phase reactions of organic species." Atmospheric Chemistry and Physics **6**: 3625-4055.

Baer, M. D., I. F. W. Kuo, H. Bluhm and S. Ghosal (2009). "Interfacial Behavior of Perchlorate versus Chloride Ions in Aqueous Solutions." Journal of Physical Chemistry B **113**(48): 15843-15850.

Bell, M. L., A. McDermott, S. L. Zeger, J. M. Samet and F. Dominici (2004). "Ozone and short-term mortality in 95 US urban communities, 1987-2000." Jama-Journal of the American Medical Association **292**(19): 2372-2378.

Bian, H. T., R. R. Feng, Y. Guo and H. F. Wang (2009). "Specific Na+ and K+ Cation Effects on the Interfacial Water Molecules at the Air/Aqueous Salt Solution Interfaces Probed with Nonresonant Second Harmonic Generation." Journal of Chemical Physics **130**(13).

Brown, M. A., R. D'Auria, I. F. W. Kuo, M. J. Krisch, D. E. Starr, H. Bluhm, D. J. Tobias and J. C. Hemminger (2008). "Ion spatial distributions at the liquid-vapor interface of aqueous potassium fluoride solutions." Physical Chemistry Chemical Physics **10**(32): 4778-4784.

Brown, M. A., M. Faubel and B. Winter (2009). "X-Ray photo- and resonant Auger-electron spectroscopy studies of liquid water and aqueous solutions." Annual Reports Section "C" (Physical Chemistry) **105**(0): 174-212.

Brown, M. A., B. Winter, M. Faubel and J. C. Hemminger (2009). "Spatial Distribution of Nitrate and Nitrite Anions at the Liquid/Vapor Interface of Aqueous Solutions." Journal of the American Chemical Society **131**(24): 8354-8355.

Buch, V., A. Milet, R. Vacha, P. Jungwirth and J. P. Devlin (2007). "Water Surface is Acidic." Proceedings of the National Academy of Sciences of the United States of America **104**(18): 7342-7347.

Carpenter, L. J., S. M. MacDonald, M. D. Shaw, R. Kumar, R. W. Saunders, R. Parthipan, J. Wilson and J. M. C. Plane (2013). "Atmospheric iodine levels influenced by sea surface emissions of inorganic iodine." Nature Geoscience **6**(2): 108-111.

Cheng, M. H., K. M. Callahan, A. M. Margarella, D. J. Tobias, J. C. Hemminger, H. Bluhm and M. J. Krisch (2012). "Ambient Pressure X-ray Photoelectron Spectroscopy and Molecular Dynamics Simulation Studies of Liquid/Vapor Interfaces of Aqueous NaCl, RbCl, and RbBr Solutions." Journal of Physical Chemistry C **116**(7): 4545-4555.

Clifford, D. and D. J. Donaldson (2007). "Direct experimental evidence for a heterogeneous reaction of ozone with bromide at the air-aqueous interface." Journal of Physical Chemistry A **111**(39): 9809-9814.

Donaldson, D. J. and C. George (2012). "Sea-Surface Chemistry and Its Impact on the Marine Boundary Layer." Environmental Science & Technology **46**(19): 10385-10389.

Donaldson, D. J. and V. Vaida (2006). "The influence of organic films at the air-aqueous boundary on atmospheric processes." Chemical Reviews **106**(4): 1445-1461.

Du, H., J. Liu, O. Ozdemir, A. V. Nguyen and J. D. Miller (2008). "Molecular Features of the Air/Carbonate Solution Interface." Journal of Colloid and Interface Science **318**(2): 271-277.

Eisenthal, K. B. (1993). "Liquid Interfaces." Accounts of Chemical Research **26**(12): 636-643.

Enami, S., M. R. Hoffmann and A. J. Colussi (2008). "Acidity Enhances the Formation of a Persistent Ozonide at Aqueous Ascorbate/Ozone Gas Interfaces." Proceedings of the National Academy of Sciences of the United States of America **105**(21): 7365-7369.

Fan, S. M. and D. J. Jacob (1992). "SURFACE OZONE DEPLETION IN ARCTIC SPRING SUSTAINED BY BROMINE REACTIONS ON AEROSOLS." Nature **359**(6395): 522-524.

Fan, Y. B., X. Chen, L. J. Yang, P. S. Cremer and Y. Q. Gao (2009). "On the Structure of Water at the Aqueous/Air Interface." Journal of Physical Chemistry B **113**(34): 11672-11679.

Faust, J. A., L. P. Dempsey and G. M. Nathanson (2013). "Surfactant-Promoted Reactions of Cl_2 and Br_2 with Br^- in Glycerol." Journal of Physical Chemistry B **117**(41): 12602-12612.

Finlayson-Pitts, B. J. and J. N. Pitts (1993). "ATMOSPHERIC CHEMISTRY OF TROPOSPHERIC OZONE FORMATION - SCIENTIFIC AND REGULATORY IMPLICATIONS." Journal of the Air & Waste Management Association **43**(8): 1091-1100.

Foster, K. L., R. A. Plastridge, J. W. Bottenheim, P. B. Shepson, B. J. Finlayson-Pitts and C. W. Spicer (2001). "The role of Br_2 and BrCl in surface ozone destruction at polar sunrise." Science **291**(5503): 471-474.

Frumkin, A. (1924). "Phase Interface Powers and Adsorption on the Segregative Surface Air - Solution of Anorganic Electrolyte. [Original Title in German: "Phasengrenzkräfte und Adsorption an der Trennungsfläche Luft: Lösung anorganischer Elektrolyte"]." Zeitschrift Fur Physikalische Chemie--Stochiometrie Und Verwandtschaftslehre **109**(1/2): 34-48.

Ghosal, S., M. A. Brown, H. Bluhm, M. J. Krisch, M. Salmeron, P. Jungwirth and J. C. Hemminger (2008). "Ion Partitioning at the Liquid/Vapor Interface of a Multicomponent Alkali Halide Solution: A Model for Aqueous Sea Salt Aerosols." Journal of Physical Chemistry A **112**(48): 12378-12384.

Ghosal, S., J. C. Hemminger, H. Bluhm, B. S. Mun, E. L. D. Hebenstreit, G. Ketteler, D. F. Ogletree, F. G. Requejo and M. Salmeron (2005). "Electron spectroscopy of aqueous solution interfaces reveals surface enhancement of halides." Science **307**(5709): 563-566.

Gopalakrishnan, S., D. F. Liu, H. C. Allen, M. Kuo and M. J. Shultz (2006). "Vibrational spectroscopic studies of aqueous interfaces: Salts, acids, bases, and nanodrops." Chemical Reviews **106**(4): 1155-1175.

Haag, W. R. and J. Hoigne (1983). "Ozonation of Bromide-Containing Waters - Kinetics of Formation of Hypobromous Acid and Bromate." Environmental Science & Technology **17**(5): 261-267.

Hu, J. H., Q. Shi, P. Davidovits, D. R. Worsnop, M. S. Zahniser and C. E. Kolb (1995). "REACTIVE UPTAKE OF CL2(G) AND BR2(G) BY AQUEOUS SURFACES AS A FUNCTION OF BR⁻ AND I- ION CONCENTRATION - THE EFFECT OF CHEMICAL-REACTION AT THE INTERFACE." Journal of Physical Chemistry **99**(21): 8768-8776.

Hua, W., A. M. Jubb and H. C. Allen (2011). "Electric Field Reversal of Na2SO4, (NH4)(2)SO4, and Na2CO3 Relative to CaCl2 and NaCl at the Air/Aqueous Interface Revealed by Heterodyne Detected Phase-Sensitive Sum Frequency." Journal of Physical Chemistry Letters **2**(20): 2515-2520.

Hua, W., D. Verreault and H. C. Allen (2013). "Surface Prevalence of Perchlorate Anions at the Air/Aqueous Interface." Journal of Physical Chemistry Letters **4**(24): 4231-4236.

Hua, W., D. Verreault and H. C. Allen (2014). "Surface Electric Fields of Aqueous Solutions of NH4NO3, Mg(NO3)2, NaNO3, and LiNO3: Implications for Atmospheric Aerosol Chemistry." Journal of Physical Chemistry C **118**: 24941-24949.

Hua, W., D. Verreault, Z. S. Huang, E. M. Adams and H. C. Allen (2014). "Cation Effects on Interfacial Water Organization of Aqueous Chloride Solutions. I. Monovalent Cations: Li+, Na+, K+, and NH4+." Journal of Physical Chemistry B **118**(28): 8433-8440.

Huang, Z., W. Hua, D. Verreault and H. C. Allen (2013). "Influence of Salt Purity on Na+ and Palmitic Acid Interactions." Journal of Physical Chemistry A **117**(50): 13412-13418.

Huang, Z., W. Hua, D. Verreault and H. C. Allen (2013). "Salty Glycerol versus Salty Water Surface Organization: Bromide and Iodide Surface Propensities." Journal of Physical Chemistry A **117**(29): 6346-6353.

Hunt, S. W., M. Roeselova, W. Wang, L. M. Wingen, E. M. Knipping, D. J. Tobias, D. Dabdub and B. J. Finlayson-Pitts (2004). "Formation of molecular bromine from the reaction of ozone with deliquesced NaBr aerosol: Evidence for interface chemistry." Journal of Physical Chemistry A **108**(52): 11559-11572.

Jarvis, N. L. and M. A. Scheiman (1968). "Surface Potentials of Aqueous Electrolyte Solutions." Journal of Physical Chemistry **72**(1): 74-&.

Jungwirth, P. and D. J. Tobias (2001). "Molecular structure of salt solutions: A new view of the interface with implications for heterogeneous atmospheric chemistry." Journal of Physical Chemistry B **105**(43): 10468-10472.

Jungwirth, P. and D. J. Tobias (2002). "Ions at the air/water interface." Journal of Physical Chemistry B **106**(25): 6361-6373.

Jungwirth, P. and D. J. Tobias (2006). "Specific Ion Effects at the Air/Water Interface." Chem. Rev. **106**(4): 1259-1281.

Kanakidou, M., J. H. Seinfeld, S. N. Pandis, I. Barnes, F. J. Dentener, M. C. Facchini, R. Van Dingenen, B. Ervens, A. Nenes, C. J. Nielsen, E. Swietlicki, J. P. Putaud, Y. Balkanski, S. Fuzzi, J. Horth, G. K. Moortgat, R. Winterhalter, C. E. L. Myhre, K. Tsigaridis, E. Vignati, E. G. Stephanou and J. Wilson (2005). "Organic aerosol and global climate modelling: a review." Atmospheric Chemistry and Physics **5**: 1053-1123.

Keene, W. C., H. Maring, J. R. Maben, D. J. Kieber, A. A. P. Pszenny, E. E. Dahl, M. A. Izaguirre, A. J. Davis, M. S. Long, X. Zhou, L. Smoydzin and R. Sander (2007). "Chemical and physical characteristics of nascent aerosols produced by bursting bubbles at a model air-sea interface." Journal of Geophysical Research-Atmospheres **112**(D21).

Knipping, E. M., M. J. Lakin, K. L. Foster, P. Jungwirth, D. J. Tobias, R. B. Gerber, D. Dabdub and B. J. Finlayson-Pitts (2000). "Experiments and simulations of ion-enhanced interfacial chemistry on aqueous NaCl aerosols." Science **288**(5464): 301-306.

Krisch, M. J., R. D'Auria, M. A. Brown, D. J. Tobias, J. C. Hemminger, M. Ammann, D. E. Starr and H. Bluhm (2007). "The effect of an organic surfactant on the liquid-vapor interface of an electrolyte solution." Journal of Physical Chemistry C **111**(36): 13497-13509.

Leroy, P., A. Lassin, M. Azaroual and L. Andre (2010). "Predicting the Surface Tension of Aqueous 1:1 Electrolyte Solutions at High Salinity." Geochimica Et Cosmochimica Acta **74**(19): 5427-5442.

Lewis, T., B. Winter, A. C. Stern, M. D. Baer, C. J. Mundy, D. J. Tobias and J. C. Hemminger (2011). "Dissociation of Strong Acid Revisited: X-ray Photoelectron Spectroscopy and Molecular Dynamics Simulations of HNO3 in Water." Journal of Physical Chemistry B **115**(30): 9445-9451.

Lewis, T., B. Winter, A. C. Stern, M. D. Baer, C. J. Mundy, D. J. Tobias and J. C. Hemminger (2011). "Does Nitric Acid Dissociate at the Aqueous Solution Surface?" Journal of Physical Chemistry C **115**(43): 21183-21190.

Li, Z. D., A. L. Williams and M. J. Rood (1998). "Influence of Soluble Surfactant Properties on the Activation of Aerosol Particles Containing Inorganic Solute." Journal of the Atmospheric Sciences **55**(10): 1859-1866.

Liu, Q., L. M. Schurter, C. E. Muller, S. Aloisio, J. S. Francisco and D. W. Margerum (2001). "Kinetics and mechanisms of aqueous ozone reactions with bromide, sulfite, hydrogen sulfite, iodide, and nitrite ions." Inorganic Chemistry **40**(17): 4436-4442.

Margarella, A. M., K. A. Perrine, T. Lewis, M. Faubel, B. Winter and J. C. Hemminger (2013). "Dissociation of Sulfuric Acid in Aqueous Solution: Determination of the Photoelectron Spectral Fingerprints of H2SO4, HSO4-, and SO42- in Water." Journal of Physical Chemistry C **117**(16): 8131-8137.

McConnell, J. C., G. S. Henderson, L. Barrie, J. Bottenheim, H. Niki, C. H. Langford and E. M. J. Templeton (1992). "PHOTOCHEMICAL BROMINE PRODUCTION IMPLICATED IN ARCTIC BOUNDARY-LAYER OZONE DEPLETION." Nature **355**(6356): 150-152.

Michalowski, B. A., J. S. Francisco, S. M. Li, L. A. Barrie, J. W. Bottenheim and P. B. Shepson (2000). "A computer model study of multiphase chemistry in the Arctic boundary layer during polar sunrise." Journal of Geophysical Research-Atmospheres **105**(D12): 15131-15145.

Middlebrook, A. M., D. M. Murphy and D. S. Thomson (1998). "Observations of organic material in individual marine particles at Cape Grim during the First Aerosol Characterization Experiment (ACE 1)." Journal of Geophysical Research-Atmospheres **103**(D13): 16475-16483.

Morris, J. R. (2013). "Developing a Molecular-Level Understanding of Organic Chemistry and Physics at the Gas-Surface Interface." Journal of Physical Chemistry Letters **4**(23): 4055-4057.

Mozurkewich, M. (1995). "MECHANISMS FOR THE RELEASE OF HALOGENS FROM SEA-SALT PARTICLES BY FREE-RADICAL REACTIONS." Journal of Geophysical Research-Atmospheres **100**(D7): 14199-14207.

O'Dowd, C. D., M. C. Facchini, F. Cavalli, D. Ceburnis, M. Mircea, S. Decesari, S. Fuzzi, Y. J. Yoon and J. P. Putaud (2004). "Biogenically driven organic contribution to marine aerosol." Nature **431**(7009): 676-680.

Oldridge, N. W. and J. P. D. Abbatt (2011). "Formation of Gas-Phase Bromine from Interaction of Ozone with Frozen and Liquid NaCl/NaBr Solutions: Quantitative Separation of Surficial Chemistry from Bulk-Phase Reaction." Journal of Physical Chemistry A **115**(12): 2590-2598.

Onorato, R. M., D. E. Otten and R. J. Saykally (2010). "Measurement of Bromide Ion Affinities for the Air/Water and Dodecanol/Water Interfaces at Molar Concentrations by UV Second Harmonic Generation Spectroscopy." Journal of Physical Chemistry C **114**(32): 13746-13751.

Otten, D. E., P. B. Petersen and R. J. Saykally (2007). "Observation of Nitrate Ions at the Air/Water Interface by UV-Second Harmonic Generation." Chemical Physics Letters **449**(4-6): 261-265.

Ottosson, N., M. Faubel, S. E. Bradforth, P. Jungwirth and B. Winter (2010). "Photoelectron spectroscopy of liquid water and aqueous solution: Electron effective attenuation lengths and emission-angle anisotropy." Journal of Electron Spectroscopy and Related Phenomena **177**(2-3): 60-70.

Ottosson, N., J. Heyda, E. Wernersson, W. Pokapanich, S. Svensson, B. Winter, G. Ohrwall, P. Jungwirth and O. Bjorneholm (2010). "The Influence of Concentration on the Molecular Surface Structure of Simple and Mixed Aqueous Electrolytes." Physical Chemistry Chemical Physics **12**(36): 10693-10700.

Ottosson, N., R. Vacha, E. F. Aziz, W. Pokapanich, W. Eberhardt, S. Svensson, G. Ohrwall, P. Jungwirth, O. Bjorneholm and B. Winter (2009). "Large Variations in the Propensity of Aqueous Oxychlorine Anions for the Solution/Vapor Interface." Journal of Chemical Physics **131**(12).

Ottosson, N., E. Wernersson, J. Soderstrom, W. Pokapanich, S. Kaufmann, S. Svensson, I. Persson, G. Ohrwall and O. Bjorneholm (2011). "The protonation state of small carboxylic acids at the water surface from photoelectron spectroscopy." Physical Chemistry Chemical Physics **13**(26): 12261-12267.

Padday, J. F. and D. R. Russell (1960). "The Measurement of the Surface Tension of Pure Liquids and Solutions." Journal of Colloid Science **15**: 503-511.

Petersen, M. K., S. S. Iyengar, T. J. F. Day and G. A. Voth (2004). "The Hydrated Proton at the Water Liquid/Vapor Interface." Journal of Physical Chemistry B **108**(39): 14804-14806.

Petersen, P. B., J. C. Johnson, K. P. Knutsen and R. J. Saykally (2004). "Direct Experimental Validation of the Jones-Ray Effect." Chemical Physics Letters **397**(1-3): 46-50.

Petersen, P. B. and R. J. Saykally (2004). "Confirmation of Enhanced Anion Concentration at the Liquid Water Surface." Chemical Physics Letters **397**(1-3): 51-55.

Petersen, P. B. and R. J. Saykally (2005). "Adsorption of Ions to the Surface of Dilute Electroyte Solutions: The Jones-Ray Effect Revisited." Journal of the American Chemical Society **127**(44): 15446-15452.

Petersen, P. B. and R. J. Saykally (2005). "Evidence for an Enhanced Hydronium Concentration at the Liquid Water Surface." Journal of Physical Chemistry B **109**(16): 7976-7980.

Petersen, P. B. and R. J. Saykally (2006). "On the Nature of Ions at the Liquid Water Surface." Annual Review of Physical Chemistry **57**: 333-364.

Petersen, P. B. and R. J. Saykally (2006). "Probing the Interfacial Structure of Aqueous Electrolytes with Femtosecond Second Harmonic Generation Spectroscopy." Journal of Physical Chemistry B **110**(29): 14060-14073.

Petersen, P. B. and R. J. Saykally (2008). "Is the Liquid Water Surface Basic or Acidic? Macroscopic vs. Molecular-Scale Investigations." Chemical Physics Letters **458**(4-6): 255-261.

Petersen, P. B., R. J. Saykally, M. Mucha and P. Jungwirth (2005). "Enhanced Concentration of Polarizable Anions at the Liquid Water Surface: SHG Spectroscopy and MD Simulations of Sodium Thiocyanide." Journal of Physical Chemistry B **109**(21): 10915-10921.

Platt, U. and C. Janssen (1995). "Observation and role of the free radicals NO3, ClO, BrO and IO in the troposphere." Faraday Discussions **100**: 175-198.

Prisle, N. L., N. Ottosson, G. Ohrwall, J. Soderstrom, M. Dal Maso and O. Bjorneholm (2012). "Surface/bulk partitioning and acid/base speciation of aqueous decanoate: direct observations and atmospheric implications." Atmospheric Chemistry and Physics **12**(24): 12227-12242.

Pruyne, J. G., M.-T. Lee, C. Fábri, A. Beloqui Redondo, A. Kleibert, M. Ammann, M. A. Brown and M. J. Krisch (2014). "Liquid-Vapor Interface of Formic Acid Solutions in Salt Water: A Comparison of Macroscopic Surface Tension and Microscopic In Situ X-ray Photoelectron Spectroscopy." Journal of Physical Chemistry C **118**: 29350-29360.

Putaud, J. P., R. Van Dingenen, M. Mangoni, A. Virkkula, F. Raes, H. Maring, J. M. Prospero, E. Swietlicki, O. H. Berg, R. Hillamo and T. Makela (2000). "Chemical mass closure and assessment of the origin of the submicron aerosol in the marine boundary layer and the free troposphere at Tenerife during ACE-2." Tellus Series B-Chemical and Physical Meteorology **52**(2): 141-168.

Read, K. A., A. S. Mahajan, L. J. Carpenter, M. J. Evans, B. V. E. Faria, D. E. Heard, J. R. Hopkins, J. D. Lee, S. J. Moller, A. C. Lewis, L. Mendes, J. B. McQuaid, H. Oetjen, A. Saiz-Lopez, M. J. Pilling and J. M. C. Plane (2008). "Extensive halogen-mediated ozone destruction over the tropical Atlantic Ocean." Nature **453**(7199): 1232-1235.

Richmond, G. L. (2002). "Molecular bonding and interactions at aqueous surfaces as probed by vibrational sum frequency spectroscopy." Chemical Reviews **102**(8): 2693-2724.

Rouviere, A. and M. Ammann (2010). "The effect of fatty acid surfactants on the uptake of ozone to aqueous halogenide particles." Atmospheric Chemistry and Physics **10**(23): 11489-11500.

Saiz-Lopez, A., J. F. Lamarque, D. E. Kinnison, S. Tilmes, C. Ordonez, J. J. Orlando, A. J. Conley, J. M. C. Plane, A. S. Mahajan, G. S. Santos, E. L. Atlas, D. R. Blake, S. P. Sander, S. Schauffler, A. M. Thompson and G. Brasseur (2012). "Estimating the climate significance of halogen-driven ozone loss in the tropical marine troposphere." Atmospheric Chemistry and Physics **12**(9): 3939-3949.

Saiz-Lopez, A. and J. M. C. Plane (2004). "Recent applications of differential optical absorption spectroscopy: Halogen chemistry in the lower troposphere." Journal De Physique Iv **121**: 223-238.

Sander, R. and P. J. Crutzen (1996). "Model study indicating halogen activation and ozone destruction in polluted air masses transported to the sea." Journal of Geophysical Research-Atmospheres **101**(D4): 9121-9138.

Schwier, A. N., G. A. Viglione, Z. Li and V. F. McNeill (2013). "Modeling the Surface Tension of Complex, Reactive Organic-Inorganic Mixtures." Atmospheric Chemistry and Physics **13**(21): 10721-10732.

Seah, M. P. and W. A. Dench (1979). "Quantitative electron spectroscopy of surfaces: a standard data base for electron inelastic mean free paths in solids." Surface and Interface Analysis **1**(1): 2-11.

Seinfeld, J. H. and Pandis, S. N.: Athmospheric Chemistry and Physics: from Air Polution to Climate Change, John Wiley & Sons, Inc., New York, USA, 1998.

Shen, Y. R. and V. Ostroverkhov (2006). "Sum-frequency vibrational spectroscopy on water interfaces: Polar orientation of water molecules at interfaces." Chemical Reviews **106**(4): 1140-1154.

Siegbahn, H. and K. Siegbahn (1973). "ESCA applied to liquids." Journal of Electron Spectroscopy and Related Phenomena **2**(4): 319-325.

Simpson, W. R., R. von Glasow, K. Riedel, P. Anderson, P. Ariya, J. Bottenheim, J. Burrows, L. J. Carpenter, U. Friess, M. E. Goodsite, D. Heard, M. Hutterli, H. W. Jacobi, L. Kaleschke, B. Neff, J. Plane, U. Platt, A. Richter, H. Roscoe, R. Sander, P. Shepson, J. Sodeau, A. Steffen, T. Wagner and E. Wolff (2007). "Halogens and their role in polar boundary-layer ozone depletion." Atmospheric Chemistry and Physics **7**(16): 4375-4418.

Smolentsev, N., Y. Chen, K. C. Jena, M. A. Brown and S. Roke (2014). "Sum Frequency and Second Harmonic Generation from the Surface of a Liquid Microjet." Journal of Chemical Physics **141**: 18C524.

Sorjamaa, R., B. Svenningsson, T. Raatikainen, S. Henning, M. Bilde and A. Laaksonen (2004). "The Role of Surfactants in Köhler Theory Reconsidered." Atmospheric Chemistry and Physics **4**: 2107-2117.

Souckova, M., J. Klomfar and J. Pátek (2008). "Measurement and Correlation of the Surface Tension-Temperature Relation for Methanol." Journal of Chemical and Engineering Data **53**(9): 2233-2236.

Tang, C. Y. and H. C. Allen (2009). "Ionic Binding of Na^+ versus K^+ to the Carboxylic Acid Headgroup of Palmitic Acid Monolayers Studied by Vibrational Sum Frequency Generation Spectroscopy." Journal of Physical Chemistry A **113**(26): 7383-7393.

Tang, T. and J. C. McConnell (1996). "Autocatalytic release of bromine from Arctic snow pack during polar sunrise." Geophysical Research Letters **23**(19): 2633-2636.

Tian, C. S., S. J. Byrnes, H. L. Han and Y. R. Shen (2011). "Surface Propensities of Atmospherically Relevant Ions in Salt Solutions Revealed by Phase-Sensitive Sum Frequency Vibrational Spectroscopy." Journal of Physical Chemistry Letters **2**(15): 1946-1949.

Tobias, D. J. and J. C. Hemminger (2008). "Chemistry - Getting specific about specific ion effects." Science **319**(5867): 1197-1198.

Tuckermann, R. (2007). "Surface tension of aqueous solutions of water-soluble organic and inorganic compounds." Atmospheric Environment **41**(29): 6265-6275.

Verreault, D. and H. C. Allen (2013). "Bridging the Gap Between Microscopic and Macroscopic Views of Air/Aqueous Salt Interfaces." Chemical Physics Letters **586**: 1-9.

Vignati, E., M. C. Facchini, M. Rinaldi, C. Scannell, D. Ceburnis, J. Sciare, M. Kanakidou, S. Myriokefalitakis, F. Dentener and C. D. O'Dowd (2010). "Global scale emission and distribution of sea-spray aerosol: Sea-salt and organic enrichment." Atmospheric Environment **44**(5): 670-677.

Vogt, R., P. J. Crutzen and R. Sander (1996). "A mechanism for halogen release from sea-salt aerosol in the remote marine boundary layer." Nature **383**(6598): 327-330.

von Glasow, R. (2008). "Atmospheric chemistry - Sun, sea and ozone destruction." Nature **453**(7199): 1195-1196.

Wennberg, P. (1999). "Atmospheric chemistry - Bromine explosion." Nature **397**(6717): 299-301.

Winter, B., R. Weber, P. M. Schmidt, I. V. Hertel, M. Faubel, L. Vrbka and P. Jungwirth (2004). "Molecular Structure of Surface-Active Salt Solutions: Photoelectron Spectroscopy and Molecular Dynamics Simulations of Aqueous Tetrabutylammonium Iodide." Journal of Physical Chemistry B **108**(38): 14558-14564.

Chapter 2

2. Methods

This chapter gives an introduction into x-ray photoelectron spectroscopy and the liquid microjet endstation of the Swiss Light Source. It includes a detailed description of the endstation with two proof-of-principle measurements in conjunction with the liquid microjet setup, and a short introduction of the flow reactor used in O_3 uptake measurements.

This chapter forms part of three full papers, published as:

1. Matthew A. Brown, Amaia Beloqui Redondo, Inga Jordan, Nicolas Duyckaerts, Ming-Tao Lee, Markus Ammann et al.: A new endstation at the Swiss Light Source for ultraviolet photoelectron spectroscopy, X-ray photoelectron spectroscopy, and X-ray absorption spectroscopy measurements of liquid solutions, *Review of Scientific Instruments 2013*, *84*, *073904*.

2. Jefferson G. Pruyne, Ming-Tao Lee, Csaba Fábri, Amaia Beloqui Redondo, Armin Kleibert, Markus Ammann, Matthew A. Brown, Maria J. Krisch: The Liquid−Vapor Interface of Formic Acid Solutions in Saltwater: A Comparison of Macroscopic Surface Tension and Microscopic in Situ X-ray Photoelectron Spectroscopy Measurements, *J. Phys. Chem. C 2014*, *118, 29350−29360*

3. Matthew A. Brown, Ming-Tao Lee, Armin Kleibert, Markus Ammann, Javier B. Giorgi, Ion spatial distributions at the air− and vacuum−aqueous K_2CO_3 interfaces, *Journal of Physical Chemistry C 2015*, *119*, *4976-4982*.

2.1. Near Ambient Pressure Photoemission (NAPP)

We describe the development of a new endstation at the Swiss Light Source for *in situ* X-ray photoelectron (XP) spectroscopies of liquid solutions. The endstation can also be operated away from a synchrotron beamline with a helium (He) discharge lamp for ultraviolet photoemission (UPS) studies of the liquid−vapor interface. The design of our apparatus is unique in several ways that help to distinguish it from the liquid jet endstations at BESSY (Winter and Faubel 2006) and MAX-lab (Bergersen, Marinho et al. 2007). The first is that it can be operated under a vacuum of ca. 10^{-4} mbar and in an ambient environment at background pressures up to 20 mbar. Designed as a mobile endstation adapted for both the SIM (Flechsig, Nolting et al. 2010) and Phoenix beamlines of the Swiss Light Source, it allows for electron spectroscopy measurements from liquid solutions over an electron kinetic range that spans from 2-7000 eV. Efficient photoelectron detection from liquid samples at low energies (ca. <60 eV) is a by-product of both a measurement chamber completely shielded of magnetic fields that can disrupt photoelectron trajectories at these energies, and the development of an electrostatic lens mode that applies a biased potential to the first lens element that helps to draw the low energy photoelectrons into the high vacuum environment of the electron analyzer where the mean free path is increased. This allows for electron spectroscopy measurements down to several eV and for use with a He discharge lamp for UPS measurements from the liquid microjet.

2.2. The liquid microjet endstation of the Swiss Light Source

2.2.1. Design concept

Fig. 2.2 a. shows a picture of the liquid microjet endstation installed at the SIM (Flechsig, Nolting et al. 2010) beamline of the Swiss Light Source. At the heart of the design is a Scienta *HiPP-2* R4000 electron spectrometer with a multi-channel plate (MCP) detector. The electron spectrometer is similar to that previously described (Grass, Karlsson et al. 2010), and only features specifically relevant to the liquid microjet experiment are described here. The electron spectrometer is mounted parallel to the laboratory floor and has six electrostatic lens elements, three in the pre-lens and three in the (traditional) lens (Fig. 2.2 b.). The analyzer is rotated on its side to align the entrance slits with the direction of flow of the liquid microjet. All the components of the liquid microjet are designed to operate inside a 6-way DN-200 aluminum cube that overlaps the orthogonal incoming photon beam, liquid microjet and focal

point of the electron spectrometer at its center (Fig. 2.2 c.). The liquid microjet cube and all of its components were designed to be as compact as possible. Using a DN-200 cube improves access to the liquid microjet inside the chamber and greatly improves visibility/sight lines to the measurement area. To the top of the DN-200 cube is fitted a tee connector that houses a liquid nitrogen cold trap, used to condense water vapor and help to reduce the background chamber pressure, in the vertical position and a Agilent TwisTorr 700 turbo molecular pump in the horizontal position. For experiments conducted in ambient pressures both the LN_2 trap and the turbo pump are removed and the flange blanked off with a viewport. The flange opposite the electron spectrometer is equipped with a pressure gauge, a viewport in direct line of sight up the electron spectrometer lens, and a linear/rotation feed-through manipulator that is used to seal off the entrance to the electron spectrometer during venting. The incoming photon beam enters the DN-200 cube parallel to the floor. The opposite flange is used as a large viewport.
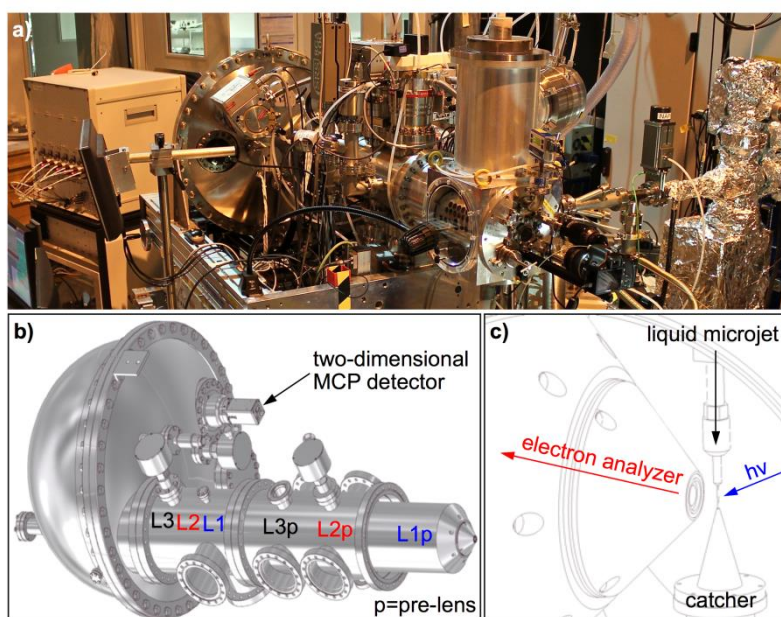

Fig. 2.2. (a) The liquid microjet endstation installed at the SIM beamline of the Swiss Light Source. (b) The Scienta *HiPP-2* R4000 electron spectrometer has six lens elements, three in the pre-lens and three in the (traditional) lens. (c) The incoming photon beam, the liquid microjet direction of flow and the electron analyzer detection axis are orthogonal with one another.

The liquid microjet is mounted on the bottom DN-200 flange (Fig. 2.2 a.). All materials are made of aluminum or titanium and are therefore free of magnetic fields. The liquid microjet consists of a titanium rod assembly and a quartz nozzle that has been described previously

(Winter and Faubel 2006). A three-axis piezo type in-vacuum motor with a step resolution of 100 nm controls the position of the liquid microjet. The motors are mounted directly to a rigid 12 mm thick motor mount that is attached to the DN-200 flange. The liquid microjet is expanded inside the vacuum chamber for ca. 1.5 cm (Fig. 2.4) before it exits the chamber through a 600 μm hole in the aluminum catcher. The catcher is directly drained out the bottom of the measurement chamber and allows for the solution under investigation to be recycled. Note that in later experiments described in *Chapters 3*, *5* and *6* the catcher has been replaced by a LN2 trap attached to the bottom flange of the cube. The remaining component mounted to the bottom flange is the spring-loaded bottom plate of the mu-metal shield that lines the DN-200 cube. A schematic representation of the mu-metal liner is shown in Fig 2.3 b. The field inside the chamber when the liquid microjet is mounted is less than 0.014 μT. In line with the simplicity of the overall setup, the mu-metal liner has been designed to allow simple access to the measurement area. The large side door can be quickly removed and provides a large enough access point to directly reach inside the chamber for minor adjustments.
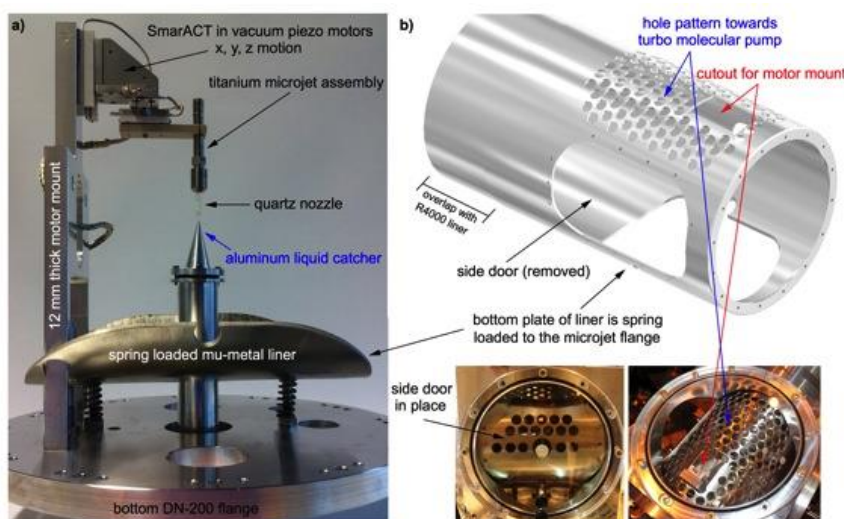

Fig. 2.3. (a) The liquid microjet and all of its components are mounted to the bottom DN-200 flange. (b) The mu-metal liner is designed to allow simple access to the measurement area. The overall magnetic field inside the liner with the liquid microjet installed is less than 15 μT.
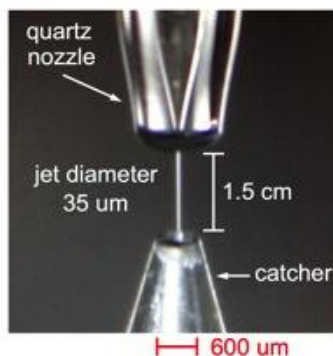
Fig. 2.4. The liquid microjet travels 1.5 cm inside the measurement chamber before it enters a 600 μm catcher and is directly drained outside the vacuum chamber where it can be recycled for further study. The diameter of the liquid microjet filament is variable, but typically in the 20-40 μm size range. The liquid filament depicted has been artificially enhanced for clarity.

2.2.2. Accelerating lens mode for low energy photoelectrons

It is difficult to develop a single electron spectrometer that is capable of detecting photoelectrons from the UV (ca. 2 eV) up to hard X-ray energies (7000 eV). Because our electron spectrometer is equipped with a gold mesh installed in the pre-lens for high-energy measurements, traditional electrostatic lens modes designed for UV energies do not perform well on our system. At energies below ca. 60 eV, photoelectrons do not efficiently pass the gold mesh and the transmission function of the electron spectrometer becomes significantly reduced. To increase the low energy transmission function of our electron spectrometer we have developed an electrostatic lens mode that applies a positive potential to the L1p (L=lens, 1=first element, p=pre-lens) element to accelerate low energy photoelectrons through the pre-lens system. The lens potentials of the accelerating 10 eV pass energy lens mode are shown in Fig. 2.5 for photoelectron kinetic energies of 2-60 eV. We have also developed similar accelerating lens modes for pass energies of 20 and 50 eV. The accelerating potential increases linearly with increasing photoelectron kinetic energy. At low energies the accelerating potential needs to be reduced to prevent an unwanted large increase in the electron spectrometer transmission function (background electrons with energies on the order of several eV are accelerated into the lens).
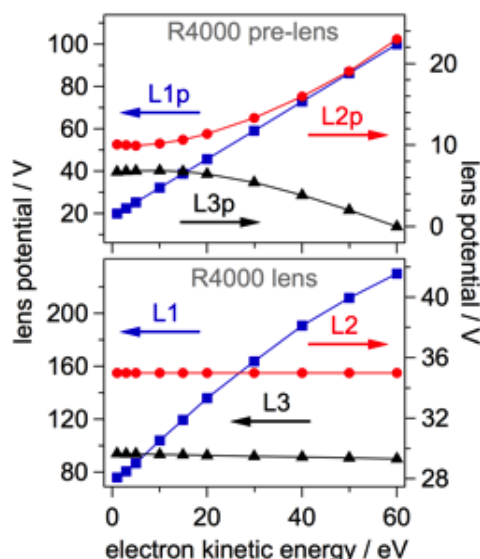
Fig. 2.5. Potentials applied to the six electrostatic lens elements of the Scienta *HiPP-2* R4000 electron spectrometer for 10 eV pass energy as a function of electron kinetic energy over the range of 2-60 eV. An accelerating potential is applied to the L1p element (see Fig. 2.2 b). At electron kinetic energies above 60 eV L1p is grounded and a traditional lens mode is employed.

2.2.3. Entrance cones

Applying a potential to the L1p element of the Scienta *HiPP-2* R4000 analyzer requires that we replace the traditional front entrance cone of the spectrometer with a truncated cone that exposes the L1p element to the measurement zone. Fig. 2.6 shows both the truncated cone and the traditional ambient pressure cone. There are noticeable differences. The entrance aperture of the ambient pressure cone is between 0.1-0.8 mm and the cone-to-sample working distance is kept small, on the order of the aperture diameter. The truncated cone has an opening of 11 mm and a working distance of 9 mm. While together the truncated cone and accelerating lens mode allow for electron spectroscopy measurements from the liquid microjet at electron kinetic energies below 60 eV the design is not without its drawbacks. The 11 mm opening of the truncated cone no longer acts as a conducting restrictive aperture and introduces an upper pressure limit of 1×10^{-2} mbar in the measurement chamber. The large opening on the truncated cone also directly exposes the pre-lens to the liquid microjet environment. Long-term effects to the condition of the pre-lens with liquid microjet exposure have demonstrated that for XPS measurements where traditional lens tables are employed it is preferable to use the traditional cones with small apertures.

Fig. 2.6. Entrance cones of the Scienta *HiPP-2* R4000 electron spectrometer used with the liquid microjet. The truncated cone exposes the L1p element to the measurement zone and allows for an accelerating field to be applied to photoelectrons below 60 eV. The working distance of the truncated cone is 9 mm. The traditional cone is used in liquid microjet studies at ambient pressure conditions up to 20 mbar and has an aperture diameter typically between 0.1 and 0.8 mm. The working distance of the traditional cone is on the order of the aperture diameter.

To avoid having to turn off the vacuum system and vent the analyzer each time the main analysis chamber is opened, i.e., to replace a clogged liquid microjet nozzle, we have designed a special 'plug' that can be positioned in front of and pressed onto the truncated cone. Fig. 2.7 shows this 'plug' that consists of a small aluminum plate that is mounted to a linear/rotation feed-through. This manner of sealing off the analyzer works well and can maintain a vacuum of 1×10^{-8} mbar at the detector with the main analysis chamber vented to ambient air. When using the traditional entrance cone the differential pumping in the pre-lens is sufficient so that the analysis chamber can be vented to ambient air while vacuum (10^{-6} mbar) is maintained in the hemisphere.
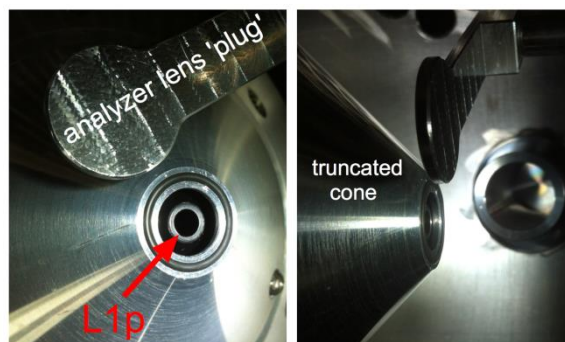
Fig. 2.7. A plug is used to seal off the electron analyzer vacuum system from the liquid microjet ionization chamber during venting and allows for quick venting of only the liquid microjet chamber. This manner of sealing off the analyzer works well and can maintain a vacuum of 1×10^{-8} mbar at the detector with the main analysis chamber vented to ambient air.

2.3. Vacuum system

Opening up the energy analyzer to the liquid microjet chamber by using the truncated entrance cone described in Section 2.2.3 introduces a significant water vapor load into the pre-lens section. Fig. 2.8 shows a schematic representation of the vacuum system and the typical pressures in the various sections of the analyzer when the liquid microjet is in operation. The vacuum system is divided into five sections: the liquid microjet chamber (ionization chamber), the first and second differential pumping sections of the pre-lens, the lens, and the hemisphere. The ionization chamber is pumped with a 700 liter/sec Agilent TwisTorr turbo molecular pump that is backed by an Agilent TriScroll 300 liter/min rough pump. Two Pfeiffer HiPace 300 liter/sec turbo molecular pumps, each of which is backed by an Adixen 600 liter/min roots pump, evacuate the first differential pumping section of the pre-lens. Two Pfeiffer HiPace 300 liter/sec turbo molecular pumps are also used to evacuate the second differential pumping section. The lens and hemisphere section of the analyzer are each pumped by a single Pfeiffer HiPace 300 liter/sec turbo molecular pump. The turbo molecular pumps of the second differential stage, the lens, and the hemisphere are backed by a single Adixen 600 liter/min roots pump.
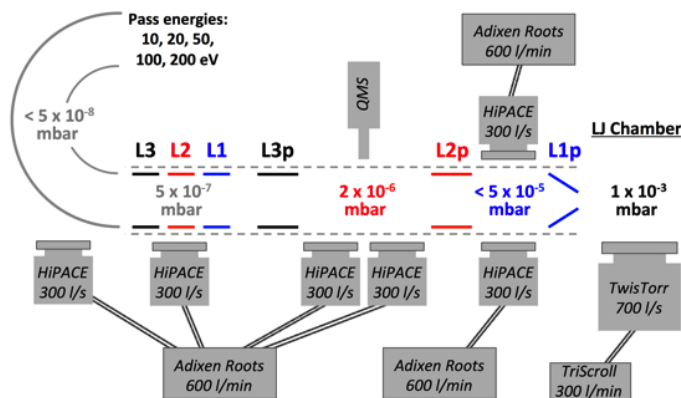
Fig. 2.8. A schematic representation of the vacuum system of the Scienta *HiPP-2* R4000 energy analyzer and the liquid microjet chamber. The pressures shown were recorded during operation of the liquid microjet with the truncated entrance cone.

The increased load brought about by using the truncated entrance cone affects predominantly the pre-lens vacuum with the lens and hemisphere sections experiencing little pressure change between liquid microjet operating conditions and when the ionization chamber is under moderate 1×10^{-6} mbar vacuum, i.e., when the liquid microjet is removed. The upper pressure limit for prolonged liquid microjet operation is 1×10^{-2} mbar above which the load on the two turbo molecular pumps of the first differential pumping section is too high. For liquid microjet experiments at pressures above 1×10^{-2} mbar the traditional entrance cone with an aperture diameter below 500 μm must be used.

2.4. Motion control of the analyzer for alignment to a beamline

The Scienta *HiPP-2* R4000 energy analyzer is mounted to an adjustable frame that allows for movement in the horizontal (x,y) and vertical (z) directions. The analyzer can be rotated in the (x,y) plane around a virtual axis passing through the analyzer focus, and tilted in the z direction. Wheels can be lowered from the frame for easy transport to and from a beamline. Commercially available motors, rails, and encoders are used for all frame movements. Linear movements in x-, y- and z- directions have a range of ± 50 mm with a resolution of 10 μm and a step reproducibility of ± 10 μm. The tilt and rotation ranges are ± 50 mrad with a resolution of 0.01 mrad and a reproducibility of ± 0.02 mrad. A Labview program offering a convenient graphical interface that allows recording frame positions controls all movements.

2.5. Proof-of-principle measurements

All experiments were performed using 20-40 μm liquid microjets operating at 279 K and at a flow rate of 0.35-0.65 ml/min. The base pressure of the measurement chamber was 1×10^{-3} mbar. PE signals from 0.5 and 1.1 M aqueous solutions of potassium carbonate (K_2CO_3) are measured by synchrotron-based X-ray photoelectron spectroscopy (XPS) in combination with a liquid microjet. Results are compared, where possible, between liquid jets running in vacuum (1×10^{-4} mbar) and jets in an equilibrated background vapor pressure that is determined by the temperature of the solution (6 mbar in this case). Ultraviolet photoelectron spectroscopy (UPS) experiments were performed using a commercial Scienta 5K UV helium discharge lamp. UPS measurements were performed using a 0.05 M solution of NaCl in combination with a liquid microjet.

2.5.1. Liquid microjet X-ray photoelectron spectroscopy

The XPS synchrotron-based experiments described here were performed at the soft X-ray SIM beamline (Flechsig, Nolting et al. 2010) of the Swiss Light Source. The liquid microjet endstation was connected to the beamline using a series of differential pumping stages separated by small apertures that allowed for windowless (e.g., silicon nitride) operation.

Aqueous solutions of 0.5 M and 1.1 M potassium carbonate (K_2CO_3, ACS Reagent, ≥99%, Sigma-Aldrich, used as-received) were prepared using Milli-Q water. The 1.1 M solution was specifically chosen to facilitate comparison with the SFG spectroscopy results of Allen and coworkers on the air−water interface structure of aqueous Na_2CO_3 (Hua, Jubb et al. 2011). The solutions pH were 12.1 (0.5 M) and 12.2 (1.1 M) as determined using a four point calibrated Mettler Toledo Expert Pro electrode.

Potassium 2p (K 2p) and carbon 1s (C 1s) photoelectron spectra were collected from a 19 μm liquid jet. The liquid jet was operated at 0.35 mL/min and at 279 K (measured immediately prior to the measurement chamber). The entrance aperture of the hemispherical energy analyzer was 0.5 mm in diameter and 0.5 mm from the liquid jet. For the experiments performed in vacuum (1×10^{-4} mbar) the liquid jet was expanded to hit a liquid nitrogen trap (immediately frozen). For experiments performed in equilibrium (6 mbar) with the temperature of the liquid jet the liquid nitrogen trap was replaced by a reservoir cooled by an ice bath, and a 200 nm thick silicon nitride (SiN_x) window was used to separate the ultra-high

vacuum of the beamline from the measurement chamber. The SiN_x window was ~3 cm from the ionization point. The pumping system was turned off in the measurement chamber.

Results are compared, where possible, between liquid jets running in vacuum (1×10^{-4} mbar) and jets in an equilibrated background vapor pressure that is determined by the temperature of the solution (6 mbar in this case). The ion spatial distributions and the molecular level pictures of the air − and vacuum−aqueous electrolyte interfaces as derived by XPS are identical.

Fig.2.9 shows the K 2p and C 1s photoelectron spectra recorded from a 19 μm vacuum (1×10^{-4} mbar) aqueous microjet of 0.5 M K_2CO_3 at photoelectron kinetic energies of (a) 132 eV, (b) 332 eV, (c) 592 eV, and (d) 752 eV.

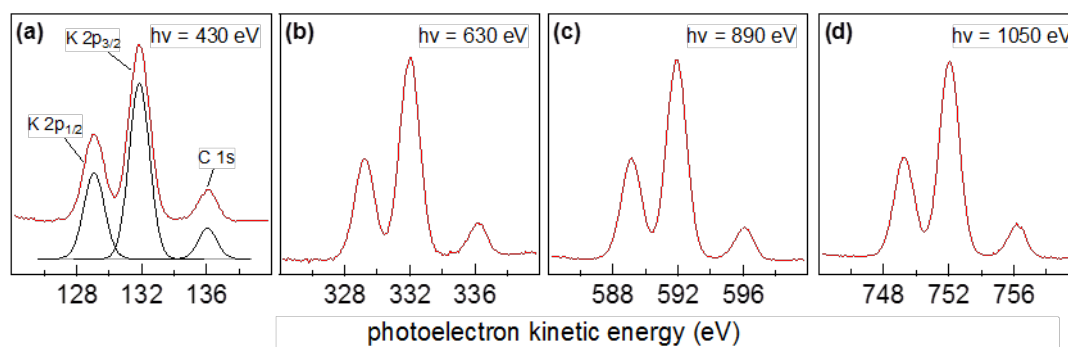**Fig. 2.9.** K 2p and C 1s spectra from 0.5 M aqueous solutions of K_2CO_3 at photoelectron kinetic energy of (**a**) 132 eV, (**b**) 332 eV, (**c**) 592 eV, and (**d**) 752 eV. The incident X-ray photon energy is shown in each panel. In **a**) are shown the fits and assignments of the three components. The y-axis is PE signal intensity given in arbitrary unit.

A depth-resolved ion stoichiometry at the vacuum−aqueous solution interface can be calculated by simply normalizing the XPS integrated K 2p and C 1s peak areas to the energy-dependent photoionization cross-sections. We have used the cross-sections calculated by Yeh and Lindau (Yeh and Lindau 1985). One major advantage of the K_2CO_3 system for XPS measurements is that the close proximity of the K 2p and C 1s orbitals means that they are collected simultaneously in the same kinetic energy window using a single photon energy (at the same depth into solution). There is, therefore, no need to normalize to photon flux (which is required if two different photon energies are used to ionize the different ions orbitals at the same photoelectron kinetic energy and would typically introduce an error) or to the transmission function of the hemispherical energy analyzer (which we assume constant over

the ~4 eV separation between orbitals). In addition, the precision of the measurements is also increased as the stability of the liquid jet is guaranteed for both orbitals. As directly apparent from the spectra taken at different photon energy, and thus different KE, the ratio of K^+ to carbon does not change. As shown in the example of KI solutions in Fig. 1.4 section 1.31, where the iodide to potassium ratio was changing strongly with KE (and thus probe depth), this result is not necessarily straightforward. Many solutions investigated thus far by liquid jet XPS show indeed pronounced depth profiles. As it turns out, the variation of the K 2p to C 1s ratio with KE observed here represents one of the weakest ion ratio profile observed thus far (Brown, Lee et al., 2015).

We have performed additional experiments for 0.5 M K_2CO_3 in an equilibrated background vapor pressure of 6 mbar. Unfortunately, the only meaningful spectra we could collect at 6 mbar were for photoelectron kinetic energies of 592 eV. At lower energies the signal to noise was not sufficient (even after averaging for 45 min) for quantitative data analysis. We attribute this to (i) lower transmission of the incident X-ray beam through the SiN_x window (Lary 1997), (ii) to greater absorption of the incident X-ray beam in the 6 mbar ambient background (which we assume to be water vapor) of the measurement chamber, (iii) to more efficient (and detrimental) scattering of the photoelectrons in the gas phase (Itikawa and Mason 2005), and (iv) to the shallower probe volume (and therefore less total ions to ionize). Fig. 2.10 shows a comparison of the spectra collected at 592 eV pKE in vacuum (1×10^{-4} mbar, red) and in ambient conditions (6 mbar, blue). Qualitatively, the relative signal intensities of the K 2p and C 1s orbitals are the same in both conditions (see difference spectrum shown in Fig. 2.10), but the signal to noise of the spectrum in ambient conditions is poor compared with that collected in vacuum. The potassium to carbonate stoichiometries, determined from curve fitting and normalization to the photoionization cross-sections, are the same for both the water vapor– aqueous and the vacuum–aqueous K_2CO_3 interfaces at 592 pKE. Several conclusions can be drawn from these results. First, in order to interrogate the water interface at energies near the minimum in the photoelectron escape depth (maximum sensitivity to the water interface) measurements are best performed in vacuum (for this particular system at 6 mbar the signal to noise is too low to give meaningful spectra). Second, at pKE's where measurements are possible in both environments the ion spatial distributions of K^+ and CO_3^{2-} measured at the vacuum−water interface are equivalent to those measured at the air−water interface. This finding gives support to the argument that the liquid microjet in vacuum is in a local equilibrium (Faubel, Steiner et al. 1997, Winter and Faubel 2006).
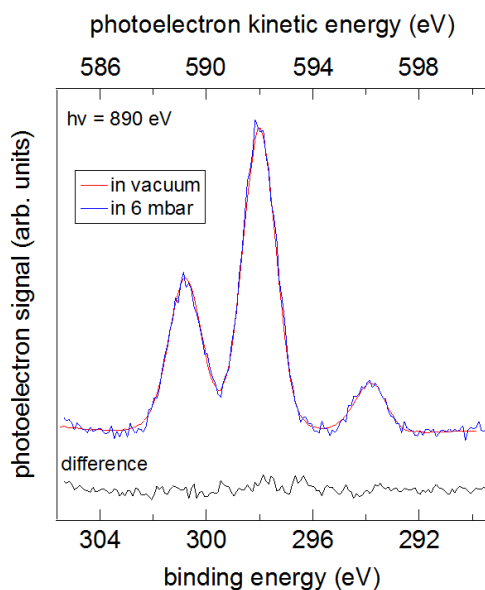
Fig. 2.10. Comparison between the signals obtained in vacuum (1×10^{-4} mbar, red) to that recorded with an equilibrated background vapor pressure (6 mbar, blue) for 0.5 M K_2CO_3 at a photoelectron kinetic energy of 592 eV. The difference spectrum shows that the signals are essentially identical. The lower signal-to-noise ratio from the 6 mbar experiment is a product of significantly reduced signal strength (see text).

2.5.2. Ultraviolet photoelectron spectroscopy

UPS experiments were performed using a commercial Scienta 5K UV helium discharge lamp. The platinum coated toroidal type monochromator (80 x 30 mm, 1200 lines/mm) was set to select the He II α line at 40.8 eV. Our experiments use a ca. 300 μm quartz capillary to focus the UV light onto the liquid microjet. The working distance is kept small, on the order of 2 mm. At this working distance the UV spot size is 350 μm. As discussed and shown below in Fig. 2.11 the relatively large spot size compared with the diameter of the liquid microjet results in a significant contribution to the spectral intensity from the gas phase that makes spectral interpretation more cumbersome. Measurements were performed using a 0.05 M solution of NaCl with the truncated entrance cone.

Valence band photoemission spectra from a liquid microjet of 0.05 M NaCl are shown in Fig. 2.11. The top spectrum, labeled 'gas + liquid', is obtained when the liquid filament is in the optimal focal position in front of the energy analyzer and the UV source spot. The spectrum is a combination of both condensed water of the liquid microjet and gas phase water in the background volume of the chamber. The major contribution of the gas phase arises because the spot size of the UV source at 350 μm is much larger than that of the liquid microjet at 28

µm. The second spectrum in Fig. 2.11, labeled 'gas', is collected by displacing the liquid microjet filament 500 µm away from the focal plane of the energy analyzer and out of the UV source spot. In this manner only gas phase water is excited and the spectrum is noticeably different than that obtained for 'gas + liquid'. By taking the difference of these two spectra the valence band signature of pure liquid water is obtained. Assignments to the three orbital components in the spectrum labeled 'liquid (difference)' are based on the work of Winter and coworkers (Winter, Weber et al. 2004). We are at present designing smaller focusing capillaries that will reduce the UV spot size and in turn reduce the contribution from the gas phase.
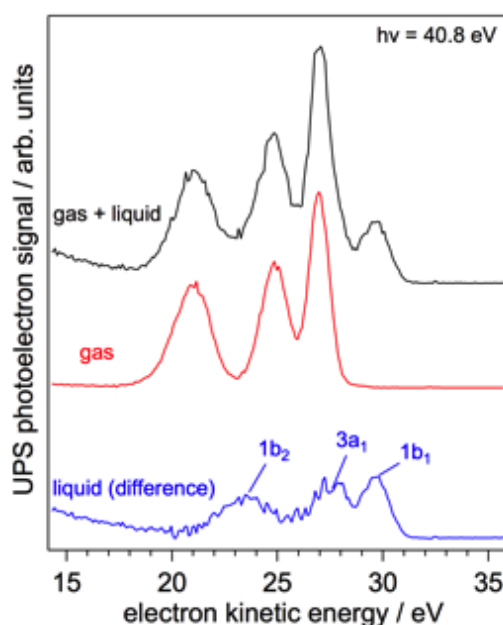

Fig. 2.11. Ultraviolet photoemission spectra recorded using He II α excitation at 40.8 eV from a liquid microjet of 0.05 M NaCl. The top spectrum is recorded with the liquid microjet in the focal plane of the electron analyzer and consists of both liquid and gas phase water. The gas phase spectrum is recorded by displacing the liquid microjet filament 500 µm away from the electron analyzer focus and out of the incident photon path. The difference spectrum provides the signature of liquid water (Winter, Weber et al. 2004).

2.6. Flow reactor used in ozone uptake measurements

How do atmospheric scientists measure rates of uptake of trace gases to condensed phase substrates? A number of experimental methods for measuring trace gas uptake on condensed-phase-surfaces have been developed. Here we list the most commonly used ones: coated (wetted) wall flow tube, bubble train, droplet train, Knudsen cell, and ambient pressure

aerosol flow tube reactors, and molecular beam scattering chambers for both solid and liquid substrates, single suspended droplet/laser probe methods etc. (Kolb, Cox et al. 2010). In usual applications of these methods, the loss of the gas phase species of interest is monitored as a function of the gas – surface interaction time. Some of them in addition allow determining the appearance kinetics of products in the condensed phase or their chemically selective analysis. Each of them is applicable for specific ranges of surface area to volume ratios, kinetic regimes and net rate of uptake. A more thorough elaboration of the various methods can be found in Kolb, Worsnop et al. (1995) and Davidovits, Kolb et al. (2006).

The purpose of the flow reactor in this thesis was motivated by the need to investigate the impact of organic constituents on the interaction of O_3 with aqueous solutions of Br^-. While traditionally, this kind of experiment has been performed in a wetted wall flow tube, which are either rotated or which feature the aqueous solution flowing down as a liquid film along the flow tube walls. Since for the applications envisaged in this thesis and follow-up projects, the application of surfactants (including also insoluble surfactants) required a stagnant solution surface. The design thus more followed that of Langmuir troughs (ref to Knopf paper). A schematic diagram of our flow reactor with a quartz trough is shown in Fig. 2.12. After about 1 h of stabilizing the background O_3 concentration (dotted arrow in Fig. 2.12), the bypass is switched to experimental mode (solid arrow) which leads to exposure of the film to O_3 allowing the heterogeneous reactions to take place. Finally, the concentration after the reactor is measured in by-pass mode (dotted arrow) again at the end of the experiment to confirm that the background has not changed during the course of the experiment.
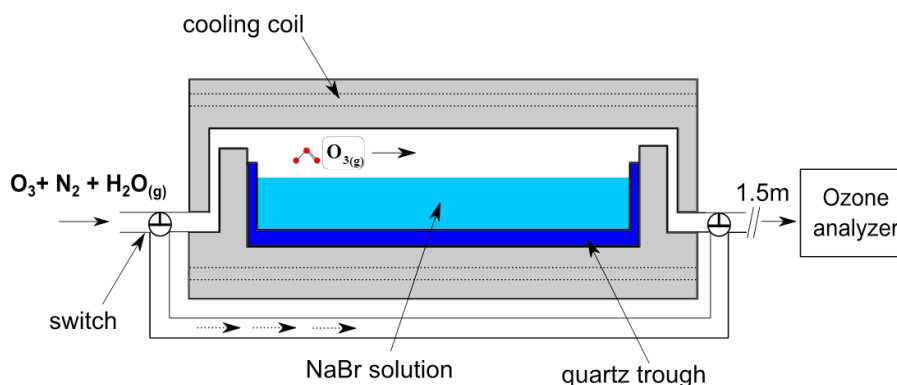

Fig. 2.12. A Schematic diagram of the flow reactor used in O_3 uptake measurements to solutions filled into a quartz trough.

Fig. 2.13 shows exemplary raw data of O_3 uptake to an aqueous solution composed of 0.12 M NaBr at 15.7°C shown as O_3 concentration in the gas phase against exposure time. The valves are turned to expose the solution at 0 min. and 33 min. and back to bypass at 25 min. and 67 min., respectively. The blue arrows show the difference in O_3 concentration interpreted as O_3 loss to the solution. The dashed lines connect the bypass measurements to indicate the drift of the background concentration that was taken into account in the determination of the O_3 loss.
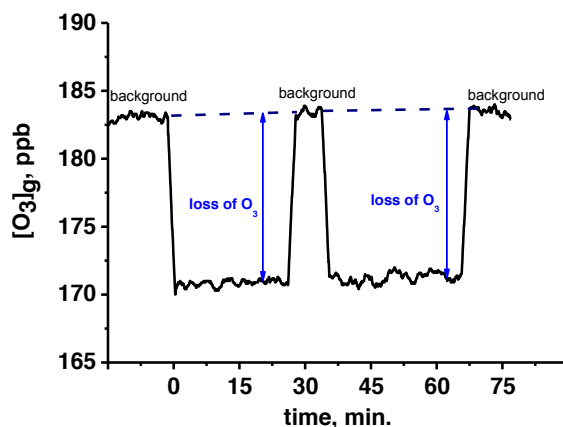

Fig. 2.13. Exemplary raw data of O_3 uptake to an aqueous solution composed of 0.12 M NaBr at 15.7°C shown as O_3 concentration vs. exposure time.

2.7. Conclusion and outlook

In this chapter, the liquid microjet endstation that has been installed at the Swiss Light Source has been presented. In addition, a flow reactor has been developed for complementary kinetic experiments in our laboratory. First measurements at the soft X-ray SIM beamline (XPS), and using a He II α source (UPS) were shown. Performing XPS measurements over a broad energy range from 1000 eV down to 15 eV allows for a depth resolved analysis of the solution composition near the air −water interface.

In summary, near ambient pressure XPS measurements from a the liquid jet in equilibrium with a background vapor pressure of water were shown to give the same results as those performed under the more traditional vacuum (1×10^{-4} mbar) environment of XPS. While it is difficult to generalize these results to all systems of interest, in particular those that contain a solute with a high propensity for the water interface (e.g., a surfactant), it should be clear from the current results that for aqueous solutions of electrolyte ions with weak interface

propensity the molecular level pictures of the near interface region (≈3.5 nm) derived from XPS in vacuum are analogous to those in ambient humidity.

UPS measurements neatly reproduce the shape of the valence band for liquid water by taking a difference spectrum from that of 'gas + liquid' to 'gas', the latter of which is recorded by offsetting the liquid microjet out of the UV source spot. At present, the relatively large spot size of our current setup will prevent the trivial assignment of electronic structures with binding energies above the onset of liquid water. However, solutes with electronic structures below the onset of liquid water, such as halide ions (Winter 2009), will be easily distinguishable.

Accomplished developments involve interfacing the Scienta *HiPP-2* R4000 energy analyzer with the beamline control systems to allow for incident photon energy scans that permits broad and continuous energy XAS measurements. Ambient pressure liquid microjet experiments that operate at the room temperature i.e. 20 °C vapor pressure of the solution under study is underway. These measurements use the traditional entrance cone and therefore do not allow for the use of the accelerating lens modes for low energy photoelectron detection. High-energy measurements increase the probe depth of the experiment and allow for electronic structure measurements of bulk solutions.

The proof-of-principle measurements have shown the applicability from UV photoemission to soft X-ray photoemission. However, the analyzer can cover kinetic energies up to 7000 eV. The NAPP endstation is prepared to fit to the PHOENIX beamline at SLS for X-ray energies between 2000 and 7000 eV, but so far only be used with a solid sample (Kato, Ammann et al. 2015).

Our Scienta *HiPP-2* R4000 electron spectrometer is also outfitted with a solid-state chamber, when the liquid microjet is removed, that will allow *in situ* electron spectroscopy measurements at the gas−solid interface under pressure conditions up to ca. 100 mbar. This chamber has already been tested with ice, deliquesced salts and titania under humid conditions (Orlando and Waldner 2015).

Finally, the flow reactor used in O_3 uptake measurements (see *chapter 5*) to solutions filled into a quartz trough was introduced, which will allow kinetic experiments with the same solutions as probed in LJ XPS experiments.

References

Bergersen, H., R. R. T. Marinho, W. Pokapanich, A. Lindblad, O. Bjorneholm, L. J. Saethre and G. Ohrwall (2007). "A photoelectron spectroscopic study of aqueous etrabutylammonium iodide." Journal of Physics-Condensed Matter **19**(32).

Brown, M. A., B. Winter, M. Faubel and J. C. Hemminger (2009). "Spatial Distribution of Nitrate and Nitrite Anions at the Liquid/Vapor Interface of Aqueous Solutions." Journal of the American Chemical Society **131**(24): 8354-8355.

Brown, M. A., F. Vila, M. Sterrer, S. Thuermer, B. Winter, M. Ammann, J. J. Rehr and J. A. van Bokhoven (2012). "Electronic Structures of Formic Acid (HCOOH) and Formate (HCOO-) in Aqueous Solutions." Journal of Physical Chemistry Letters **3**(13): 1754-1759.

Brown, M. A., I. Jordan, A. Beloqui Redondo, A. Kleibert, H. J. Wörner and J. A. van Bokhoven (2013). "In Situ Photoelectron Spectroscopy at the Liquid/Nanoparticle Interface." Surface Science **610**: 1-6.

Brown, M. A., M. Faubel and B. Winter (2009). "X-Ray Photo- and Resonant Auger-Electron Spectroscopy Studies of Liquid Water and Aqueous Solutions." Annual Reports Section "C" (Physical Chemistry) **105**(0): 174-212.

Brown, M. A., R. D'Auria, I. F. W. Kuo, M. J. Krisch, D. E. Starr, H. Bluhm, D. J. Tobias and J. C. Hemminger (2008). "Ion spatial distributions at the liquid-vapor interface of aqueous potassium fluoride solutions." Physical Chemistry Chemical Physics **10**(32): 4778-4784.

Davidovits, P., C. E. Kolb, L. R. Williams, J. T. Jayne and D. R. Worsnop (2006). "Mass accommodation and chemical reactions at gas-liquid interfaces." Chemical Reviews **106**(4): 1323-1354.

Faubel, M., B. Steiner and J. P. Toennies (1997). "Photoelectron Spectroscopy of Liquid Water, Some Alcohols, and Pure Nonane in Free Micro Jets." Journal of Chemical Physics **106**(22): 9013-9031.

Flechsig, U., F. Nolting, A. F. Rodriguez, J. Krempasky, C. Quitmann, T. Schmidt, S. Spielmann and D. Zimoch (2010). "Performance Measurements at the SLS SIM Beamline." AIP Conference Proceedings **1234**: 319-322.

Ghosal, S., M. A. Brown, H. Bluhm, M. J. Krisch, M. Salmeron, P. Jungwirth and J. C. Hemminger (2008). "Ion Partitioning at the Liquid/Vapor Interface of a Multicomponent Alkali Halide Solution: A Model for Aqueous Sea Salt Aerosols." Journal of Physical Chemistry A **112**(48): 12378-12384.

Grass, M. E., P. G. Karlsson, F. Aksoy, M. Lundqvist, B. Wannberg, B. S. Mun, Z. Hussain and Z. Liu (2010). "New ambient pressure photoemission endstation at Advanced Light Source beamline 9.3.2." Review of Scientific Instruments **81**(5).

Hua, W., A. M. Jubb and H. C. Allen (2011). "Electric Field Reversal of Na2SO4, NH4)(2)SO4, and Na2CO3 Relative to CaCl2 and NaCl at the Air/Aqueous Interface Revealed by Heterodyne Detected Phase-Sensitive Sum Frequency." Journal of Physical Chemistry Letters **2**(20): 2515-2520.

Itikawa, Y. and N. Mason (2005). "Cross Sections for Electron Collisions with Water Molecules." Journal of Physical and Chemical Reference Data **34**(1): 1-22.

Jungwirth, P. and Winter, B. Ions at Aqueous Interfaces: From Water Surface to Hydrated Proteins. Annu. Rev. Phys. Chem. 2008, **59**, 343-366.

Kato, S., M. Ammann, T. Huthwelker, C. Paun, M. Lampimaeki, M.-T. Lee, M. Rothensteiner and J. A. van Bokhoven (2015). "Quantitative depth profiling of Ce3+ in Pt/CeO2 by in situ high-energy XPS in a hydrogen atmosphere." Physical Chemistry Chemical Physics **17**(7): 5078-5083.

Kolb, C. E., D. R. Worsnop, M. S. Zahniser, W. J. DeBruyn, J. A. Shorter and P. Davidovits (1995). Heterogeneous atmospheric chemistry of alternative halocarbon oxidation intermediates. Halon Replacements: Technology and Science. A. W. Miziolek and W. Tsang. **611:** 50-58.

Kolb, C. E., R. A. Cox, J. P. D. Abbatt, M. Ammann, E. J. Davis, D. J. Donaldson, B. C. Garrett, C. George, P. T. Griffiths, D. R. Hanson, M. Kulmala, G. McFiggans, U. Poeschl, I. Riipinen, M. J. Rossi, Y. Rudich, P. E. Wagner, P. M. Winkler, D. R. Worsnop and C. D. O' Dowd (2010). "An overview of current issues in the uptake of atmospheric trace gases by aerosols and clouds." Atmospheric Chemistry and Physics **10**(21): 10561-10605.

Krisch, M. J., R. D'Auria, M. A. Brown, D. J. Tobias, J. C. Hemminger, M. Ammann, D. E. Starr and H. Bluhm (2007). "The Effect of an Organic Surfactant on the Liquid-Vapor Interface of an Electrolyte Solution." Journal of Physical Chemistry C **111**(36): 13497-13509.

Le Guyader, L.; Kleibert, A.; Rodriguez, A. F.; El Moussaoui, S.; Balan, A.; Buzzi, M.; Raabe, J.; and Nolting, F. "Studying nanomagnets and magnetic heterostructures with X-ray PEEM at the Swiss Light Source". J. Electron Spectrosc. Relat. Phenom. 2012, **185**, 371-380.

See http://www.psi.ch/sls for specifications and operational performance of the Swiss Light Source.

Seidel, R., S. Thuermer and B. Winter (2011). "Photoelectron Spectroscopy Meets Aqueous Solution: Studies from a Vacuum Liquid Microjet." Journal of Physical Chemistry Letters **2**(6): 633-641.

Siegbahn, H. and Seibahn, K. "ESCA applied to liquids". J. Electron Spectros. Relat. Phenom. 1973, **2**, 319-325.

Siegbahn, H., L. Asplund, P. Kelfve and K. Siegbahn (1975). "ESCA APPLIED TO LIQUIDS .3. ESCA PHASE-SHIFTS IN PURE AND MIXED ORGANIC-SOLVENTS." Journal of Electron Spectroscopy and Related Phenomena **7**(5): 411-419.

Siegbahn, H., S. Svensson and M. Lundholm (1981). "A NEW METHOD FOR ESCA STUDIES OF LIQUID-PHASE SAMPLES." Journal of Electron Spectroscopy and Related Phenomena **24**(2): 205-213.

Starr, D. E., E. K. Wong, D. R. Worsnop, K. R. Wilson and H. Bluhm (2008). "A combined droplet train and ambient pressure photoemission spectrometer for the investigation of liquid/vapor interfaces." Physical Chemistry Chemical Physics **10**(21): 3093-3098.

Winter, B. and Faubel, M. "Photoemission from Liquid Aqueous Solutions". Chem. Rev. 2006, **106**, 1176-1211.

Winter, B. "Liquid microjet for photoelectron spectroscopy". Nucl. Instrum. Methods Phys. Res. 2009, A, **601**, 139-150.

Winter, B. and M. Faubel (2006). "Photoemission from liquid aqueous solutions." Chemical Reviews **106**(4): 1176-1211.

Winter, B., M. Faubel, I. V. Hertel, C. Pettenkofer, S. E. Bradforth, B. Jagoda-Cwiklik, L. Cwiklik and P. Jungwirth (2006). "Electron binding energies of hydrated H3O+ and OH-: Photoelectron spectroscopy of aqueous acid and base solutions combined with electronic structure calculations." Journal of the American Chemical Society **128**(12): 3864-3865.

Winter, B., R. Weber, W. Widdra, M. Dittmar, M. Faubel and I. V. Hertel (2004). "Full Valence Band Photoemission From Liquid Water Using Euv Synchrotron Radiation." Journal of Physical Chemistry A **108**(14): 2625-2632.

Yeh, J. J. and I. Lindau (1985). "ATOMIC SUBSHELL PHOTOIONIZATION CROSS-SECTIONS AND ASYMMETRY PARAMETERS - 1 LESS-THAN-OR-EQUAL-TO Z LESS-THAN-OR-EQUAL-TO 103." Atomic Data and Nuclear Data Tables **32**(1): 1-155.

Chapter 3

3. The Liquid−Vapor Interface of Formic Acid Solutions in Saltwater: A Comparison of Macroscopic Surface Tension and Microscopic *in Situ* X-ray Photoelectron Spectroscopy Measurements

3.1. Abstract

The liquid−vapor interface is difficult to access experimentally but is of interest from a theoretical and applied point of view, and has particular importance in atmospheric aerosol chemistry. Here we examine the liquid−vapor interface for mixtures of water, sodium chloride, and formic acid, an abundant chemical in the atmosphere. We compare the results of surface tension and X-ray photoelectron spectroscopy (XPS) measurements over a wide range of formic acid concentrations. Surface tension measurements provide a macroscopic characterization of solutions ranging from 0 to 3 M sodium chloride and from 0 to over 0.5 mole fraction formic acid. Sodium chloride was found to be a weak salting out agent for formic acid with surface excess depending only slightly on salt concentration. *in situ* XPS provides a complementary molecular level description about the liquid−vapor interface. XPS measurements over an experimental probe depth of 51 Å gave the C 1s to O 1s ratio for both total oxygen and oxygen from water. Our data are consistent with surface tension measurements yielding a significantly more surface sensitive measurement than XPS due to the relatively weak propensity of formic acid for the interface. A simple model allowed us to replicate the XPS results under the assumption that the surface excess was contained in the top four angstroms of solution.

3.2. Introduction

The liquid-vapor interfacial region exhibits properties distinct from both bulk liquid and vapor but selectively probing it presents an experimental challenge as many surface-selective experimental techniques require high or ultra-high vacuum for use and cannot be easily applied to liquids with reasonable vapor pressures. Only over the past twenty years has progress been made in the development of surface selective methods that can be used with high vapor pressure liquids such as water. These developments have resulted in detailed descriptions of the liquid−vapor interface with methods such as surface-selective non-linear spectroscopy (Petersen and Saykally 2006, Jubb, Hua et al. 2012), scattering experiments (Nathanson 2004), and X-ray photoelectron spectroscopy (XPS) (Winter and Faubel 2006). This paper aims to compare the characterization of the interface provided by the older, macroscopic approach of surface tension measurements to the molecular scale technique of XPS. These methods are known to provide complementary information about the liquid−vapor interface and have been paired for this reason in previous work (Krisch, D'Auria

et al. 2007, Kolbeck, Lehmann et al. 2010). There is only one study we are aware of (Ottosson, Wernersson et al. 2011); however, quantitatively comparing results of the two methods over a range of solution compositions as we present here.

The interesting properties of the liquid−vapor interface stem from the fact that this region is inherently an asymmetric environment, which impacts both structure and reactivity. The liquid−vapor interface shows large changes over angstrom-scale distances in properties such as molecular composition, orientation, and density. These qualities can lead to differences in structure and chemistry between the interfacial region and the bulk (Eisenthal 1993, Petersen and Saykally 2006). With acids and bases, for example, it has become apparent that the interfacial pH can be either more acidic or more basic than the bulk liquid, depending upon the system under examination (Petersen, Iyengar et al. 2004, Buch, Milet et al. 2007, Lewis, Winter et al. 2011). Quantifying these unique properties of the liquid−vapor interface is of practical interest to many fields. For example, chemical reactions in the atmosphere frequently occur within atmospheric aerosol, which have high surface to volume ratios. A major fraction of atmospheric aerosols are highly concentrated solutions. In several important cases, reactions between gas and aerosol phase species have a substantial surface component, meaning that a reaction channel exists that occurs exclusively at the surface (Ammann, Cox et al. 2013). Differences between the bulk and the liquid−vapor interface in this type of system can have an overall impact on the net chemistry of the atmosphere.

Surface tension (γ) gives a macroscopic picture of the composition of the interface. In the thermodynamic development of surface tension, it is directly related by the Gibbs equation to the surface excess, Γ_i, of a component i beyond a theoretical dividing plane (referred to as the Gibbs surface) placed parallel to the solution surface: (Adamson 1976)

$$\Gamma_i = -\frac{a_i}{RT}\left(\frac{\partial \gamma}{\partial a_i}\right)_{T,a_j \neq i} \tag{3.1}$$

where a_i is the chemical activity of component i, R is the universal gas constant and T is temperature in Kelvin. In solutions containing multiple species, different molecular arrangements can give rise to similar measures of surface tension, complicating direct interpretation of the results. Treatment of the surface tension for these mixtures has been detailed in the literature (Sorjamaa, Svenningsson et al. 2004, Tuckermann 2007, Schwier,

Viglione et al. 2013) while a useful review of the interpretation of results is given by Jungwirth and Tobias (Jungwirth and Tobias 2006). Multiple experimental approaches can be used to quantify surface tension but in comparison studies the Wilhelmy plate method has emerged as an accurate and robust approach (Padday and Russell 1960, Soucková, Klomfar et al. 2008). The surface tension is a key parameter in determining atmospheric aerosol nucleation and growth as well as in cloud droplet nucleation by aerosol particles (Li, Williams et al. 1998, Sorjamaa, Svenningsson et al. 2004).

X-ray photoelectron spectroscopy is surface-specific due to the short inelastic mean free path (IMFP) of (photo)electrons in condensed matter. While the X-rays penetrate the interface over large depths, on the μm length scale, photoelectrons can only escape without loss of energy from several nm. The technique provides a means to quantify elemental composition that is sensitive to molecular environment and oxidation state. In this paper a liquid jet is used for XPS of aqueous solutions of formic acid.

Formic acid, HCOOH, is one of the most abundant oxygenated volatile organic compounds in the atmosphere resulting from photooxidation of volatile organic compounds (Khare, Kumar et al. 1999). Its persistence in the atmosphere is related to its long photolytic lifetime. It contributes substantially to the acidity of aerosol particles, cloud droplets and precipitation. In the context here it also serves as a simple surfactant system. Surfactants are considered important in atmospheric chemistry to affect the surface tension and gas − particle exchange rates (Donaldson and George 2012). The specific acidic environment potentially induced by acids at the liquid−gas interface may be related to novel acid-catalyzed chemistry recently discovered (Enami, Hoffmann et al. 2008).

Formic acid is an appealing system from an experimental viewpoint as well. It is fully miscible with water, allowing for a wide range of solution compositions to be studied. It contains only one carbon, which simplifies interpretation of XP spectra. As the smallest possible carboxylic acid it serves as a well-studied simple benchmark for assessing the behavior of carboxylic acids. The properties of its liquid−vapor interface are relatively well characterized from previous studies. Vibrational sum frequency spectroscopy has been applied to a wide range of formic acid-water mixtures as described by Johnson et al (Johnson, Tyrode et al. 2009). This study found that the surface formic acid existed exclusively in the neutral form. Furthermore, the study found the structure of the surface water to be significantly disturbed by the formic acid beginning at 0.2 mole fraction, while at higher

concentrations (~0.5 mole fraction) changes in the spectra could potentially be explained by the presence of dimers at the interface, although other explanations could also describe the observed behavior. In gas phase, the dimer form of formic acid has been observed (Singleton, Paraskevopoulos et al. 1987), while in the neat liquid clusters of various sizes (including dimers and larger polymers) have been reported (Pajak and Szcześniak 1977, Imberti and Bowron 2010). Dimers have been observed even at low concentrations; for 1 M (0.02 mole fraction) formic acid solutions the amount of molecules in dimer form was estimated to be between 1 and 5 % (Chmielewska, Wypych-Stasiewicz et al. 2007). Photoelectron spectroscopy has been used on the liquid−vapor interface of formic acid water solutions in two previous studies, both of which found formic acid to be enhanced at the liquid−vapor interface as compared to the bulk (Ottosson, Wernersson et al. 2011, Brown, Vila et al. 2012). Despite this enhancement, formic acid is a comparatively weak surfactant, so its presence in both bulk and surface regions of the liquid can be easily accessed via XPS. By examining this system over a wide range of solution composition with both surface tension measurements and XPS we are able to compare the relative surface sensitivity of the two techniques.

3.3. Experimental section

Surface tension measurements. Surface tension measurements data were provided by the group of Maria Krisch from the Trinity College, Hartford, Connecticut, United States.

O 1s XPS peak fitting. The O 1s photoelectron spectra were fit in two different manners that provide different information. The first and the more basic approach, fits the entire O 1s envelop with only two components. One is assigned to gas phase at high binding energy (BE) and the second at lower BE accounts for all condensed liquid in the liquid microjet, H_2O and HCOOH. This approach does not explicitly account for the oxygen contribution of the formic acid in solution, and therefore cannot provide a measured formic acid mole fraction. However, it is significantly more straightforward than the second approach, requires fewer assumptions, and provides the same results as the second fitting routine, within the experimental uncertainty, for C 1s to O 1s elemental ratios and BE peak positions at all but the highest concentration of formic acid studied by XPS. In the second approach, the contributions from the two different oxygen atoms of formic acid are explicitly included in the O 1s. The spacing between these two components, the one at higher binding energy originating from the C=O, and the one at lower BE from C-OH, is determined from gas phase measurements of formic

acid to be 1.6 eV. In order to include the two O 1s signals from formic acid, which are weak in intensity relative to water, the contribution from water is fit using the shape and full width at half maximum (FWHM) obtained from the fit of pure liquid water (0.05 M NaCl, no formic acid). Important to note is that this second approach to the fit of the O 1s has only been extended down to mole fraction 5.4×10^{-3}, below this it is not possible to explicitly include formic acid contributions. At mole fractions greater than 9.1×10^{-3} a gas phase component for formic acid is also included in the O 1s fit. Here the relative intensity, gas phase to condensed formic acid, has been determined from the C 1s spectral region and applied to the O 1s region. This approach will (slightly) overestimate the gas phase O 1s intensity of formic because the C 1s region is taken at lower photoelectron kinetic energy (probing less volume into the liquid jet) than that of the O 1s region. The width and shape of gas phase O 1s peaks of formic acid are taken to be the same as the gas phase H_2O peak.

3.4. Experimental results

The O 1s and C 1s XP regions from a liquid microjet of 0.05 M NaCl (no formic acid) are shown in Fig. 3.1 a and 3.1 b. The O 1s region is fit by two components that are assigned as $H_2O_{(gas)}$ at higher BE and $H_2O_{(liq)}$ at lower BE. The C 1s region from this sample is entirely free of intensity, highlighting one of the benefits of using a fast moving liquid microjet as a continuously refreshed interface. The O 1s and C 1s regions, including the spectral deconvolutions according to approach 2 described in the experimental section, are shown in Fig. 3.1 for formic acid mole fractions of 5.4×10^{-3} (c, d), 9.1×10^{-3} (e, f), 1.84×10^{-2} (g, h), 1.00×10^{-1} (i, j), and 2.24×10^{-1} (k, l). The explicit contribution of formic acid to the O 1s region are shown in the insets of (c) and (e) for mole fractions of 5.4×10^{-3} and 9.1×10^{-3}, respectively. At higher concentrations its contribution becomes apparent. At concentrations below 5.4×10^{-3} mole fraction formic acid the C 1s region is fit by a single component assigned to $HCOOH_{(liq)}$ (not shown). As the concentration of formic acid is progressively increased a second component at higher BE becomes noticeable in the C 1s region that can be assigned to formic acid in the gas phase, $HCOOH_{(gas)}$. Its spectral contribution reaches 25.8 % by 2.24×10^{-1} mole fraction, however this value reflects the experimental geometry of our liquid microjet setup, and will vary depending on the spatial overlap of the liquid microjet and the synchrotron radiation.
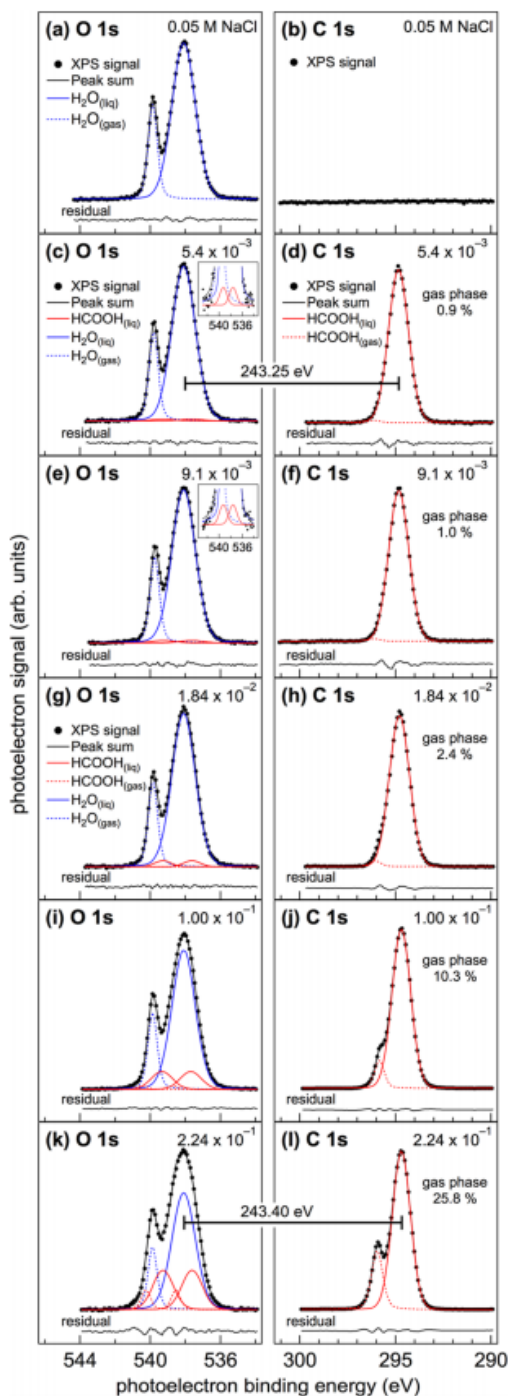
Fig. 3.1. XP spectra from a liquid microjet of aqueous solutions of formic acid. The O 1s (left side) and C 1s (ride side) regions are shown. (**a**, **b**) From a solution of 0.05 M NaCl that has no formic acid. (**c**, **d**) Formic acid mole fraction of 5.4×10^{-3}, (**e, f**) 9.1×10^{-3}, (**g**, **h**) 1.84×10^{-2}, (**i, j**) 1.00×10^{-1}, (**k**, **l**) 2.24×10^{-1}. The fits are from approach 2 described in the experimental section. The experimental data points are denoted by black markers while different components of the fit are shown by lines distinguished by the legend. The differences in BE between the O 1s of $H_2O_{(liq)}$ and the C 1s of $HCOOH_{(liq)}$ are shown for 5.4×10^{-3} and 2.24×10^{-1} formic acid mole fractions.

The relative concentration of formic acid within the probe volume of the XPS experiment can be determined from the ratio of the integrated peak areas for C 1s HCOOH$_{(liq)}$ and O 1s$_{(liq)}$. However, because the photon fluxes and hemispherical energy analyzer transmission functions are not precisely known for the conditions of the experiment the measured values cannot be normalized to yield an absolute formic acid concentration. Nevertheless, for the purposes of this study, and to compare the increase in interface concentration of formic acid as a function of bulk concentration with those obtained from surface tension measurements, the relative signal intensity is sufficient. Two different experimental ratios, one for both approaches used to fit the O 1s region, are shown in Fig. 3.2 and summarized in Table 3.1. Using the first fitting approach (black circular markers), where the entire condensed phase liquid component of the O 1s region is fit with a single component that does not distinguish between water and formic acid, results for each formic acid mole fraction investigated are obtained. In the second fitting approach (red square markers), where liquid water and formic acid are explicitly fit, results for mole fractions greater than 5.4×10^{-3} are obtained. As was noted earlier, both fitting approaches yield identical results within the uncertainty of the experiment at all formic acid mole fractions except for the highest. At 2.24×10^{-1} mole fraction formic acid the second fitting approach gives an increased ratio relative to fitting approach one. This stems from the obvious decrease in H$_2$O at such high formic acid mole fraction relative to that of pure water.
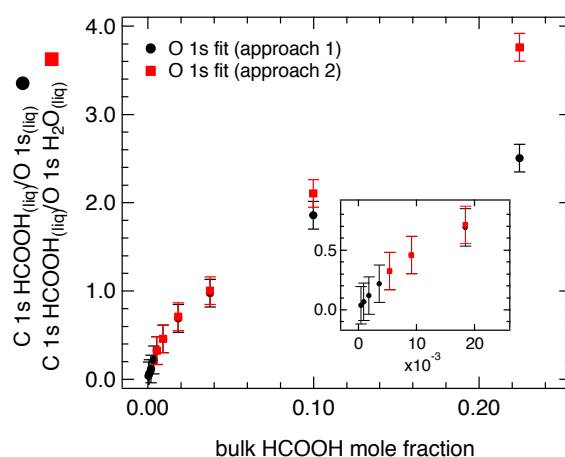

Fig. 3.2. Relative concentration of formic acid in the probe volume of the XPS experiment. There are two data sets, representing both fitting approaches to the O 1s region, as explained in the text. The inset shows the low concentration region.

Table 3.1. A summary of the C/O$_{tot}$ and C/O$_{water}$ ratios derived from XPS data fits of the type shown in Fig. 3.1.

Prepared mole fraction	pH	C1s HCOOH$_{(liq)}$/O1s H$_2$O$_{(liq)}$ ratio[a]	C 1s HCOOH$_{(liq)}$/O 1s$_{(liq)}$ ratio[b]
		[arb. units]	[arb. units]
4.5×10^{-4}	2.8		0.04
9.0×10^{-4}	2.6		0.07
1.8×10^{-3}	2.5		0.12
3.6×10^{-3}	2.3		0.22
5.4×10^{-3}	2.2	0.33	0.33
9.1×10^{-3}	2.1	0.46	0.46
1.84×10^{-2}	1.9	0.71	0.69
3.75×10^{-2}	1.7	1.00	0.98
1.00×10^{-1}	1.2	2.11	1.86
2.24×10^{-1}	0.5	3.76	2.51

[a]Calculated using the O 1s spectral deconvolutions that account for condensed HCOOH. The O 1s component of condensed H$_2$O is used. [b]Calculated using the total O 1s condensed phase areas (i.e., O 1s fit using only one gas phase and one condensed phase component).

3.5. Discussion

In order to understand the connection between our surface tension and XPS data, we consider a simple model of XPS signal where we treat the interface as a function of depth into solution in two parts. The first is a surface layer located from $z = 0$ to a depth, w, into the solution, that contains the concentration per volume of formic acid as measured by surface excess, ρ_{se}, added to the bulk density, ρ_{bulk}. For the purpose of the model, the total surface excess per unit area, n_{se}, is spread evenly throughout the interfacial layer of width w, so $\rho_{se} = n_{se}/w$ and $\rho_{surface} = \rho_{se} + \rho_{bulk}$. The second part of the XPS signal comes from integrating over the bulk number concentration of formic acid, ρ_{bulk}. The bulk integration begins after the interface, starting at $z = w$ and extending to infinity. The simulated signal comes from an integration in

which the signal is attenuated by an exponential decay characteristic of electron attenuation, given by:

$$S = \int_0^w \rho_{surface} e^{-(z/IMFP)} dz + \int_w^\infty \rho_{bulk} e^{-(z/IMFP)} dz \tag{3.2}$$

$$= IMFP\rho_{surface}(1 - e^{-(w/IMFP)}) + IMFP\rho_{bulk} e^{-(w/IMFP)}$$

We calculate this signal for the carbon from formic acid, the oxygen from water, and for the total oxygen from both water and formic acid. For the 155 eV photoelectron kinetic energy used to probe C 1s, the best current estimate for the electron inelastic mean free path (IMFP) in dilute aqueous solution is 9 ± 2 Å, whereas at 362 eV (O 1s) the value is 15 ± 2 Å (Thurmer, Seidel et al. 2013, Jordan, Redondo et al. 2014). We found that the fits were best at the limits of these error bars, and used IMFP values of 7 Å for the 155 eV C 1s signal and 17 Å for the 362 eV O 1s signal. The signal for each element was simulated for several different solution compositions in line with those used in the experiments. We present the results for two limiting cases of interfacial width, w, 4 Å and 51 Å. The 51 Å depth was chosen to coincide with the maximum probe depth of the experiment for O 1s, assumed to be 3 times the IMFP. By contrast the 4 Å depth was chosen to represent a system in which the interfacial region is molecularly thin and is the smallest width for which the formic acid does not overfill the interface, forcing a density greater than that of neat formic acid. In Fig. 3.3 we plot an example of the number densities used in the (a) 4 Å and (b) 51 Å simulations for a representative concentration (formic acid activity = 0.117). These densities are overlaid with the exponential decay term arising from the 7 Å and 17Å IMFP values as a function of depth.
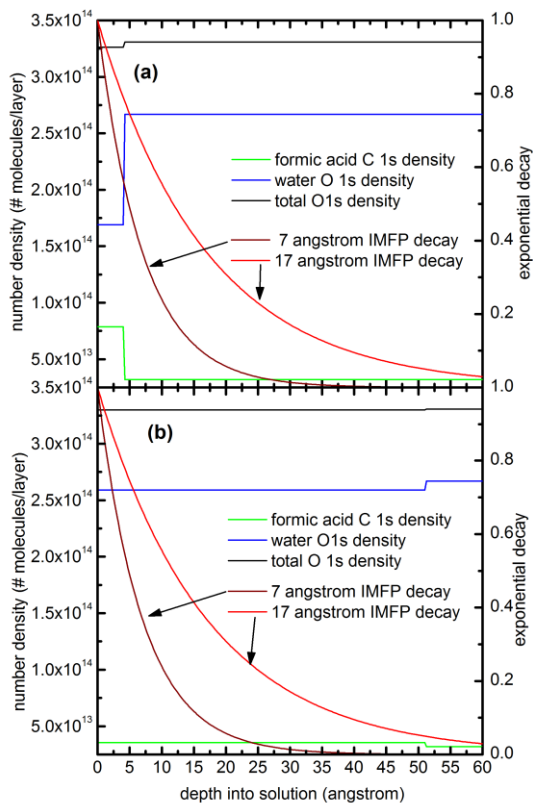
Fig. 3.3. A plot of the number density of C from C1s in formic acid (green), O from water (blue) and O total (black). Both the (a) 4 Å simulation and (b) 51 Å simulations are shown. The layer volume is 1 cm x 1 cm x 1 Å. Number densities are given for a single solution composition, chosen to be a formic acid activity of 0.117. The exponential decay term for IMFP values used for carbon (7 Å, shown in brown) and oxygen (17 Å, shown in red) are overlaid on the graph.

In Fig. 3.4, simulated XPS intensity ratios based on the integrated signal described above are compared to the experimental C 1s HCOOH$_{(liq)}$/O 1s$_{(liq)}$ and C 1s HCOOH$_{(liq)}$/O 1s H$_2$O$_{(liq)}$ values. The integrations assuming a 4 Å interface match the data well except at the very highest activity value. We cannot definitively explain the overestimation of the signal at the highest concentrations but we note that it coincides with the same concentration range in which Johnson et al (Johnson, Tyrode et al. 2009) noted a disruption of water structure by formic acid in aqueous formic acid solutions. In the study of Ottosson et al. (Ottosson, Wernersson et al. 2011) which uses a similar model to quantitatively connect XPS and surface tension, deviation was also found at high concentrations. Their work found the ratio of PE signal to a model incorporating surface excess to drop as a function of acetic acid concentration. They interpreted this to mean that the molecules were buried deeper into solution at high concentration. Assuming the interface is 51 Å wide, the predicted XPS signal intensities do not accurately reproduce the shape of the experimental results. Thus we find that the XPS data is well fit by a model that assumes that the surface tension results represent the outermost, molecularly thin, layer of the solution. If we assume that the surface tension is probing a region similar to that of the XPS probe volume, we do not get a consistent description of the interface by the two techniques. It is worth noting that for a stronger

surfactant than formic acid with a relative higher concentration at the interface, the XPS measurements would be expected to more closely match the surface tension results.
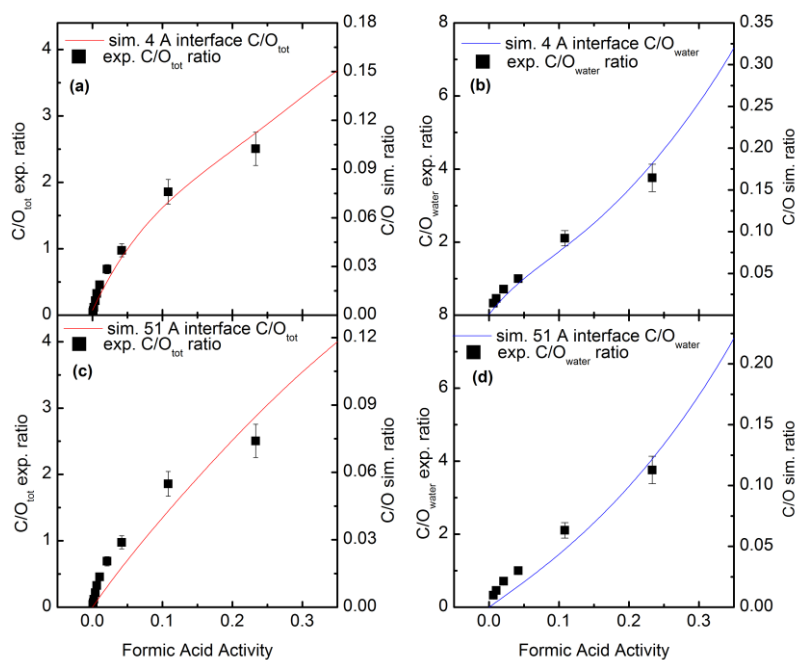

Fig. 3.4. A comparison of the C/O experimental ratio from XPS (squares) and the simulated surface signal from equation 3 (lines) as a function of formic acid activity for two different widths of the interface. Panels (a) and (c) show C/O_{tot} for interfacial widths of 4 Å and 51 Å, respectively while panels (b) and (d) give C/O_{water} for interfacial widths of 4 Å and 51 Å, respectively.

3.6. Conclusion

Surface tension and XPS measurements were applied to the same ternary system, solutions of formic acid, sodium chloride and water. The surface excess measured via surface tension was used to model the XPS results. These agreed under the assumption that the surface excess was located in an interfacial region that was much smaller, by up to a factor of 10, than the probe depth of the XPS measurements. However, XPS affords additional electronic structure information that surface tension cannot access.

Acknowledgments

References

Adamson, A. W. (1976). Physical Chemistry of Surfaces. New York, Wiley.

Ammann, M., R. A. Cox, J. N. Crowley, M. E. Jenkin, A. Mellouki, M. J. Rossi, J. Troe and T. J. Wallington (2013). "Evaluated kinetic and photochemical data for atmospheric chemistry: Volume VI - heterogeneous reactions with liquid substrates." Atmospheric Chemistry and Physics **13**(16): 8045-8228.

Brown, M. A., F. Vila, M. Sterrer, S. Thurmer, B. Winter, M. Ammann, J. J. Rehr and J. A. van Bokhoven (2012). "Electronic Structures of Formic Acid (HCOOH) and Formate (HCOO⁻) in Aqueous Solutions." Journal of Physical Chemistry Letters **3**(13): 1754-1759.

Buch, V., A. Milet, R. Vacha, P. Jungwirth and J. P. Devlin (2007). "Water Surface is Acidic." Proceedings of the National Academy of Sciences of the United States of America **104**(18): 7342-7347.

Chmielewska, A., A. Wypych-Stasiewicz and A. Bald (2007). "Viscosity of Aqueous Solutions of Monocarboxylic Acids." Journal of Molecular Liquids **130**(1-3): 42-47.

Donaldson, D. J. and C. George (2012). "Sea-Surface Chemistry and Its Impact on the Marine Boundary Layer." Environmental Science & Technology **46**(19): 10385-10389.

Eisenthal, K. B. (1993). "Liquid Interfaces." Accounts of Chemical Research **26**(12): 636-643.

Enami, S., M. R. Hoffmann and A. J. Colussi (2008). "Acidity Enhances the Formation of a Persistent Ozonide at Aqueous Ascorbate/Ozone Gas Interfaces." Proceedings of the National Academy of Sciences of the United States of America **105**(21): 7365-7369.

Imberti, S. and D. T. Bowron (2010). "Formic and Acetic Acid Aggregation in the Liquid State." Journal of Physics-Condensed Matter **22**(40).

Johnson, C. M., E. Tyrode, A. Kumpulainen and C. Leygraf (2009). "Vibrational Sum Frequency Spectroscopy Study of the Liquid/Vapor Interface of Formic Acid/Water Solutions." Journal of Physical Chemistry C **113**(30): 13209-13218.

Jordan, I., A. B. Redondo, M. A. Brown, D. Fodor, M. Staniuk, A. Kleibert, H. J. Wörner, J. B. Giorgi and J. A. van Bokhoven (2014). "Non-Uniform Spatial Distribution of Tin Oxide (SnO₂) Nanoparticles at the Air-Water Interface." Chemical Communications **50**(32): 4242-4244.

Jubb, A. M., W. Hua and H. C. Allen (2012). "Organization of Water and Atmospherically Relevant Ions and Solutes: Vibrational Sum Frequency Spectroscopy at the Vapor/Liquid and Liquid/Solid Interfaces." Accounts of Chemical Research **45**(1): 110-119.

Jungwirth, P. and D. J. Tobias (2006). "Specific Ion Effects at the Air/Water Interface." Chemical Reviews **106**(4): 1259-1281.

Khare, P., N. Kumar, K. M. Kumari and S. S. Srivastava (1999). "Atmospheric Formic and Acetic Acids: An Overview." Reviews of Geophysics **37**(2): 227-248.

Kolbeck, C., J. Lehmann, K. R. J. Lovelock, T. Cremer, N. Paape, P. Wasserscheid, A. P. Fröba, F. Maier and H. P. Steinrück (2010). "Density and Surface Tension of Ionic Liquids." Journal of Physical Chemistry B **114**(51): 17025-17036.

Krisch, M. J., R. D'Auria, M. A. Brown, D. J. Tobias, J. C. Hemminger, M. Ammann, D. E. Starr and H. Bluhm (2007). "The effect of an organic surfactant on the liquid-vapor interface of an electrolyte solution." Journal of Physical Chemistry C **111**(36): 13497-13509.

Lewis, T., B. Winter, A. C. Stern, M. D. Baer, C. J. Mundy, D. J. Tobias and J. C. Hemminger (2011). "Does Nitric Acid Dissociate at the Aqueous Solution Surface?" Journal of Physical Chemistry C **115**(43): 21183-21190.

Li, Z. D., A. L. Williams and M. J. Rood (1998). "Influence of Soluble Surfactant Properties on the Activation of Aerosol Particles Containing Inorganic Solute." Journal of the Atmospheric Sciences **55**(10): 1859-1866.

Nathanson, G. M. (2004). "Molecular Beam Studies of Gas-Liquid Interfaces." Annual Review of Physical Chemistry **55**: 231-255.

Ottosson, N., E. Wernersson, J. Söderström, W. Pokapanich, S. Kaufmann, S. Svensson, I. Persson, G. Öhrwall and O. Björneholm (2011). "The Protonation State of Small Carboxylic Acids at the Water Surface from Photoelectron Spectroscopy." Physical Chemistry Chemical Physics **13**(26): 12261-12267.

Padday, J. F. and D. R. Russell (1960). "The Measurement of the Surface Tension of Pure Liquids and Solutions." Journal of Colloid Science **15**: 503-511.

Pajak, Z. and E. Szcześniak (1977). "Structure and Microdynamic Behavior of Liquid Formic-Acid." Chemical Physics Letters **49**(2): 269-272.

Petersen, M. K., S. S. Iyengar, T. J. F. Day and G. A. Voth (2004). "The Hydrated Proton at the Water Liquid/Vapor Interface." Journal of Physical Chemistry B **108**(39): 14804-14806.

Petersen, P. B. and R. J. Saykally (2006). "On the Nature of Ions at the Liquid Water Surface." Annual Review of Physical Chemistry **57**: 333-364.

Petersen, P. B. and R. J. Saykally (2006). "Probing the Interfacial Structure of Aqueous Electrolytes with Femtosecond Second Harmonic Generation Spectroscopy." Journal of Physical Chemistry B **110**(29): 14060-14073.

Schwier, A. N., G. A. Viglione, Z. Li and V. F. McNeill (2013). "Modeling the Surface Tension of Complex, Reactive Organic-Inorganic Mixtures." Atmospheric Chemistry and Physics **13**(21): 10721-10732.

Singleton, D. L., G. Paraskevopoulos and R. S. Irwin (1987). "UV Absorption Cross-Sections of the Monomer and Dimer of Formic-Acid." Journal of Photochemistry **37**(2): 209-216.

Sorjamaa, R., B. Svenningsson, T. Raatikainen, S. Henning, M. Bilde and A. Laaksonen (2004). "The Role of Surfactants in Köhler Theory Reconsidered." Atmospheric Chemistry and Physics **4**: 2107-2117.

Soucková, M., J. Klomfar and J. Pátek (2008). "Measurement and Correlation of the Surface Tension-Temperature Relation for Methanol." Journal of Chemical and Engineering Data **53**(9): 2233-2236.

Thurmer, S., R. Seidel, M. Faubel, W. Eberhardt, J. C. Hemminger, S. E. Bradforth and B. Winter (2013). "Photoelectron Angular Distributions from Liquid Water: Effects of Electron Scattering." Physical Review Letters **111**(17).

Tuckermann, R. (2007). "Surface tension of aqueous solutions of water-soluble organic and inorganic compounds." Atmospheric Environment **41**(29): 6265-6275.

Winter, B. and M. Faubel (2006). "Photoemission from liquid aqueous solutions." Chemical Reviews **106**(4): 1176-1211.

Chapter 4

4. Quantifying the Affinity of C1-C4 Oxygenated Volatile Organic Compounds for the Air−Water Interface using Liquid jet XPS

Ming-Tao Lee, D. James Donaldson, Markus Ammann, Matthew A. Brown

Manuscript in preparation

4.1. Abstract

The liquid−vapor interface is difficult to interrogate experimentally but is of interest from a theoretical and applied point of view, and has particular importance in atmospheric aerosol chemistry. Here, we examine the liquid−vapor interface for mixtures of water and small alcohols or small carboxylic acids (C1-C4), abundant chemicals in the atmosphere. We compare the results of X-ray photoelectron spectroscopy (XPS) measurements over all species at 0.5 M bulk concentration with the surface excesses derived from literature values for the surface tensions of surface tension measurements. A linear correlation was found between the headgroup carbon 1s core-level signal intensity and the surface excess, with the offset being explained by the bulk contribution to the photoemission signal. The correlation between XPS and macroscopic equilibrium thermodynamic quantity is an indication of the equilibrated condition of the vacuum liquid jet surface with respect to the bulk–surface equilibrium of short-chained surfactants. The surface propensity of the carboxylic acids was found to be about a factor of five higher than that of their conjugate carboxylate bases, with a trend to increase with chain-length. The ratio of aliphatic to headgroup C 1s signal intensities indicated an increasing orientation towards the surface normal as a function of chain length, along with increasing importance of lateral hydrophobic interactions. The hydrophobicity as a driving force for adsorption to the interface leads to a remarkable linear correlation between the C 1s signal intensity and the octanol-water partition coefficient P.

4.2. Introduction

A better understanding of the molecular properties of organic compounds at the liquid-vapor interface and of the impact of their presence on the properties of this interface is important in many fields of science, in particular in atmospheric chemistry. Small oxygenated volatile organic compounds (OVOC), such as alcohols and acids, are important products of atmospheric oxidation cycles. Their amphiphilic nature due the presence of hydrophilic and hydrophobic functional groups is controlling their propensity for the aqueous liquid−vapor interface. Organic surfactants may affect cloud condensation nucleus activation (Prisle, Asmi et al. 2012) and the phase transfer of major and trace species (McNeill, Patterson et al. 2006, Rouviere and Ammann 2010), or accelerate reactions at the aqueous liquid−vapor interface of aerosol particles (Donaldson and Valsaraj 2010). The macroscopic surface tension is directly

related via the Gibbs equation to the surface excess, Γ_i, of a component i beyond a theoretical dividing plane (referred to as the Gibbs surface) placed parallel to the solution surface. The surface excess expresses the increased or decreased number of solute molecules within the volume above the Gibbs surface relative to those in the bulk of the solution. While comparatively easy to measure, surface tension falls short of providing selectivity for chemical properties or the detailed depth profile of components at the interface contributing to it. In turn, X-ray photoelectron spectroscopy (XPS) likely provides the most chemically selective information from the interfacial region (Hüfner 1995). XPS is surface-specific due to the short inelastic mean free path (IMFP or λ) of photoelectrons in condensed matter. The photoelectrons can only escape without loss of energy (inelastic scattering) from a few nm, which is still a significant depth on molecular length scales, though. XPS quantitatively measures the amount of molecules within the probe depth (defined as $3 \times \lambda$), since the intensity of core-level photoelectron (PE) signals is proportional to atom density after all normalizations. On top of that, XPS is sensitive to the chemical environment and oxidation state, i.e., for soluble organic compounds, it distinguishes between carbons in hydroxyl (-C-OH), carboxyl (-C-OOH), carboxylate (-C-OO$^-$), and aliphatic (-CH$_2$)$_n$ functional groups. The development of liquid jets gives the opportunity of probing a continuously renewed surface free of contamination or beam damage that would significantly affect XPS experiments with static liquids (Brown, Faubel et al. 2009). XPS and surface tension thus provide complementary information about the liquid−vapor interface and have been coupled for this reason in previous work (Krisch, D'Auria et al. 2007, Ottosson, Wernersson et al. 2011). There is one study (please also see *chapter 3*) quantitatively comparing results of the two methods over a range of formic acid solutions (Pruyne, Lee et al. 2014).

In this chapter, we report C 1s core-level photoelectron spectra of C1 to C4 monoacids (formic, acetic, propionic, and butyric acid), their respective (sodium) carboxylate conjugate base forms (formate, acetate, propionate, and butyrate), and C1 to C4 alcohols (methanol, ethanol, 1-propanol, 2-propanol, and 1-butanol) in aqueous solution, all at a bulk concentration of 0.5 M. The surface propensity information derived from XPS for the acids, the carboxylate ions and the alcohols will be compared with that from surface tension data reported in the literature. In addition, the XPS signal may explain the origin of the largely different surface tensions of neutral carboxyls versus the deprotonated carboxylate ions. Furthermore, XPS provides information about the orientation of surface molecules for different functional groups and chain lengths, which is driven by lateral hydrophobic

interactions. The latter is then the origin of a strong correlation of photoemission signals with the octanol-water partition coefficient.

4.3. Experimental section

X-ray photoelectron spectroscopy (XPS). XPS experiments using a liquid micro-jet (Brown, Faubel et al. 2009) were performed at the Surfaces/Interfaces: Microscopy (SIM) beamline (Flechsig, Nolting et al. 2010) of the Swiss Light Source (SLS) using a near ambient pressure photoemission (NAPP) endstation (Brown, Redondo et al. 2013). A 19 μm liquid jet operating at 279 K (measured immediately before entry into the ionization chamber) with a flow rate of 0.30 ml/min at a chamber pressure of $< 1.0 \times 10^{-4}$ mbar was used. The equilibrated nature of the liquid jet under these conditions has been discussed previously (Faubel, Steiner et al. 1997, Pruyne, Lee et al. 2014, Lee, Brown et al. 2015). The entrance orifice of the hemispherical energy analyzer and the working distance to the liquid jet were both 500 μm. The Scienta HiPP-2 analyzer was operated at 100 eV pass energy in 0.1 eV step size.

All aqueous solutions (methanol and ethanol, ACS reagent, ≥99.8%, Sigma-Aldrich; 1 and 2-propanol, ACS reagent, ≥99.5%, Sigma-Aldrich; 1-bunanol, 99.9%, Sigma-Aldrich; formic acid, ACS reagent, ≥98%, Sigma-Aldrich; acetic acid, ACS reagent, ≥99.7%, Sigma-Aldrich; propionic acid, ACS reagent, ≥99.5%, Alfa Aesar; butyric acid, ≥99+%, Alfa Aesar) were prepared using Milli-Q water (Millipore, 18.2 MΩ cm at 25 °C) at 0.5 M in 0.05 M NaCl (Sigma-Aldrich, ACS reagent, ≥99%). The sodium chloride is used to ensure adequate conductivity of the solutions to prevent charging of the liquid micro-jet in the X-ray beam in absence of other ionic solutes. Bulk pH values were measured using a Mettler Toledo Expert Pro electrode that was calibrated using a four point curve at room temperature.

We use a combination of first- and second-order synchrotron light (Pruyne, Lee et al. 2014, Lee, Brown et al. 2015, Redondo, Jordan et al. 2015). The primary photon beam was set to 450 eV to ionize the C 1s orbital of aqueous organic solutions with a kinetic energy of ca. 155 eV (Pruyne, Lee et al. 2014). Second order light, 900 eV, that passes through the beamline optics with ca. 10 % intensity of the primary energy was used to ionize the O 1s orbital (binding energy of O 1s in liquid water is 538.1 eV(Brown, Winter et al. 2009)) with kinetic energy of about 362 eV. The C 1s and O 1s regions were collected in parallel by setting the hemispherical energy analyzer to take a single pass of the C 1s region followed by

a single pass of the O 1s. 15 sweeps were averaged to create one spectrum. Because the C 1s and O 1s orbitals are collected from different electron kinetic energies (KE's) and therefore different depths into solution, we report only a relative surface concentration of the organic. That is, a C 1s / O 1s ratio of the integrated peak areas that assumes the O 1s signal is dominated by H_2O independent of organic content. This ratio provides an indication of the overlap between the X-ray beam and the liquid, and thus takes into account the small spatial fluctuations of the liquid jet. These C 1s / O 1s ratios will be referred to as the measured (functional group) C 1s intensity in the following sections.

4.4. Results and discussion

O 1s and C 1s photoelectron spectra. An example of O 1s spectrum that is representative of all investigated solutions is shown in Fig. S4.1. There are two peaks in the O 1s region, assigned to gas phase water at lower KE and condensed liquid water at higher KE (Winter, Weber et al. 2004). Within the O 1s liquid peak two components should be present: solvent water at ~55 M and the organic solute at 0.5 M. We are, however, unable to resolve the individual contributions and fit the liquid region with a single component. This simplified approach bears no consequence on the conclusions of this study as our interpretations regarding the surface propensity for the organic solutes for the liquid−vapor interface are derived from the C 1s spectra.

The noticeable contribution from gas phase water in the O 1s spectrum of Fig. S4.1 (ca. 25% at 360 eV KE) results from the non-ideal overlap of the X-ray beam (FWHM = 100 μm) (G. Olivieri 2015) and the 19 μm liquid jet. The X-rays that do not overlap perfectly with the liquid jet ionize the gas phase water (and organic) envelope that surrounds the liquid jet as it propagates through the measurement chamber. Unfortunately, this can, for certain samples—like the alcohols, lead to difficulty in deconvoluting the C 1s spectra (we fit the O 1s gas phase contribution with a single component—in line with the liquid peak). We explain later why this is important only for the alcoholic solutions. In the C 1s spectra, up to four peaks are present, two from the condensed phase (functional head group carbon and the backbone aliphatic chain) and two from gas phase (Fig. 4.1a). To enable a more accurate fit of the C 1s region for the alcoholic solutions we performed additional experiments with the liquid jet setup of the synchrotron radiation facility BESSY (Winter and Faubel 2006) (Fig. S4.2 and Table S4.1). The advantage of the BESSY setup over that of the SLS is that the FWHM of

the X-ray beam is the same size of the liquid jet, effectively suppressing the gas phase contribution of the alcohols in the C 1s spectra (compare Fig. 4.1a with Fig. S4.2). We have used the C 1s spectra for ethanol, 1- and 2-propanol, and 1-butanol from BESSY to establish the BE spacing between the two condensed phase components. In our analysis of the spectra collected from the SLS at 0.5 M we have used these peak separations as constraints in the fitting routine. The spectra from BESSY are not used in our discussion of solute affinity for the air−water interface (AWI) because they were collected at different concentrations, different photon energy (probe depth of the XPS experiment is a function of photon energy for a given orbital) and furthermore, we report here a relative (vide infra) concentration of organic at the interface relative to that of the most intense signal—from 1-butanol). The same BE spacing is also enforced for the two gas phase components of the C 1s spectra.

The C 1s photoelectron spectra from (**a**) the alcohols, (**b**) the carboxylic acids and (**c**) the carboxylates are shown in Fig. 4.1. The pH of our measurements ensures that the acid-base equilibrium is shifted predominantly towards the carboxylic acids (W. M. Haynes Internet Version 2016) in Fig. 4.1b (97% for formic acid and >99% for the others) and entirely to that of the carboxylates (100%) in Fig. 4.1c (pH-values are listed in Table 4.1). The carbon atom of the head group (fit shown in blue) is well resolved from the carbon backbone (red), with the former having a lower KE (higher BE) that reflects its more oxidized state. Further confirmation of this assignment comes by noting the peak position for the solutes that contain only the head group carbon, methanol (lower panel of Fig. 4.1a), formic acid (lower panel of Fig. 4.1b) and formate (lower panel of Fig. 4.1c). The C 1s BE's for all the solutes are tabulated in the Supporting Information (Table S4.1).
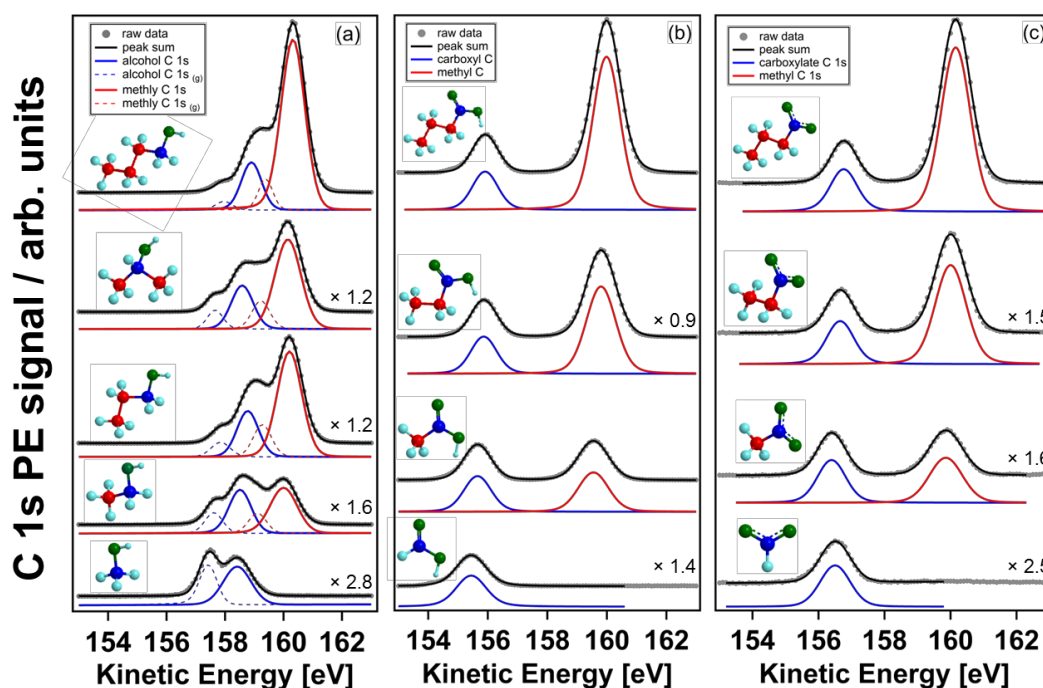
Fig. 4.1. Carbon 1s photoemission spectra of 0.5 M aqueous solutions of organics taken at a photoelectron kinetic energy around 155 eV for (a) alcohols, (b) carboxylic acids, and (c) ionic (sodium)carboxylates. All the spectra are normalized to the peak area of the functional carbon (C4) within the same functional group family.

Qualitatively, the ratios of the gas phase contributions to that of $H_2O_{(gas)}$ can be compared. The gas-phase contribution for the acids is much smaller than for the alcohols in general. This is consistent with the vapor pressure derived from the Henry's law constants for 0.5 M acidic solutions ($0.11\text{-}8.44\times10^{-2}$ mbar) being smaller than for 0.5 M alcoholic solutions (2.3-4.61 mbar) (R. Sander 2015). Within the series of alcohols themselves, the vapor pressure increases with increasing chain length leading to a slight increase of the relative contribution of the gas phase peaks in each spectrum.

We measure a marked difference in normalized C1s signal intensity from the head group carbon atom between organics at the AWI (Table 4.1). Because the XPS experiment is done at a fixed KE (probe depth of ca. 1 nm) for all solutions these changes in intensity between the different organic solutes are easiest to interpret as arising from substantially different propensities for the AWI. That is, the different organic solutes exhibit substantially different spatial (physical) distributions at and near the AWI.

Table 4.1. Relative intensity of the functional group carbon 1s photoemission signal

Organic Solute	pH	C 1s intensity*
Formate, $HCOO^-$	12.8	0.07
Acetate, $CH_3\text{-}COO^-$	12.9	0.1
Propionate, $CH_3CH_2\text{-}COO^-$	12.8	0.12
Butyrate, $CH_3CH_2CH_2\text{-}COO^-$	12.6	0.19
Methanol, $CH_3\text{-}OH$	-	0.22
Formic acid, $HCOOH$	2.2	0.34
Ethanol, $CH_3CH_2\text{-}OH$	-	0.46
Acetic acid, $CH_3\text{-}COOH$	2.6	0.55
2-Propanol, $CH_3CH\text{-}OH\text{-}CH_3$	-	0.71
Propionic Acid, $CH_3CH_2\text{-}COOH$	2.7	0.72
1-Propanol, $CH_3CH_2CH_2\text{-}OH$	-	0.74
Butyric Acid, $CH_3CH_2CH_2\ COOH$	2.7	0.86
1-Butanol, $CH_3CH_2CH_2CH_2\text{-}OH$	-	1

*all value are normalized to the functional carbon 1s of 1-butanol

We derive the surface excesses from literature values for the surface tensions of the alcohols (Hoke and Chen 1991, Vazquez, Alvarez et al. 1995, Aratono, Toyomasu et al. 1997, Glinski, Chavepeyer et al. 1998, Donaldson and Anderson 1999, Belda Maximino 2009), carboxylic acids (Wright and Akhtar 1970, Donaldson and Anderson 1999, Granados, Gracia-Fadrique et al. 2006) and carboxylates (Abramzon and Gaukhberg 1993, Minofar, Jungwirth et al. 2007) (Fig. S4.3). The recorded C 1s intensities of the head group carbon atoms reported in Table 1 scale linearly with the mean surface excesses, Γ_{se} (Fig. 4.2, error bars in the x-axis represent the standard deviation of the Γ_{se}). The impressive agreement of the XPS intensities with results derived from a measurement accepted to be in thermodynamic equilibrium (Adamson 1997), surface tension (surface excess), provides further support to the growing consensus (Brown, Lee et al. 2015) that the liquid jet provides a measurement tool in vacuum for XPS that is representative of a static solution interface in ambient humidity because it is in local equilibrium (Faubel, Schlemmer et al. 1988, Winter and Faubel 2006).
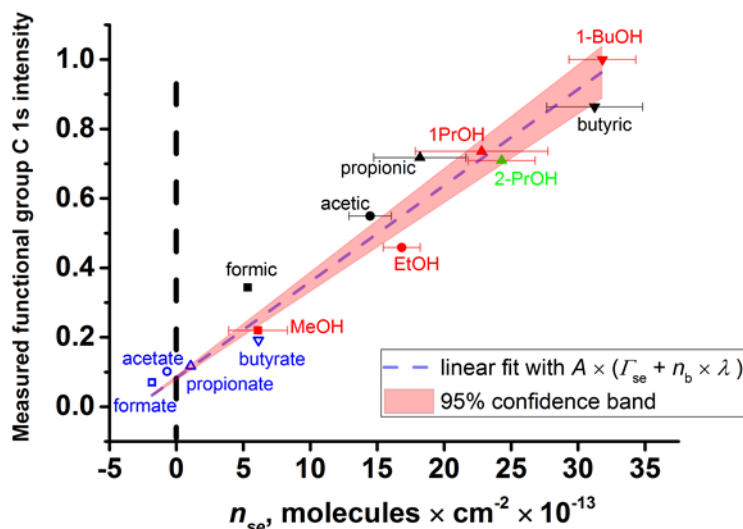
Fig. 4.2. Comparison of measured functional group C 1s intensity of organics and the corresponding surface excess values as a function of organic species. The dashed line indicates an ideal behavior with a perfectly uniform distribution across the entire solution.

To first approximation, the measured functional group C 1s intensities (I_C) are contributed by both the molecules residing in the bulk within the probe depth and those directly sitting on the surface represented by the surface excess (Γ_{se}), as already pointed out in *Chapter 3*:

$$I_C = A \, (\Gamma_{se} + \lambda \times n_b) \tag{E 4.1}$$

A is a proportionality factor; n_b is the bulk concentration i.e. 0.5 M. For $\lambda \approx 1$ nm, the last term on the right hand side in equation (E 4.1) contributes about 3×10^{13} molecule per cm^2, which is significant especially for the less surface active C 1 species and the deprotonated carboxylate ions. This simple model assumes that those molecules making up for the surface excess are contributing to the C 1s signal without attenuation, while the second term on the right hand side is the result of the integral of the contribution of bulk phase organic species exponentially decreasing with depth. In Fig. 4.2, the simulated C 1s intensity based on equation (E 4.1) is fit to the experimental values. It matches the data well and even does so for negative surface excess for formate and acetate ions. Note that this is a one parameter fit, i.e., the ratio between the offset at zero surface excess and the slope of the line is constant. The fact that it fits well, provides evidence that the estimate for the electron inelastic mean free path taken for this system is a good approximation.

As apparent from Fig. 4.2, the different species group according to the type of functional group and within the same functional group family, the surface propensity increases with

increasing chain length. We start with a more detailed discussion of the data for the carboxylic acids and their conjugate bases. Photoelectron spectroscopy has been used to study the liquid−vapor interface of carboxylic acids water solutions previously (Ottosson, Wernersson et al. 2011, Brown, Vila et al. 2012, Pruyne, Lee et al. 2014). All the carboxylic acids were found with higher affinity for the surface relative to their conjugate base carboxylates. This is because the dissociation reactions of carboxylic acids into carboxylates, exhibit greater hydration free energies of the charged carboxylate group compared to the neutral acids (Florian and Warshel 1997, Setny 2015). The lower surface propensity of the deprotonated carboxylate ions is also in line with the simple electrostatic picture that ions are repelled from the interface. The substantially larger measured functional group C 1s intensity for the acids than for their conjugated bases (carboxylates) are in line with previous studies mentioned above.
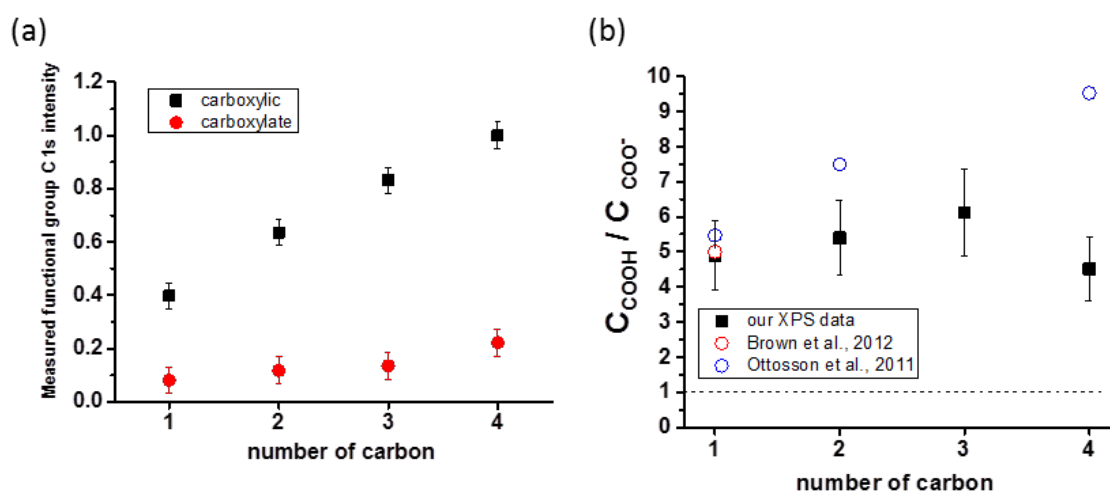

Fig. 4.3. (a) Measured functional group C 1s intensity for acids and their corresponding carboxylates against number of carbon. (b) Ratio of functional group C 1s signal intensity of acids to that of their corresponding conjugated bases against number of carbon. The ratios are compared with other studies on similar systems (Brown, Vila et al. 2012, Ottosson, Wernersson et al. 2011).

Fig. 4.3a shows the same data as in the Fig. 4.2 but now plotted as the measured C 1s PE signals of the 0.5 M formic, acetic, propionic, and butyric acids at low pH and the signals of the corresponding carboxylate solutions at high pH (see Table 4.1), using the carbon chain length to categorize the data. The chain length is also a measure of the ratio of hydrophobic to hydrophilic interaction options. The measured functional group C 1s intensity increases with increasing aliphatic chain length for both neutral carboxyl and charged carboxylate. The formate ion is the only species exhibiting a positive surface tension difference to pure water

at 0.5 M, indicative of the extent of electrostatic repulsion from the interface induced by this headgroup. For the other carboxylates, the increasing hydrophobic carbon chain seems to lead to a net positive attraction towards the interface, counteracting charge repulsion. Fig. 4.3b represents the ratios of the C 1s signals of each pair of carboxylic acid and its conjugated base. They seem to increase with chain length from formic/formate to propionic/propionate, while when considering the uncertainty (error bar in Fig. 4.3b) in the measurements, this increase is likely not significant. A constant ratio would indicate that the electrostatic repulsion has always the same effect independent of the chain length, while the slight increase could indicate that the longer hydrophobic aliphatic carbon chain has a relatively stronger effect on the neutral acids than on the carboxylates. In the latter case, the hydrophobic interactions would progressively dictate the preference for the interface of the longer chain carboxylic acids. The ratio of butyric/butyrate is lower probably because the surface excess of butyric acid exhibits saturation at 0.5 M (Fig. S4.5), so that the surface concentration is also affected by lateral interactions and not only affected by the amphiphilic nature and charge repulsion. This limit has likely not been reached for butyrate at 0.5 M. The ratio for formic/formate reported here is consistent with data from both Ottosson et al. (Ottosson, Wernersson et al. 2011) (measured at pH at corresponding pK_a) and Brown et al (Brown, Vila et al. 2012) (measured at pH = pK_a), while the ratios derived from data from Ottosson et al. are slightly higher for acetic and significantly higher for butyric acids. The first difference is that they have measured the carboxylic/carboxylate PE ratio for a total bulk concentration of 1 M at pH ≈ pK_a. Their assumption was that the neutral carboxylic and charged carboxylate are coexisting in the bulk at equal concentrations of about 0.5 M in the same solution. In this context, it may be expected that the competition among the two at the interface due to lateral interactions leads to a preference of the neutral acid at the expense of the carboxylate ion and thus to a higher ratio of the two in their experiment. In contrast, the ratios reported here were based on measurements at low and high pH for the same bulk concentration of 0.5 M for both individually, so that lateral interactions were not playing a role for C1 to C3 species, and also not for butyrate. Since the surface propensity also of neutral formic acid is not very high (so that formate does not feel the presence of formic acid at the interface), the data for formic acid and formate are consistent among the studies. We also note that Ottosson et al. used a different photoelectron KE = 70 eV for C 1s in their study, and KE = 150 eV in this study. This leads to a lower proportion of the bulk contribution to the C 1s signal, adding to an increase of the ratio considered here.

The carboxylic acids may act as Brønsted acids (proton donors) in aqueous solution, and their conjugate bases may act as Brønsted bases (proton acceptors), whereas the sodium ions have practically no acid/base properties in this respect. The acid-base equilibrium and dissociation and protonation kinetics in the bulk aqueous phase are well known in the aqueous phase. However, whether the asymmetric hydrogen bonding environment at the AWI changes is not well established. Whether the enhanced presence of the neutral acid is just a consequence of the latter or the availability of protons at the interface is higher, remains also open. The debate is ongoing whether protons themselves prefer the interface or not (Petersen and Saykally 2008, Tian, Ji et al. 2008, Gray-Weale and Beattie 2009, Winter, Faubel et al. 2009), or whether a very fine structure exists in the interfacial region of the proton profile with depth. (Saykally 2013) Mass spectrometry results from nanodrops emerging from microdroplets in the ionization environment of an electro-spray led Mishra et al. (Mishra, Enami et al. 2012) to suggest that the AWI (on the air side) is Brønsted neutral for bulk pH values around 3. The same technique applied by the same group also indicated enhanced reaction rates at the surface of aqueous droplets for acid catalyzed reactions (Dalleska, Colussi et al. 2000, Enami, Hoffmann et al. 2008).

The next point of discussion relates to the information obtained about the molecules themselves, which is accessible by XPS only. In principle, the C 1s core level excitation cross section is independent of the chemical environment carbon is engaged in, even though oscillations of the cross section due to scattering of the outgoing photoelectron wave at nearby atoms have been reported based on gas phase spectra (Soderstrom, Martensson et al. 2012), which is likely relevant only for heavy substituents, such as halogen atoms attached to the carbon chain. Thus, we could safely expect that the C 1s photoemission intensity is reflecting the molecular structure, i.e., the ratio of the C 1s peak areas assigned to aliphatic carbon to that assigned to the functional group carbon should increase from one to three for the C2 to C4 species, respectively. As shown in Fig. 4.4, where the aliphatic to functional group C 1s signal intensity ratio has been normalized to its stoichiometric value and plotted against the surface excess, this ratio exceeds stoichiometry for all species.
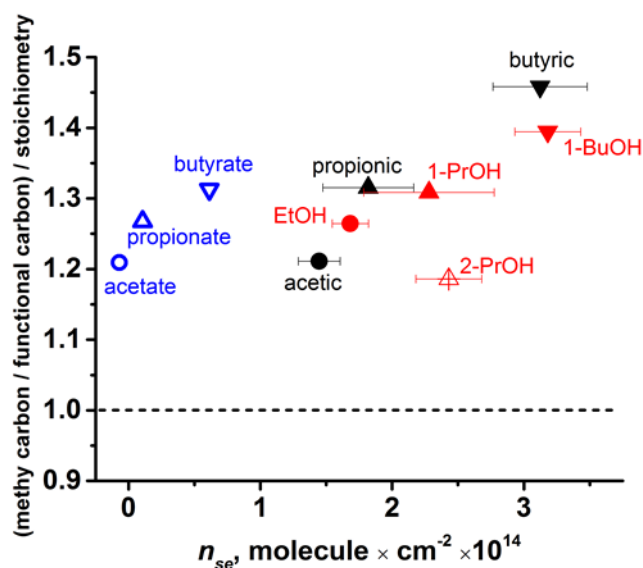
Fig. 4.4. Relative enhancement of integrated -C-CH$_2$ PE intensity to -C-functional-group PE intensity ratio as function of functional group, alkyl chain length, and surface excess.

Overall, this enhanced ratio is in line with the intuitive expectation that the preferred orientation of the amphiphilic molecules is that the functional group carbons prefer the interfacial region, while the aliphatic chain points rather outward away from it into vacuum. Thus, aliphatic C 1s photoelectrons are less attenuated than functional group carbon C 1s photoelectrons. This effect increases with increasing chain length for each functional family. This is notable especially for the carboxylates, which have very low surface excess. Thus, in spite of the fact that most of the carboxylate ions contributing to the C 1s signal intensity reside in the bulk away from the interface, the observed signal asymmetry may indicate that carboxylate ions in the bulk somewhat away from the interface still exhibit a preferred orientation towards the interface. For neutral acetic acid, the ratio is the same as for the acetate ion. The ratios for propionic and butyric acids strongly exceed those for their conjugated bases, partially attributed to a larger surface excess and thus stronger relative contribution of the surface molecules to the signal, but also indicating a stronger orientational effect and larger displacement of aliphatic carbon atoms away from the interface. If we would attribute the increase of this ratio within one functional group family entirely to the increased attenuation of headgroup C 1s photoelectrons, this would mean that we would have even underestimated the relatively higher preference of the neutral acids versus their conjugated bases based on Fig. 4.3. Turning the discussion towards the alcohol series, again, for those with the alcohol in the headgroup, the ratio increases as for the acids, albeit less strongly. For propanol, we also report a measurement for 2-propanol, where the OH group is on the center

carbon of this C3 alcohol. As expected, for 2-propanol, the aliphatic carbons being bound on both sides of the functional group, the ratio is lower than for 1-propanol, which offers more flexibility to orient the two aliphatic carbons away from the interface. It is presently not clear why the ratio for 2-propanol is lower than that for ethanol.
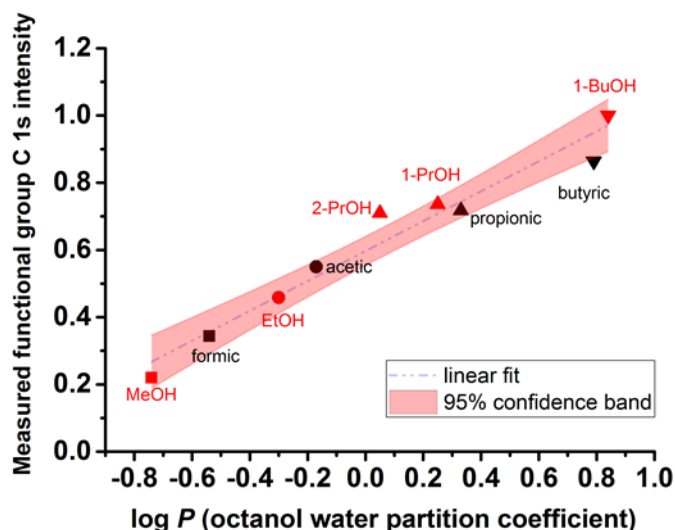

Fig. 4.5. Measured functional group C 1s intensity versus octanol-water partition coefficient (Sangster 1989).

As obvious from the previous discussion, XPS C 1s intensities measured for a range of surface active species can be directly used to discuss the surface propensity of each species, to gain information about their average orientation and to obtain insight into the relatively enhanced preference of carboxylic acids for the interface versus their carboxylate ions. Much of the discussion is triggered by the hydrophobic interaction of the aliphatic carbon chain in each molecule with liquid water. To summarize this discussion, we correlate, in Fig. 4.5, the C 1s PE signal for the series of C1 to C4 alcohols and acids studied here to the octanol-water partition constants (at 25°C for all P), a traditionally accepted hydrophobicity indicator (Valsaraj 1988). Hydrophobic compounds have generally low aqueous solubility. The most satisfactory explanation for the low aqueous solubility of a non-polar solute is the so-called "solvophobic theory". It especially considers the large decrease in entropy upon dissolution in water, attributed to the increased ordering of water molecules around the solute. The correlative decrease in entropy more than compensates for the modest increase in enthalpy of mixing. The solute molecules would have to replace the stronger hydrogen bonds among water molecules with the weaker solute-water intermolecular interactions. Those molecules that lose the competition for the hydrogen bonds are "squeezed out" of the interstices of the water structure. Since also many hydrophobic compounds considered have fairly low vapor

pressures due to substantial Van der Waals interactions the AWI is therefore a preferred place for them to go (Eley 1939, Eley 1944, Frank and Evans 1945, Valsaraj 1988).

The octanol-water partition coefficient (P or, in its more common expression, log P), which is defined as the ratio of the equilibrium concentration of the substance in the octanol-rich phase to that in the water-rich phase, is a widely used thermodynamic measure of the degree of hydrophobicity (adsorption/partitioning) of organic substances to the AWI. It is most commonly used to provide a means of the lipophilic vs. hydrophilic characteristics of an organic substance in biological systems (McKarns, Hansch et al. 1997, Vaes, Ramos et al. 1997, Escher, Schwarzenbach et al. 2000, Garrido, Queimada et al. 2009) or for partitioning of toxic organic compounds in environmental compartments (Tollefsen, Ingebrigtsen et al. 1998, Goss and Schwarzenbach 2001, Cropp, Kerr et al. 2011).

Therefore, even for hydrophobic molecules we would expect a propensity for the AWI. The polar headgroup of the amphiphilic molecules considered here of course enhance the driving force by the hydrophobicity alone. Future experiments may address the difference between the correlations obtained here with that of hydrophobic molecules.

4.5. Conclusion

Here we compared the surface propensity over a range of short-chained alcohols and carboxylic acids (C1-C4) by employing liquid microjet XPS. The results are correlated linearly with thermodynamic surface excess derived from classic surface tension measurements in literature. This strengthens the confidence that the approach of photoemission on a liquid micro-jet is a robust method to study surface propensity of organic compounds at the AWI. The approach of liquid microjet XPS can compare quantitatively the surface propensity of neutral species e.g. carboxylic acids with charged species e.g. carboxylate bases at the AWI. It can further provide us information on the tendency of the orientation of the absorbed molecules by considering the ratio of the aliphatic to functional group C 1s signal intensities affected by the aliphatic chain length at the interface. This would be an indicator for the orientational preference at the interface, in part dictated by lateral hydrophobic interactions. Interestingly, the C 1s PE signal intensity was found to linearly correlate with the octanol-water partition coefficient, P, a hydrophobicity indicator.

Supporting information

The O 1s XP regions from a liquid microjet of 0.5 M of formic acid solutions are shown in Fig. S4.1. The O 1s region is fitted by two components that are assigned to gas phase oxygen (mainly $H_2O_{(gas)}$) at higher BE and condensed phase oxygen ($H_2O_{(liq)}$ and $RCH_xO_{y(aq)}$) at lower BE. Because the O 1s levels attributed to oxygen in condensed phase alcohol- and carboxyl groups strongly overlap with that of $H_2O_{(liq)}$, we refrain from fitting detailed components to the condensed phase O 1s peak.
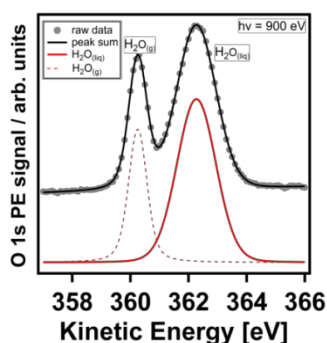

Fig. S4.1. O 1s photoelectron spectra recorded from 0.5 M aqueous solutions of formic acid is determined using X-ray photoelectron spectroscopy. O 1s region shows two components that are assigned as O $1s_{(gas)}$ and O $1s_{(liq)}$ from a 0.5 M formic acid aqueous solution.
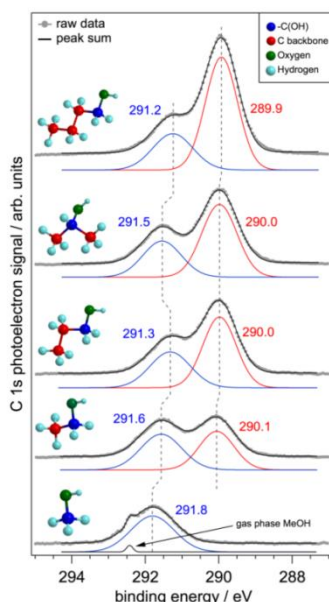

Fig. S4.2. C 1s photoelectron spectra recorded from 1.0 M aqueous solutions of methanol (CH_3-OH), ethanol (C_2H_5-OH), 1-propanol (C_3H_7-OH), 2-propanol (C_3H_7-OH), and 1-butanol (C_4H_9-OH). The raw data are shown in grey, the individual fit components in blue and red, and the sum of the fit components in black. BE's are referenced to the $1b_1$ of liquid water at 11.16 eV.

Table S4.1. Summary of the carbon 1s binding energies (BE) and full widths at half maximum (FWHM) for alcohols and for both neutral and deprotonated carboxylic acids in aqueous solution.

	Aqueous solution			
Organic molecule	Functionalized carbon atom		Carbon backbone	
Alcohols	BE / eV (±0.1)	FWHM / eV	BE / eV (±0.1)	FWHM / eV
CH_3-OH	291.8	1.4	—	—
C_2H_5-OH	291.6	1.1	290.1	1.3
C_3H_7-OH	291.3	1.1	290.0	1.3
i-C_3H_7-OH	291.5	1.1	290.0	1.2
C_4H_9-OH	291.2	1.0	289.9	1.3
Neutral Acids				
HCOOH	294.8	1.2	—	—
CH_3-COOH	294.7	1.2	290.8	1.2
C_2H_5-COOH	294.4	1.1	290.5	1.2
C_3H_7-COOH	294.3	1.1	290.2	1.2
C_4H_9-COOH	294.3	1.0	290.1	1.2
Deprotonated Acids				
$HCOO^-$	293.4	1.2	—	—
CH_3-COO^-	293.4	1.2	290.0	1.3
C_2H_5-COO^-	293.4	1.1	290.0	1.2
C_3H_7-COO^-	293.3	1.1	289.9	1.2
C_4H_9-COO^-	293.1	1.0	289.7	1.1

Fig. S4.3 shows the measured C 1s PE signal ratio for the organic species against the corresponding surface tension values as obtained from the literature. We can clearly see that XPS measurements in terms of measured functional group C 1s intensity correlates with the decrease in surface tension values, i.e., with increasing surface propensity of the organics. For one given type of functional group, this increase goes along with aliphatic carbon backbone length. The red line is a linear fit of the symbols and with its 95% confidence band.
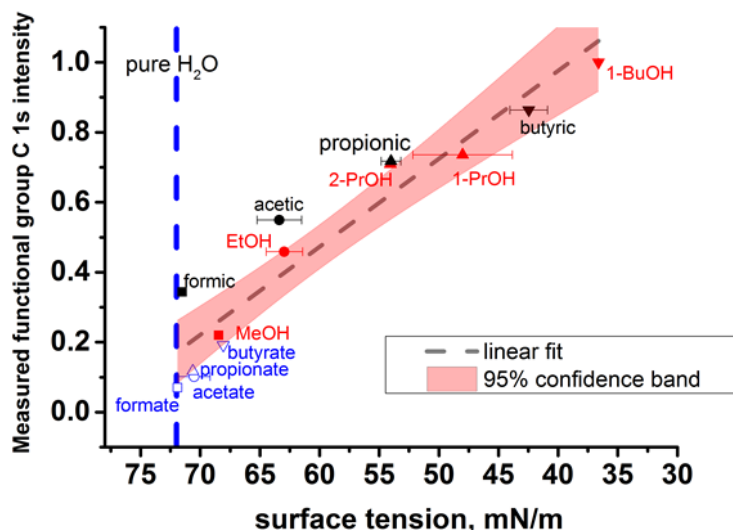
Fig. S4.3. Comparison of measured functional group C 1s intensity of organic species and the corresponding surface tension values. The red line is a linear fit of the data points and its 95% confidence band. The blue dashed line indicates the surface tension value of pure water.

The thermodynamic description of surface tension is directly related to the surface excess (Γ_{se}), Γ_i, of a component i beyond a theoretical dividing plane (referred to as the Gibbs surface) placed parallel to the solution surface by the Gibbs equation: (Adamson 1976)

$$\Gamma_i = -\frac{C_i}{RT}\left(\frac{\partial \gamma}{\partial C_i}\right)_T \qquad (S4.1)$$

where C_i is the mole fraction of component i, R is the universal gas constant and T is temperature in Kelvin. In solutions containing multiple species, different molecular arrangements can give rise to similar measures of surface tension, complicating direct interpretation of the results. The temperature range was between 293 and 300 K. The majority of surface tension values were taken at 298K.

Fig. S4.4 depicts exemplary surface tension data. To determine the surface excess of butyric acid at the interface the semi-empirical Meissner-Michaels equation was used to fit the surface tension data:(Meissner and Michaels 1949) (Langmuir 1917)

$$\gamma = \gamma_0\left[1 - b\ln(\frac{C_i}{a} + 1)\right] \qquad (S4.2)$$

where C_i is the concentration of butyric acid based on mole fraction, γ_0 is the surface tension without organics, and a and b are fitting parameters. The table in Fig. S4.4 details the fitting information for butyric acid.
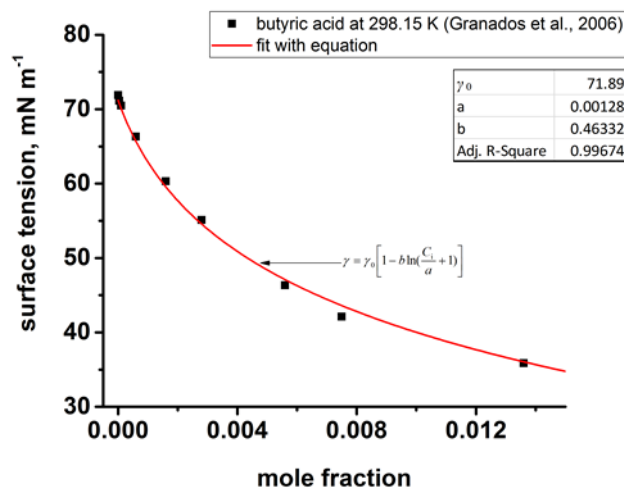

Fig. S4.4. Exemplary surface tension is plotted as a function of butyric acid mole fraction. The measured data are shown by symbol. The line displays the best fit of the data to the Meissner-Michael equation (S4.2). The values a and b are fitting parameters given in equation (S4.2).

Fig. S4.5 and S4.6 demonstrate the surface excess, Γ (first derivative of the surface tension as a function of the organic concentration) for butyric acid and for 1-butanol respectively. The determination of the surface excess was related to the Gibbs equation (S4.1).
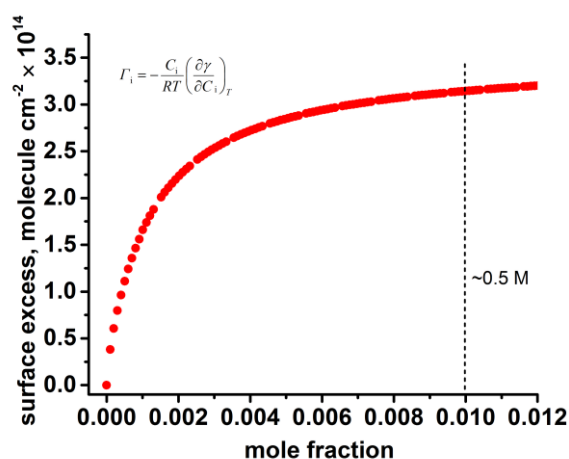

Fig. S4.5. Surface excess of butyric acid derived using the Gibbs equation and the experimental data from surface tension measurements. The dashed line indicates 0.01 mole fraction which corresponds to about 0.5 M of butyric acid.
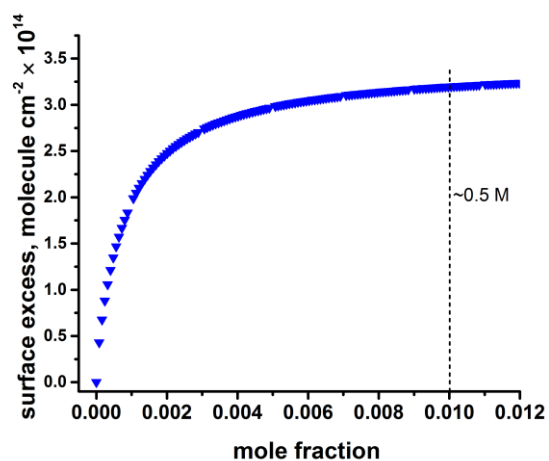
Fig. S4.6. Surface excess of 1-butanol as function of bulk concentration. The dashed line indicates 0.01 mole fraction which corresponds to about 0.5 M of 1-butanol.

Acknowledgments

References

Abramzon, A. A. and R. D. Gaukhberg (1993). "Surface-Tension of Salt-Solutions." Russian Journal of Applied Chemistry **66**(8): 1473-1480.

Adamson, A. G., Alice P. (1997). "Physical chemistry of surfaces, 6th edition." Wiley: New York.

Adamson, A. W. (1976). Physical Chemistry of Surfaces. New York, Wiley.

Aratono, M., T. Toyomasu, M. Villeneuve, Y. Uchizono, T. Takiue, K. Motomura and N. Ikeda (1997). "Thermodynamic Study on the Surface Formation of The Mixture of Water and Ethanol." Journal of Colloid and Interface Science **191**(1): 146-153.

Belda Maximino, R. (2009). "Surface Tension and Density of Binary Mixtures of Monoalcohols, Water and Acetonitrile: Equation of Correlation of the Surface Tension." Physics and Chemistry of Liquids **47**(5): 475-486.

Brown, M. A., M. Faubel and B. Winter (2009). "X-Ray Photo- and Resonant Auger-Electron Spectroscopy Studies of Liquid Water and Aqueous Solutions." Annual Reports Section "C" (Physical Chemistry) **105**(0): 174-212.

Brown, M. A., M.-T. Lee, A. Kleibert, M. Ammann and J. B. Giorgi (2015). "Ion Spatial Distributions at the Air- and Vacuum-Aqueous K2CO3 Interfaces." Journal of Physical Chemistry C **119**(9): 4976-4982.

Brown, M. A., A. B. Redondo, I. Jordan, N. Duyckaerts, M.-T. Lee, M. Ammann, F. Nolting, A. Kleibert, T. Huthwelker, J.-P. Maechler, M. Birrer, J. Honegger, R. Wetter, H. J. Woerner and J. A. van Bokhoven (2013). "A new endstation at the Swiss Light Source for ultraviolet photoelectron spectroscopy, X-ray photoelectron spectroscopy, and X-ray absorption spectroscopy measurements of liquid solutions." Review of Scientific Instruments **84**(7).

Brown, M. A., F. Vila, M. Sterrer, S. Thuermer, B. Winter, M. Ammann, J. J. Rehr and J. A. van Bokhoven (2012). "Electronic Structures of Formic Acid (HCOOH) and Formate (HCOO-) in Aqueous Solutions." Journal of Physical Chemistry Letters **3**(13): 1754-1759.

Brown, M. A., B. Winter, M. Faubel and J. C. Hemminger (2009). "Spatial Distribution of Nitrate and Nitrite Anions at the Liquid/Vapor Interface of Aqueous Solutions." Journal of the American Chemical Society **131**(24): 8354-8355.

Cropp, R. A., G. M. Kerr, S. M. Bengtson-Nash and D. W. Hawker (2011). "The Influence of Temperature and Ecosystem Dynamics on the Partitioning of a Persistent Organic Pollutant (POP) in Antarctic Marine Food Webs." 19th International Congress on Modelling and Simulation (Modsim2011): 2044-2050.

Dalleska, N. F., A. J. Colussi, A. M. Hyldahl and M. R. Hoffmann (2000). "Rates and mechanism of carbonyl sulfide oxidation by peroxides in concentrated sulfuric acid." Journal of Physical Chemistry A **104**(46): 10794-10796.

Donaldson, D. J. and D. Anderson (1999). "Adsorption of atmospheric gases at the air-water interface. 2. C-1-C-4 alcohols, acids, and acetone." Journal of Physical Chemistry A **103**(7): 871-876.

Donaldson, D. J. and K. T. Valsaraj (2010). "Adsorption and Reaction of Trace Gas-Phase Organic Compounds on Atmospheric Water Film Surfaces: A Critical Review." Environmental Science & Technology **44**(3): 865-873.

Eley, D. D. (1939). "On the solubility of gases. Part I. The inert gases in water." Transactions of the Faraday Society **35**(2): 1281-1292.

Eley, D. D. (1944). "The structure of water in aqueous solutions." Transactions of the Faraday Society **40**: 0184-0194.

Enami, S., M. R. Hoffmann and A. J. Colussi (2008). "Acidity enhances the formation of a persistent ozonide at aqueous ascorbate/ozone gas interfaces." Proceedings of the National Academy of Sciences of the United States of America **105**(21): 7365-7369.

Escher, B. I., R. P. Schwarzenbach and J. C. Westall (2000). "Evaluation of liposome-water partitioning of organic acids and bases. 1. Development of a sorption model." Environmental Science & Technology **34**(18): 3954-3961.

Faubel, M., S. Schlemmer and J. P. Toennies (1988). "A MOLECULAR-BEAM STUDY OF THE EVAPORATION OF WATER FROM A LIQUID JET." Zeitschrift Fur Physik D-Atoms Molecules and Clusters **10**(2-3): 269-277.

Faubel, M., B. Steiner and J. P. Toennies (1997). "Photoelectron Spectroscopy of Liquid Water, Some Alcohols, and Pure Nonane in Free Micro Jets." Journal of Chemical Physics **106**(22): 9013-9031.

Flechsig, U., F. Nolting, A. F. Rodriguez, J. Krempasky, C. Quitmann, T. Schmidt, S. Spielmann and D. Zimoch (2010). "Performance Measurements at the SLS SIM Beamline." AIP Conference Proceedings **1234**: 319-322.

Florian, J. and A. Warshel (1997). "Langevin Dipoles Model for Ab *Initio* Calculations of Chemical Processes in Solution: Parametrization and Application to Hydration Free Energies of Neutral and Ionic Solutes and Conformational Analysis in Aqueous Solution." Journal of Physical Chemistry B **101**(28): 5583-5595.

Frank, H. S. and M. W. Evans (1945). "FREE VOLUME AND ENTROPY IN CONDENSED SYSTEMS .3. ENTROPY IN BINARY LIQUID MIXTURES - PARTIAL MOLAL ENTROPY IN DILUTE SOLUTIONS - STRUCTURE AND THERMODYNAMICS IN AQUEOUS ELECTROLYTES." Journal of Chemical Physics **13**(11): 507-532.

G. Olivieri, A. G., A. Kleibert, M.A. Brown (2015). "Effect of X-Ray Spot Size on Liquid Jet Photoelectron Spectroscopy." Journal of Synchrotron Radiation.

Garrido, N. M., A. J. Queimada, M. Jorge, E. A. Macedo and I. G. Economou (2009). "1-Octanol/Water Partition Coefficients of n-Alkanes from Molecular Simulations of Absolute Solvation Free Energies." Journal of Chemical Theory and Computation **5**(9): 2436-2446.

Glinski, J., G. Chavepeyer, J. K. Platten and P. Smet (1998). "Surface Properties of Diluted Aqueous Solutions of Normal Short-Chained Alcohols." Journal of Chemical Physics **109**(12): 5050-5053.

Goss, K. U. and R. P. Schwarzenbach (2001). "Linear free energy relationships used to evaluate equilibrium partitioning of organic compounds." Environmental Science & Technology **35**(1): 1-9.

Granados, K., J. Gracia-Fadrique, A. Amigo and R. Bravo (2006). "Refractive Index, Surface Tension, and Density of Aqueous Mixtures of Carboxylic Acids at 298.15 K." Journal of Chemical and Engineering Data **51**(4): 1356-1360.

Gray-Weale, A. and J. K. Beattie (2009). "An explanation for the charge on water's surface." Physical Chemistry Chemical Physics **11**(46): 10994-11005.

Hoke, B. C. and J. C. Chen (1991). "Binary Aqueous Organic-Surface Tension Temperature-Dependence." Journal of Chemical and Engineering Data **36**(3): 322-326.

Hüfner, S. (1995). Photoelectron Spectroscopy. Berlin, Springer Verlag.

Krisch, M. J., R. D'Auria, M. A. Brown, D. J. Tobias, J. C. Hemminger, M. Ammann, D. E. Starr and H. Bluhm (2007). "The Effect of an Organic Surfactant on the Liquid-Vapor Interface of an Electrolyte Solution." Journal of Physical Chemistry C **111**(36): 13497-13509.

Langmuir, I. (1917). "The Constitution and Fundamental Properties of Solids and Liquids. II. Liquids." Journal of the American Chemical Society **39**: 1848-1906.

Lee, M.-T., M. A. Brown, S. Kato, A. Kleibert, A. Tuerler and M. Ammann (2015). "Competition between Organics and Bromide at the Aqueous Solution-Air Interface as Seen from Ozone Uptake Kinetics and X-ray Photoelectron Spectroscopy." Journal of Physical Chemistry A **119**(19): 4600-4608.

McKarns, S. C., C. Hansch, W. S. Caldwell, W. T. Morgan, S. K. Moore and D. J. Doolittle (1997). "Correlation between hydrophobicity of short-chain aliphatic alcohols and their ability to alter plasma membrane integrity." Fundamental and Applied Toxicology **36**(1): 62-70.

McNeill, V. F., J. Patterson, G. M. Wolfe and J. A. Thornton (2006). "The Effect of Varying Levels of Surfactant on the Reactive Uptake of N_2O_5 to Aqueous Aerosol." Atmospheric Chemistry and Physics **6**: 1635-1644.

Meissner, H. P. and A. S. Michaels (1949). "Surface Tensions of Pure Liquids and Liquid Mixtures." Industrial and Engineering Chemistry **41**(12): 2782-2787.

Minofar, B., P. Jungwirth, M. R. Das, W. Kunz and S. Mahiuddin (2007). "Propensity of Formate, Acetate, Benzoate, and Phenolate for the Aqueous Solution/Vapor Interface: Surface Tension Measurements and Molecular Dynamics Simulations." Journal of Physical Chemistry C **111**(23): 8242-8247.

Mishra, H., S. Enami, R. J. Nielsen, L. A. Stewart, M. R. Hoffmann, W. A. Goddard, III and A. J. Colussi (2012). "Bronsted basicity of the air-water interface." Proceedings of the National Academy of Sciences of the United States of America **109**(46): 18679-18683.

Ottosson, N., E. Wernersson, J. Soderstrom, W. Pokapanich, S. Kaufmann, S. Svensson, I. Persson, G. Ohrwall and O. Bjorneholm (2011). "The protonation state of small carboxylic acids at the water surface from photoelectron spectroscopy." Physical Chemistry Chemical Physics **13**(26): 12261-12267.

Petersen, P. B. and R. J. Saykally (2008). "Is the liquid water surface basic or acidic? Macroscopic vs. molecular-scale investigations." Chemical Physics Letters **458**(4-6): 255-261.

Prisle, N. L., A. Asmi, D. Topping, A. I. Partanen, S. Romakkaniemi, M. Dal Maso, M. Kulmala, A. Laaksonen, K. E. J. Lehtinen, G. McFiggans and H. Kokkola (2012). "Surfactant Effects in Global Simulations of Cloud Droplet Activation." Geophysical Research Letters **39**.

Pruyne, J. G., M.-T. Lee, C. Fábri, A. Beloqui Redondo, A. Kleibert, M. Ammann, M. A. Brown and M. J. Krisch (2014). "Liquid–Vapor Interface of Formic Acid Solutions in Salt Water: A Comparison of Macroscopic Surface Tension and Microscopic in Situ X-ray Photoelectron Spectroscopy Measurements." The Journal of Physical Chemistry C.

R. Sander, P. J. (2015). ""Henry's Law Constants" in NIST Chemistry WebBook, NIST Standard Reference Database Number 69, Eds. P.J. Linstrom and W.G. Mallard, National Institute of Standards and Technology, Gaithersburg MD, 20899, http://webbook.nist.gov, (retrieved July 17, 2015).".

Redondo, A. B., I. Jordan, I. Ziazadeh, A. Kleibert, J. B. Giorgi, H. J. Woerner, S. May, Z. Abbas and M. A. Brown (2015). "Nanoparticle-Induced Charge Redistribution of the Air-Water Interface." Journal of Physical Chemistry C **119**(5): 2661-2668.

Rouviere, A. and M. Ammann (2010). "The effect of fatty acid surfactants on the uptake of ozone to aqueous halogenide particles." Atmospheric Chemistry and Physics **10**(23): 11489-11500.

Sangster, J. (1989). "OCTANOL-WATER PARTITION-COEFFICIENTS OF SIMPLE ORGANIC-COMPOUNDS." Journal of Physical and Chemical Reference Data **18**(3): 1111-1229.

Saykally, R. J. (2013). "AIR/WATER INTERFACE Two sides of the acid-base story." Nature Chemistry **5**(2): 82-84.

Setny, P. (2015). "Hydration in Discrete Water (II): From Neutral to Charged Solutes." Journal of Physical Chemistry B **119**(19): 5970-5978.

Soderstrom, J., N. Martensson, O. Travnikova, M. Patanen, C. Miron, L. J. Saethre, K. J. Borve, J. J. Rehr, J. J. Kas, F. D. Vila, T. D. Thomas and S. Svensson (2012). "Nonstoichiometric Intensities in Core Photoelectron Spectroscopy." Physical Review Letters **108**(19).

Tian, C., N. Ji, G. A. Waychunas and Y. R. Shen (2008). "Interfacial structures of acidic and basic aqueous solutions." Journal of the American Chemical Society **130**(39): 13033-13039.

Tollefsen, K. E., K. Ingebrigtsen, A. J. Olsen, K. E. Zachariassen and S. Johnsen (1998). "Acute toxicity and toxicokinetics of 4-heptylphenol in juvenile Atlantic cod (Gadus morhua L.)." Environmental Toxicology and Chemistry **17**(4): 740-746.

Vaes, W. H. J., E. U. Ramos, C. Hamwijk, I. vanHolsteijn, B. J. Blaauboer, W. Seinen, H. J. M. Verhaar and J. L. M. Hermens (1997). "Solid phase microextraction as a tool to determine membrane/water partition coefficients and bioavailable concentrations in in vitro systems." Chemical Research in Toxicology **10**(10): 1067-1072.

Valsaraj, K. T. (1988). "On the Physicochemical Aspects of Partitioning of Non-Polar Hydrophobic Organics at the Air-Water-Interface." Chemosphere **17**(5): 875-887.

Vazquez, G., E. Alvarez and J. M. Navaza (1995). "Surface-Tension of Alcohol Plus Water from 20-Degrees-C To 50-Degrees-C." Journal of Chemical and Engineering Data **40**(3): 611-614.

Haynes, W. M. e. (Internet Version 2016). " "Physical Constants of Organic Compounds," in CRC Handbook of Chemistry and Physics, ." CRC Press/Taylor and Francis, Boca Raton, FL.

Winter, B. and M. Faubel (2006). "Photoemission from liquid aqueous solutions." Chemical Reviews **106**(4): 1176-1211.

Winter, B., M. Faubel, R. Vacha and P. Jungwirth (2009). "Reply to comments on Frontiers Article 'Behavior of hydroxide at the water/vapor interface'." Chemical Physics Letters **481**(1-3): 19-21.

Winter, B., R. Weber, W. Widdra, M. Dittmar, M. Faubel and I. V. Hertel (2004). "Full Valence Band Photoemission From Liquid Water Using Euv Synchrotron Radiation." Journal of Physical Chemistry A **108**(14): 2625-2632.

Wright, E. H. M. and B. A. Akhtar (1970). "Soluble Surface Films Of Short-Chain Monocarboxylic Acids On Organic And Aqueous Substrates." Journal of the Chemical Society B-Physical Organic(1): 151-157.

Chapter 5

5. The Competition between Organics and Bromide at the Aqueous Solution–Air Interface as seen from Ozone Uptake Kinetics and X-ray Photoelectron Spectroscopy

5.1. Abstract

A more detailed understanding of the heterogeneous chemistry of halogenated species in the marine boundary layer is required. Here, we studied the reaction of ozone (O_3) with NaBr solutions in presence and absence of citric acid ($C_6H_8O_7$) under ambient conditions. Citric acid is used as a proxy for oxidized organic material present at the ocean surface or in sea spray aerosol. On neat NaBr solutions, the observed kinetics is consistent with bulk reaction limited uptake, and a second order rate constant for the reaction of $O_3 + Br^-$ is 57 ± 10 M^{-1} s^{-1}. On mixed NaBr–citric acid aqueous solutions the uptake kinetics was faster than that predicted by bulk reaction limited uptake and also faster than expected based on an acid catalyzed mechanism. X-ray photoelectron spectroscopy (XPS) on a liquid microjet of the same solutions at $1.0 \times 10^{-3} - 1.0 \times 10^{-4}$ mbar was used to obtain quantitative insight into the interfacial composition relative to that of the bulk solutions. It revealed that the bromide anion becomes depleted by 30 ± 10 % while the sodium cation gets enhanced by 40 ± 20 % at the aqueous solution−air interface of a 0.12 M NaBr solution mixed with 2.5 M citric acid in the bulk, attributed to the role of citric acid as a weak surfactant. Therefore, the enhanced reactivity of bromide solutions observed in presence of citric acid is not necessarily attributable to a surface reaction but could also result from an increased solubility of O_3 at higher citric acid concentrations. Whether the acid catalyzed chemistry may have a larger effect on the surface than in the bulk to offset the effect of bromide depletion also remains open.

5.2. Introduction

Halogen species are of significant interest in the atmospheric chemistry of the marine boundary layer. By the action of oxidants, halide ions (chloride, Cl^-; bromide, Br^-; iodide, I^-) present in sea water and in sea spray aerosol can be converted into gas phase species such as molecular halogens (Cl_2, Br_2, I_2, and interhalogen compounds). These molecular halogen compounds represent a source of halogen atoms upon photolysis. These are implicated in catalytic cycles affecting the ozone (O_3) budget of the marine boundary layer. Halogens are therefore representing a substantial O_3 sink in the troposphere at a global level (Foster, Plastridge et al. 2001, Simpson, von Glasow et al. 2007, Saiz-Lopez, Lamarque et al. 2012).

The reactions of O_3 with Br^- and I^- ions are believed be one of the significant sources of gas phase halogen compounds (Simpson, von Glasow et al. 2007, Carpenter, MacDonald et al.

2013). In a first step, these reactions lead to HOBr and HOI, respectively, which then react further with halide ions to form BrCl or Br_2 and ICl or I_2, respectively. The kinetics of these reactions has already been studied under a range of conditions. They were relevant to ocean water (Carpenter *et al.* (Carpenter, MacDonald et al. 2013) for I^-; Oldridge and Abbatt (Oldridge and Abbatt 2011) for Br^-), the higher ionic strength environment of sea spray aerosol or sea ice, (Clifford and Donalson (Clifford and Donaldson 2007), Hunt *et al.* (Hunt, Roeselova et al. 2004) and Oldridge and Abbatt (Oldridge and Abbatt 2011) for Br^-; Rouviere *et al.* (Rouviere, Sosedova et al. 2010) for I^-) and in the context of waste water treatment (Haag and Hoigné (Haag and Hoigne 1983) for Br^-, Fono and Sedlak (Fono and Sedlak 2007) for I^-). Several of these studies have suggested the involvement of surface specific reactions (Hunt, Roeselova et al. 2004, Oldridge and Abbatt 2011). These surface specific reactions have been concluded based on the saturating behavior of the Br_2 formation rate as a function of the Br^- concentration at high (M) Br^- concentrations (Clifford and Donaldson 2007) or based on the inverse dependence of the Br_2 formation rate of the O_3 concentration at low Br^- concentration relevant for ocean water (Oldridge and Abbatt 2011). Surface reactions would significantly alter the net effect of these reactions on the halogen cycling in the gas phase, especially in the high surface to volume ratio environment of a marine aerosol (Hunt, Roeselova et al. 2004). Suggestions for surface reactions of halide ions were partially motivated by the propensity of the larger, more polarizable halide ions for the aqueous solution–air interface (Jungwirth and Tobias 2001, Jungwirth and Tobias 2002).
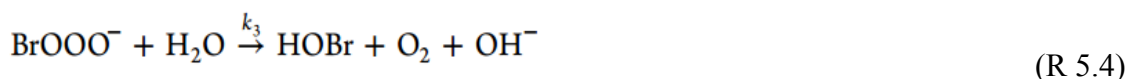
At first sight, this propensity for the interface seemed contrary to the traditional picture that image-charge repulsion should push ions away from the surface, which was supported by an increase of the surface tension with increasing salt concentration. This inconsistency had been resolved by Jungwirth and Tobias (Jungwirth and Tobias 2006) by MD simulations demonstrating a relative ion density-profile at the sodium halide salt solution–air interface. These showed a structured layer with the larger, more polarizable anions, such as I^- and Br^-, enhanced at the outermost surface followed by a layer in which the cation concentration is enhanced and the I^- or Br^- ion concentration is depleted. This picture was confirmed by direct measurements of the depth profile of anion to cation ratios by means of X-ray photoelectron spectroscopy (XPS) (Ghosal, Hemminger et al. 2005).

In this study, we focus on the reaction of gaseous O_3 with Br^- as our model system:

$$O_3 + Br^- \rightarrow OBr^- + O_2 \qquad \text{(R5.1)}$$

The net rate constant is sufficiently low ($k_b^{II} = 258$ M^{-1} s^{-1} at 298 K) (Liu, Schurter et al. 2001) that a surface reaction could manifest by an increase in reactivity, as suggested by Oldridge and Abbatt (Oldridge and Abbatt 2011). In contrast to that, the reaction of O$_3$ with I$^-$ is orders of magnitude faster (O$_3$ + I$^-$ $\rightarrow$ OI$^-$ + O$_2$, $k_b^{II} = 2 \times 10^9$ M^{-1} s^{-1} at 298 K) (Garland, Elzerman et al. 1980) and the aqueous bulk phase sink is so strong that a surface reaction has not become rate limiting in previous studies (Hu, Shi et al. 1995, Rouviere, Sosedova et al. 2010).

Liu et al. (Liu, Schurter et al. 2001) have suggested an acid catalyzed mechanism for (R 5.1), where O$_3$ reacts with Br$^-$ to form the steady-state intermediate BrOOO$^-$ (R 5.2). This intermediate would subsequently react with H$^+$ or H$_2$O to give HOBr and O$_2$ (R 5.3 and R 5.4).

$$O_3 + Br^- \underset{k_{-1}}{\overset{k_1}{\rightleftharpoons}} BrOOO^- \qquad \text{(R5.2)}$$

$$BrOOO^- + H^+ \overset{k_2}{\rightarrow} HOBr + O_2 \qquad \text{(R 5.3)}$$

$$BrOOO^- + H_2O \overset{k_3}{\rightarrow} HOBr + O_2 + OH^- \qquad \text{(R 5.4)}$$

The ocean surface water and sea spray aerosol derived therefrom contain a complex mixture of not only inorganic salts but also organic compounds deriving from marine biota (O'Dowd, Facchini et al. 2004, Kanakidou, Seinfeld et al. 2005, Vignati, Facchini et al. 2010, Donaldson and George 2012). In the context of the present study, an important aspect of organics is that they may have a significant effect on the way halide ions are distributed at the interface (Krisch, D'Auria et al. 2007), that they hinder the mass transfer between the gas and particle phases (e.g., Rouviere and Ammann (Rouviere and Ammann 2010)) at the aqueous− air interface or even promote it (Faust, Dempsey et al. 2013, Morris 2013). Therefore, one of the main goals of the present study was to understand the effect of an organic compound on the reaction of gaseous O$_3$ with NaBr solution using a flow reactor approach. We chose citric acid (CA) (2-hydroxypropane-1,2,3-tricarboxylic acid, C$_6$H$_8$O$_7$) as a proxy for very soluble,

highly oxidized and highly functionalized organic compounds that result from photo-oxidation of primary organic compounds. Moreover, CA has been identified in aerosol particles and has been frequently used as model substance for experiments related to its thermodynamic and viscous properties (Laguerie, Aubry et al. 1976, Zardini, Sjogren et al. 2008, Lienhard, Bones et al. 2012, Lienhard, Huisman et al. 2014). For this it might also be important that CA is only a weak surfactant; the surface tension decrease is rather small and becomes noticeable only at high concentration (Varga, Kiss et al. 2007, Mahiuddin, Minofar et al. 2008).

As in the direct experimental verification of the halide enrichment at the aqueous solution–air interface (Ghosal, Hemminger et al. 2005, Ghosal, Brown et al. 2008) and the effect of surfactants on the latter (Krisch, D'Auria et al. 2007), the method of choice to assess interfacial composition for the present work is X-ray photoelectron spectroscopy (XPS). XPS is a surface-specific method capable of probing the aqueous–air interface (Winter and Faubel 2006, Brown, Faubel et al. 2009), and provides a means to quantify elemental composition at the interface. Since the electron's inelastic mean free path (IMFP) is short, photoelectrons can only escape without loss of energy from a few nm, with a minimum of about 10 Å in the region of 100 eV kinetic energy (KE) (Thurmer, Seidel et al.). When implemented with a liquid microjet, the liquid surface is renewed rapidly enough to remain contamination-free (in particular free of the ubiquitous carbon) (Pruyne, Lee et al. 2014), and the results are not affected by beam damage (Winter 2009).

In this work we have performed complementary kinetic and spectroscopic experiments with liquid microjet XPS (LJ-XPS) to directly assess the interplay between Br^- ions and organics and the effect it potentially has on the kinetics of the reaction between O_3 and Br^- in an environment that has relevance for the ocean surface or sea spray particles (Prather, Bertram et al. 2013).

5.3. Methods

5.3.1. Flow reactor

Experiments were done with an atmospheric pressure flow reactor setup (see Fig. S2.12 in *Chapter 2*) in which the solution of interest is contained in a shallow trough, over which a gas containing O_3 is passing. O_3 was produced by photolysis of a small flow of oxygen (20-100 mL min^{-1}) at 185 nm UV light provided by an Hg penray lamp. By varying the power of the

Hg penray lamp the level of O_3 concentration could be adjusted. The flow containing O_3 was mixed with a carrier gas flow (N_2, 920-1000 mL min^{-1}) and passed either through a 1.5 m long FEP bypass-tube at room temperature or through the flow reactor. Part of the flow exiting the flow reactor was pumped to the O_3 analyzer (Teledyne technologies, model 400E). The reactor has planar geometry and it has cooling coils to allow circulating a thermo-stated fluid to control the temperature. The latter was set to 15.7 °C to allow operation at saturated conditions with respect to water vapor inside the flow reactor, and to avoid high humidity in gas lines upstream, downstream and within the O_3 analyzer. The geometry of the flow reactor is similar to that used in a previous study (Knopf, Cosman et al. 2007), but is operated at atmospheric pressure. O_3 of known concentration was passed over the surface of the solution of interest, which was filled into a quartz trough. The head-space (gas channel) above the liquid surface has a width of 32 mm and a height (h) of 4.5 mm which is narrow enough to avoid gas phase diffusion limitations over a length of 400 mm for the small rates of uptake of the present experiments. The liquid surface is 27.5 mm wide (w) and 398 mm long (l). The thickness of the liquid can be varied from 0.8 to 1.5 mm which is significantly larger than the reacto-diffusive length (max few μm, see below) of O_3 under all conditions. The initial and the end parts of the gas channel are designed to facilitate laminar flow.

An example of raw data of O_3 uptake on an aqueous solution containing NaBr is shown in *Chapter 2*, Fig. S2.13. The loss of O_3 to the solution was observed by the difference between the O_3 concentrations measured when the carrier gas passed through the bypass and through the reactor, respectively. The detection limit in terms of O_3 loss was ± 0.5 ppb. The loss of O_3 was constant over the typical period of an experiment between 30 min and 2 hours, characteristic of steady-state uptake. The Br$^-$ concentration remained in excess for all reaction times and O_3 concentrations.

5.3.2. Concept for kinetic data analysis

Heterogeneous kinetics is usually reported in terms of a net loss rate normalized to the gas kinetic collision rate to the surface involved. This is expressed in the form the uptake coefficient for O_3 is defined as

$$\gamma = \frac{\textbf{number of O}_{3(g)} \textbf{ molecules lost}}{\textbf{number of collisions between O}_{3(g)} \textbf{and the surface}}$$

(E 5.1)

As (E 5.1) indicates, the reactive uptake coefficient, γ, is determined by the amount of O_3 molecules lost per unit surface area and unit time, i.e., the difference between the background O_3 concentration, $[O_3]_{bg}$, and the level of O_3 when the heterogeneous reaction takes place, $[O_3]_{hg}$. A correction was applied to the uptake data to correct for O_3 loss ($\Delta[O_3]_{water}$) observed for control experiments with pure water, which includes loss of O_3 to all surfaces involved, including inlet and the ceiling above the trough. The loss of O_3 along the trough is treated as a pseudo-first-order process assuming excess bulk Br^- concentration (i.e., the Br^- concentration does not significantly change neither with time nor with length along the reactor). The pseudo-first order rate constant, k_{obs}, in length base (cm^{-1}) is obtained from the initial (background) concentration and the concentration at the end of the trough by $k_{obs} = [\ln ([O_3]_{hg} + \Delta[O_3]_{water}) - \ln ([O_3]_{bg})] \times \varphi / (l \times h \times w)$, where w, h and l are the width, thickness and length, respectively, of the liquid surface in the quartz though, and φ is the volumetric flow rate of the carrier gas.

The characteristic time for diffusion across the height of the reactor is $h^2/D \approx 1.5$ s, two times less than the residence time of the carrier gas in the reactor. The total loss rate of O_3 within the reacto-diffusive depth (≈ 5 μm, see below) of the liquid phase is 2.6 % of the total supply rate of O_3 to the reactor. For the uptake coefficients of the present study in the 10^{-6} range, the apparent first order loss rate constant for the uptake into the liquid phase (on a time basis) is $\gamma \omega / 4 / h \approx 0.02$ s^{-1}, which is much smaller than that for diffusion in the gas phase $D/h^2 \approx 0.7$ s^{-1}). Therefore, taken together, diffusion limitation can be safely neglected.

Under these conditions, we can obtain the relationship between γ (unitless) and k_{obs} from:

$$\gamma = \frac{4 k_{obs} \varphi}{w \omega}$$

(E 5.2)

where ω is the mean thermal velocity of O_3 in the gas phase.

The uptake coefficient represents a normalized loss rate and depends on the elementary processes involved in the condensed phase. It is typically represented by a resistor formulation (Hanson, Ravishankara et al. 1994, Ammann, Cox et al. 2013):

$$\frac{1}{\gamma} = \frac{1}{\alpha_s} + \frac{1}{\Gamma_s + \left(\frac{1}{\Gamma_{sb}} + \frac{1}{\Gamma_b}\right)^{-1}}$$

(E 5.3)

α_s represents the surface accommodation coefficient, i.e., the probability for adsorption on the surface; Γ_s the limiting rate for surface reaction, Γ_{sb} the limiting rate for surface to bulk transfer, and Γ_b the limiting rate for a reaction in the bulk. Under conditions, where adsorption on the surface and surface to bulk transfer are both not rate limiting (which is likely the case in the present case), (E 5.3) can be simplified to:

$$\gamma = \Gamma_s + \Gamma_b$$

(E 5.4)

Under conditions, where reaction in the bulk competes with the diffusive transport of the dissolved trace gas, the limiting rate can be written as,

$$\Gamma_b = \frac{4RTH\sqrt{Dk_b^I}}{\omega}$$

(E 5.5)

where R is the gas constant, T is the temperature, H is the Henry's law constant for the gas-phase molecule in the liquid phase, and D is its diffusion coefficient in the liquid phase. k_b^I is the first order liquid-phase loss rate constant for dissolved O_3 in presence of Br^-, i.e., k_b^I (s^{-1}) $= k_b^{II} \times [Br^-]_b$. where $[Br^-]_b$ is the bulk concentration of Br^- in units of mole per liter and k_b^{II} (M^{-1} s^{-1}) is the second-order liquid-phase rate constant for the net reaction between O_3 and Br^- (R 5.1). The competition between reaction and diffusion in the liquid phase is best assessed by the so-called reacto-diffusive length, l_{rd}, which is the length within which the bulk concentration of O_3 drops to 1/e of its initial value near the surface:

$$l_{rd} = \sqrt{\frac{D}{k_b^I}}$$

(E 5.6)

Therefore, the boundary condition is that l_{rd} is much smaller than the thickness of the liquid in the trough, which is the case for all experiments presented in this study.

On the other hand, surface reactions of O_3 on either solid or liquid substrates are often obeying Langmuir-Hinshelwood kinetics, by way of a reaction between a surface-species and an adsorbed species that is in equilibrium with the gas-phase O_3. This mechanism has also been suggested for the reaction of O_3 with Br^- (Oldridge and Abbatt 2011). The corresponding limiting uptake coefficient can be described as (Ammann, Cox et al. 2013),

$$\Gamma_s = \frac{4k_s^{II}\left[Br^-\right]_s K_{LangC}(O_3)N_{max}}{\omega(1+K_{LangC}(O_3)[O_3]_g)}$$ (E 5.7)

Equation (E 5.7) demonstrates that Γ_s depends on the gas phase concentration of O_3, if K_{LangC} $(O_3)[O_3]_g$ is similar to or larger than 1 (i.e., at high coverage). Here N_{max} is the maximum surface coverage of O_3 on the surface), K_{LangC} is the Langmuir adsorption equilibrium constant of O_3, $[O_3]_g$ is the concentration of O_3 in the gas phase, and k_s^I is the first-order surface-phase rate constant for the $O_3 + Br^-$ reaction, given by k_s^I $(s^{-1}) = k_s^{II} \times [Br^-]_s$, where $[Br^-]_s$ is the concentration of Br^- at the surface in units of molecule cm^{-2} and k_s^{II} (cm^2 s^{-1} $molecule^{-1}$) is the second-order surface-phase rate constant.

5.3.3. Liquid microjet XPS

We made use of the near ambient pressure photoemission endstation (NAPP) with the liquid microjet setup (Brown, Redondo et al. 2013). Liquid microjet XPS (LJ-XPS) has become an established technique (Brown, Faubel et al. 2009, Winter 2009), and our setup has been described in detail elsewhere (Brown, Beloqui Redondo et al. 2013). Measurements were made at the Surfaces/Interfaces: Microscopy (SIM) beamline of the Swiss Light Source (SLS) at Paul Scherrer Institute (PSI) (Flechsig, Nolting et al. 2010).

The electron analyzer uses a three-stage differentially pumped electrostatic lens system and a hemispherical analyzer to collect photoelectrons from samples in chamber pressures up to a few mbar. For the present experiments, a quartz nozzle, forming a liquid microjet with a diameter of 19 μm, was used to deliver a liquid sample into the vacuum chamber (see Fig. S5.1). The liquid was cooled to 279 K immediately before entry into the ionization chamber and a flow rate of 0.35 mL/min was used (see Fiqure S1 for a simple schematic of the setup). The chamber pressure with the jet running was between 1.0×10^{-3} and 1.0×10^{-4} mbar. The jet was adjusted to spatially overlap with the 100 μm (vertical) by 60 μm (horizontal) synchrotron light beam (Flechsig, Nolting et al. 2010). The photoelectrons from the liquid

surface entered the analyzer through an orifice (skimmer) with a diameter of 500 μm. The working distance between the liquid jet and the detector orifice was 500 μm.

A complete description of the equilibrated nature of a liquid microjet under the conditions of photoemission experiments has been given in the literature previously (Faubel, Steiner et al. 1997, Brown, Faubel et al. 2009). In the context of interest in this study, it is important that the surface active organic species (citric acid) can reach its equilibrium concentration at the surface until the jet is hit by the X-ray beam. The evolution of the surface concentration of an initially free surface by diffusion from the bulk with time is given by Equation (E 5.8) (Winter and Faubel 2006):

$$c_s = 2(D/\pi)^{1/2} \, ct^{1/2} \tag{E 5.8}$$

For a 1 M solution with $c = 6 \times 10^{20}$ molecules of solute per cm^3 of liquid with a diffusion coefficient of $D = 2 \times 10^{-5} \, cm^2 \, s^{-1}$, the formation of a monolayer on the surface with $c_s = 2 \times 10^{14}$ molecules per cm^2 in water takes approximately $t \approx 4$ ns. On the other hand, the liquid jet, under our operating conditions, moves with a speed of about $20 \, m \, s^{-1}$ to the observation region (laminar flow) at 2 mm distance from the nozzle exit in 100 μs, which is long enough to allow establishing surface–bulk equilibrium.

Spectra for obtaining core level spectra of Br 3d, Na 2s, C 1s and O 1s at about the same kinetic energy were not taken each one after the other with setting the beamline energy to the appropriate energy value in between. We set the primary photon energy for the detection of Br 3d and Na 2s to 229 eV, resulting in a photoelectron KE of about 155 eV and 160 eV, respectively. We made use of the around 10% of photon flux associated with 2nd order light, which simultaneously passes the monochromator with photon energies of 458 eV, to ionize the C 1s orbital for a KE of 163-167 eV. The even smaller amounts of 3rd order light at 687 eV were used to excite the O 1s orbital for a KE of 148.9 eV for liquid water. This procedure allowed to determine photoemission signals for each element within one sweep of the electron analyzer in a relatively narrow kinetic energy range.

Three concentrations (0.03, 0.06, 0.12 mole/L) of sodium bromide (NaBr, BioXtra ≥99.0%, Sigma-Aldrich) in 0.5, 1.35, and 2.5 mole/L citric acid, CA, (ACS reagent, ≥99.5% , Sigma-Aldrich) were prepared for analysis. The solutions were prepared by adding stock solutions of NaBr and CA to Milli-Q water (Millipore, 18.2 MΩ cm at 25 °C).

5.4. Results and discussion

5.4.1. Heterogeneous kinetics

Fig. 5.1 presents the uptake coefficient of O_3, γ, as a function of the square root of the Br^- concentration for neat NaBr solutions and at three O_3 concentrations in the gas phase. At all three gas phase concentrations, the linear increase of γ is consistent with the reacto-diffusive uptake regime according to equation (E 5.5). At the two higher concentrations, the γ values exhibit the same slope, while at the lowest concentration the slope appears to be lower. The error bars represent the uncertainty including scatter among replicates and the estimated error from the precision of the O_3 analyzer for the higher O_3 concentrations. As mentioned in the methods section, a correction was applied to the uptake data to correct for O_3 loss observed for control experiments with pure water. We note that for the lowest O_3 concentration this correction was similar in magnitude as the O_3 loss in presence of Br^-, so that the correction induced a large uncertainty on the value of γ. We therefore include the uptake coefficient calculated from the uncorrected O_3 loss as the upper end of the error bar to express this uncertainty.

Solute activity coefficients for the mixed solutions of citric acid with NaBr used here are not available, and applying methods for estimating them would probably bring in more uncertainty. We therefore used molarity as a metric throughout. The literature value for the diffusion coefficient of O_3 in water is taken to be 1.55×10^{-9} m^2 s^{-1} (Johnson and Davis 1996), the Henry's law constant of O_3 in solution is taken to be 1.51×10^{-2} M atm^{-1} (Chameides 1984), both at 15.7 °C (again assuming ideality). The blue line is the result of a fit to the data for the two higher concentrations according to (E 5.5) with the liquid-phase rate constant, k_b^{II}, for the net reaction of O_3 with Br^- as variable. The resulting value for k_b^{II}, 57 ± 10 M^{-1} s^{-1}, turns out to be below the value of 160 M^{-1} s^{-1} reported by Haag and Hoigné (Haag and Hoigne 1983). Also, Oldridge and Abbatt (Oldridge and Abbatt 2011) noted that for their highest O_3 concentration uptake data, which they attributed to the same uptake regime, the rate constant by Haag and Hoigné overpredicted their observed uptake coefficient. As apparent from Fig. 5.1, their uptake coefficient under those conditions (lower Br^- concentration) lies close to the best fit line to our data. We note the temperature difference between their (0 °C) and our (15.7 °C) experiment. In neat NaBr solutions, the activity coefficient of Br^- over the concentration range 0.1 to 1 M ranges from 0.74 to 0.59 (Khoshkbarchi and Vera 1996). This would then lead to a correction of the rate constant by

about a factor of 1.5, which could help explaining part of the discrepancy between our data and that of Haag and Hoigné obtained at lower Br^- concentration.
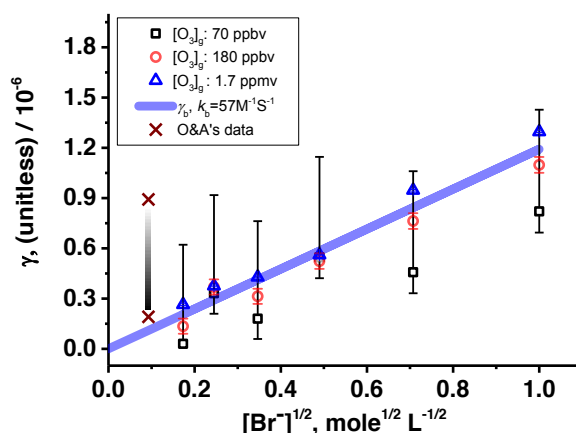

Fig. 5.1. γ vs $[Br^-]^{1/2}$ for neat NaBr aqueous solutions at 15.7 °C, $[O_3]_g = 2 \times 10^{12}$ molecules/cm^3 (squares), 5×10^{12} molecules/cm^3 (circles), and 4.4×10^{13} molecules/cm^3 (triangles)(see text for description of error bars). The blue line represents a fit to the data for the two higher O_3 concentrations based on equation (E 5.5) (see text). The dataset by Oldridge and Abbatt (Oldridge and Abbatt 2011) in 0.5 M NaCl solutions at 0 °C is represented by the two crosses and the vertical bar with the grey scale applied to symbols represents the O_3 concentrations (the darker the higher).

The main difference to the Oldridge and Abbatt study is that within uncertainty our data show no significant dependence on O_3 concentration in the gas phase that would be in accordance with equation (E 5.7). The apparently positive dependence of the uptake coefficient of the O_3 concentration is not significant, as indicated by the large error bars. As apparent from the measured uptake coefficient without this correction shown as upper end of the error bars at the lowest O_3 concentration, no correction would result in a negative dependence of O_3 concentration. Therefore, we remain careful with the conclusion about the absence of a surface reaction. In our study, we could only reach gaseous O_3 concentrations up to 4.4×10^{13} molecules cm^{-3}, which is more than 5 times less than what Oldridge and Abbatt were reaching (2.5×10^{14} molecules cm^{-3}). They worked with an 8.6 mM Br^-/0.5 M Cl^- solution adjusted to pH 1.95 at 0 °C in their experiments, while we used relatively high Br^- concentration solutions i.e. 0.03 to 1 M in the absence of chloride and at their native pH values. Last but not least, the reactive uptake coefficient for O_3 was determined based on the Br_2 production rate by Oldridge and Abbatt, while we determined the uptake coefficient for O_3 based on its loss from the gas phase. Fig. 5.2 presents O_3 uptake coefficient as a function of the square root of the Br^- concentration in presence of 2.5 M CA and at two O_3 concentrations in the gas phase.

Due to the larger uncertainty, as discussed for the data in absence of CA, we do not include data at the lowest concentration. Also in this case, we did not see a significant dependence on the O_3 concentration. The slope of γ with Br^- concentration is substantially higher in presence of CA than for the neat NaBr solution. The liquid-phase diffusion coefficient of O_3 for the CA containing solution is smaller than that of O_3 in neat NaBr solution, due to its higher viscosity. We used the viscosity data from Laguerie *et al.* (Laguerie, Aubry et al. 1976) and applied the Stokes-Einstein relation (E 5.9) to estimate the diffusion coefficient of O_3 in the 2.5 M CA solution to be $1.0 \times 10^{-9}\, m^2\, s^{-1}$.

$$D = \frac{k_{\mathrm{B}}T}{6\pi\eta r} \qquad\qquad (E\ 5.9)$$

In (E 5.9), D is the diffusion constant; k_{B} is Boltzmann's constant; T is the absolute temperature; η is the dynamic viscosity of 2.5 M citric acid; r is the radius of the spherical O_3 molecular. Taking into account this change in diffusion coefficient, but keeping all other parameters the same as for the neat NaBr solution case, leads to the blue line in Fig. 5.2, which clearly underestimates the observed uptake by far.

To discuss the enhanced reactivity of the solutions in presence of citric acid, we consider two scenarios: i) if we accept the linear dependence of γ of the square root of the Br^- concentration as an indication of reacto-diffusive uptake into the bulk, the slope of the increase of γ with Br^- concentration is determined by the product: $H \times [k_b^{II}]^{\frac{1}{2}}$. Therefore, within this scenario, we need to discuss changes in the solubility (H) or the second order rate constant. ii) In the second scenario we consider the option that the difference between the observed reactivity and that explained by the bulk reaction is partly or completely driven by a surface reaction as suggested by Oldridge and Abbatt (Oldridge and Abbatt 2011). We note that dropping the assumption of ideal solutions would not change the mechanistic interpretation, since plotting the uptake coefficient on an activity scale would still lead to an equivalent linear dependence of the uptake coefficient of the square root of activity.

Scenario i) Since the addition of citric acid brings about a substantial drop in pH of the solution, we consider the acid catalyzed mechanism (R 5.2-R 5.4) suggested by Liu *et al.* (Liu, Schurter et al. 2001) based on kinetic data. Since their absolute rate coefficient for the net reaction $O_3 + Br^-$ (R 5.1) for the neat NaBr solution calculated for our experimental

conditions is a factor of 2.86 higher than ours, we only consider the relative change in k_b^{II} as a function of pH, given by equation (E 5.10).

$$k_b^{II} = \frac{k_1\left(\frac{k_2}{k_{-1}}[\mathbf{H}^+] + \frac{k_3}{k_{-1}}\right)}{1 + \frac{k_2}{k_{-1}}[\mathbf{H}^+] + \frac{k_3}{k_{-1}}}$$

(E 5.10)

The indices to the rate coefficients in (E 5.10) refer to the number of the reaction given in the introduction section. Based on reaction (R 5.2-R 5.4), the relative change in the rate constant from neutral conditions to pH=0.9 at 2.5 M CA is a factor of 2.86, leading to 103.69 M^{-1} s^{-1}. This rate constant leads to the green line shown in Fig 5.2.

The solubility of O_3 in organic solvents tends to be higher than in water, e.g., a factor of 1.7 in pure acetic acid (Bin 2006). Together with k_b^{II} = 103.69 M^{-1} s^{-1} for the acidic case, we would need an increase of H (O_3) in citric acid by about a factor of 1.4 to bring γ according to (E 5.5) into agreement with observed values (red solid line in Fig. 5.2). Therefore, uncertainties in the acid catalyzed mechanism, the rate constant in neat NaBr solution, and in the solubility could render this scenario an option to explain the measured data.
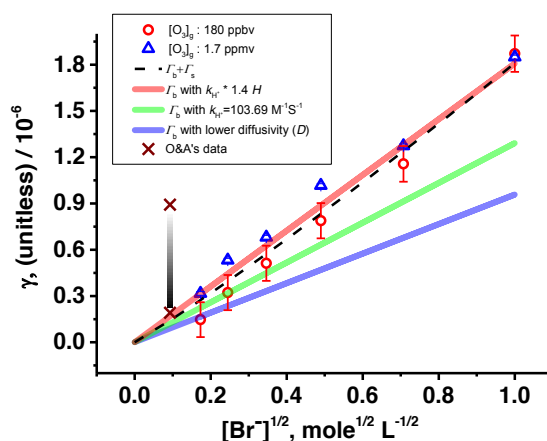
Fig. 5.2. Measured γ vs [Br$^-$]$^{1/2}$ for mixed NaBr–citric acid aqueous solutions at 15.7 °C, [O_3]$_g$ =5 × 10^{12} molecules cm^{-3} (circles), and 4.4 × 10^{13} molecules cm^{-3} (triangles). The solid lines lines represent the expected behavior for γ based on the measurements on neat NaBr solution (blue), the acid catalyzed mechanism (green) and an additional increase in solubility of O_3 (red). The dashed curve represents the sum of the acid catalyzed bulk reaction and a surface reaction component obtained according to (E 5.7). See text for details. The dataset by Oldridge and Abbatt (Oldridge and Abbatt 2011) in 0.5 M NaCl solutions at 0 °C is represented by the two crosses and the vertical bar with the grey scale applied to symbols represents the O_3 concentrations (the darker the higher).

Scenario ii) In this scenario, we consider the option that the difference between the reactivity explained by the acid catalyzed bulk reaction (green line in Fig. 5.2) and the observed data is caused by a surface component adding to the latter (E 5.4, E 5.7). In many cases this option has been suggested based on the negative concentration dependence of the uptake coefficient (E 5.7), as also by Oldridge and Abbatt (Oldridge and Abbatt 2011). Since the change in regime from constant uptake coefficient to its inverse concentration dependence occurs at $K[O_3]_g \approx 1$, where the surface becomes saturated in adsorbed O_3, and since the maximum surface coverage may be different on different substrates, we may have missed the concentration range of O_3, where the surface coverage reaches its maximum, and where the uptake coefficient would have become sensitive to the gas phase concentration. It would indicate that the presence of citric acid enhances either the Br^- concentration at the surface and/or its reactivity through the acid catalyzed mechanism. The dashed curve in Fig. 5.2 represents the sum of the bulk reaction component (green line) and a surface reaction component obtained according to (E 5.7) by taking K_{langC} as estimated by Ammann *et al.* (Ammann, Cox et al. 2013), and by assuming that N_{max} is equivalent to the Br^- concentration on the surface which is proportional to the bulk Br^- concentration, and then by adjusting k_s^{II} to fit the data. The non-linear shape is due to the linear dependence of the surface reaction rate on the concentration. In view of the scatter of the data, this scenario also allows to explain the data. In order to further explore the availability of Br^- at the interface, we performed XPS on a liquid microjet of the same solutions to obtain quantitative insight into the interfacial composition of them.

5.4.2. Liquid microjet XPS

Fig. 5.3 shows combined O 1s, Br 3d, Na 2s, and C 1s photoelectron spectra from 0.12 M NaBr aqueous solutions as a function of the citric acid concentration taken at the nominal photon energy of 229 eV and making use of the higher order light components to obtain C 1s and O 1s in the same kinetic energy (KE) window as described in the methods section. This obviously goes at the expense of signal-to-noise ratio for O 1s and C1s, but has the advantage to obtain photoemission signals for all four elements at once. Higher signal-to-noise spectra obtained separately for each core level region measured with standard first order light are shown in the supporting information Fig. S5.2 along with the details of how the peaks were fit. The spin-orbit split bromine levels Br^- $3d_{3/2,5/2}$ appear at a photoelectron KE of about 155 eV. Na 2s is observed at 160.7 eV KE. C 1s, excited by photons at around 458 eV, appears in

the spectrum at photoelectron KEs of 164.4 eV (carboxyl C), 166.6 eV (alcohol C) and 168.2 eV (aliphatic C) (Krisch, D'Auria et al. 2007, Ketteler, Ashby et al. 2008), consistent with the presence of the three functional groups in citric acid. O 1s was excited by a photon energy of 687 eV. The lower KE peak (147.1 eV) with smaller full width half maximum (fwhm) is assigned to gas phase water molecules (Winter and Faubel 2006). The second, broader, peak at higher KE (148.9 eV) accounts for all condensed phase oxygen within the probe volume, from both liquid H_2O (Winter and Faubel 2006) and citric acid. The presence of carboxyl-oxygens (two O 1s peaks separated by about 1.5 eV (Pruyne, Lee et al. 2014)) and alcohol-oxygen (Ketteler, Ashby et al. 2008) in citric acid results in the wider condensed phase O 1s contribution for the 2.5 M citric acid solution (mole fraction X = 0.060), see also Fig. S5.2 and supporting information for more details. We note that the oxygen contribution by citric acid is somewhat higher than expected from its bulk mole fraction because of the surface propensity of citric acid (see below).
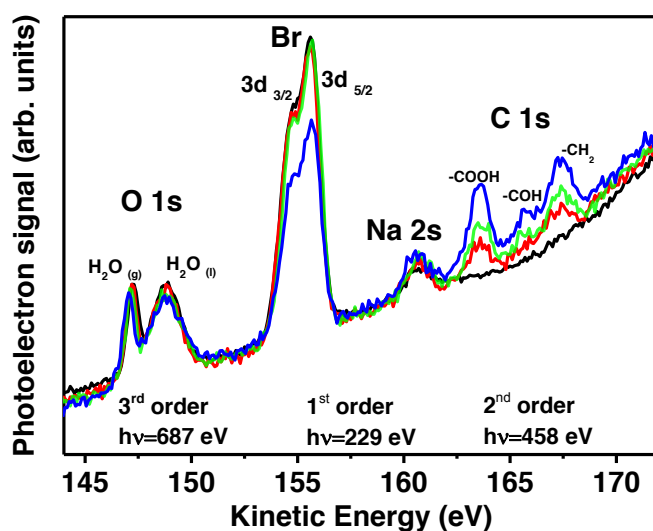
Fig. 5.3. Photoelectron spectra from aqueous solutions containing 0.12 M NaBr and varying amounts of citric acid (0, black; 0.5 M, red; 1.3 M, green; 2.5 M, blue) excited by X-rays with a nominal photon energy of 229 eV.

Spectra obtained for 0.03 M and 0.06 M NaBr over the same range of citric acid concentration are presented in Fig. S5.3 and Fig. S5.4. Normalised photoemission signals for Br, Na and C were obtained by dividing the peak areas of Br 3d, Na 2s and C 1s by the area of the condensed phase O 1s peak and multiplied by the number density of oxygen atoms per volume of liquid expected for the corresponding solutions in the bulk to take into account that this oxygen density changes slightly with increasing citric acid concentration due to the

oxygen atoms in citric acid and the changing density. This procedure assures that Br, Na and C are normalized to the volume probed at the KE with which O 1s was measured for each sample and allows us to directly compare them in a relative manner as a function of solution composition.
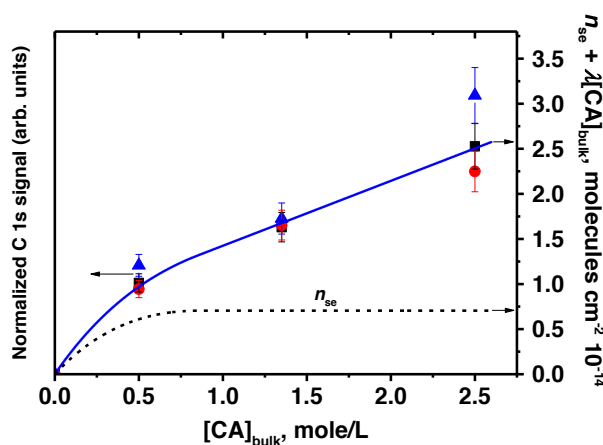

Fig. 5.4. Normalized C 1s photoemission signals as a function of citric acid concentration for three different NaBr concentrations. The blue solid line represents the simulated photoemission signal based on (E 5.11). The dashed line represents the surface excess n_{se}.

Fig. 5.4 shows the normalized C 1s PE signal as a function of the citric acid bulk concentration and for the three different NaBr concentrations. The measured C 1s PE signals do not appear to show salting effects by NaBr within error. The relative change in photoemission signal (blue line in Fig 5.4) can be described as (Pruyne, Lee et al. 2014):

$$S \propto n_{se} + \lambda \times n_{bulk} \tag{E 5.11}$$

where n_{se} is the surface excess, λ, is the electron inelastic mean free path and n_{bulk} is the bulk number density of citric acid molecules per cm^3. The surface excess (dashed line in Fig. 5.4) has been calculated from the surface tension data of Mahiuddin *et al.* (Mahiuddin, Minofar et al. 2008) The simple model of the photoemission signal expressed by (E 5.11) assumes that the surface molecules are contained in an infinitely thin layer. We calculated the relative change of the C 1s PE signal of citric acid using $\lambda \sim 1.2$ nm for the ~ 166 eV KE used (Thurmer, Seidel et al. 2013). As obvious from the shape of the surface excess in Fig. 5.4, at low concentration, the increase of the PE signal is governed by the increase in surface excess of citric acid, while at high concentration; the increase of the PE signal is dominated by the increase of the bulk contribution, which increases linearly with bulk concentration.

Fig. S5.5 in the supporting information displays the normalized Br 3d PE signals as a function of the bulk concentration, in presence and absence of citric acid. The Br 3d signal increases linearly with the bulk concentration of Br$^-$ in all cases. Citric acid has a suppressing effect on the Br signals within the probe depth at 2.5 M CA. The inelastic mean free path of the photoelectrons is approximately 1.2 nm (Thurmer, Seidel et al. 2013), which means that the measured PE signal integrates over about 3 nm, i.e., over the layered structure of Br$^-$ and sodium cations predicted by molecular dynamics simulations of the aqueous solution–air interface (Jungwirth and Tobias 2001, Ghosal, Hemminger et al. 2005). The presence of citric acid, which is a weak surfactant, is affecting the arrangement of ions near the interface in a way that the overall amount of Br$^-$ in the probed volume is decreasing. This reduction of Br$^-$ comes along with the relative increase of citric acid at the surface.

Fig. S5.6 in the supporting information shows the evolution of the normalized Na 2s signals as a function of citric acid concentration. In contrast to the behavior of Br$^-$, at least for the highest NaBr concentration, the amount of Na cations in the probed volume is increasing with increasing citric acid concentration. This trend to increase with increasing CA concentration was also apparent from the measurements at the lower NaBr concentrations, but was not significant due to the larger error. At the photon energy used in the present experiments, 229 eV, the photoionization cross section for the excitation of the Na 2s core level is relatively low (Yeh and Lindau 1985).
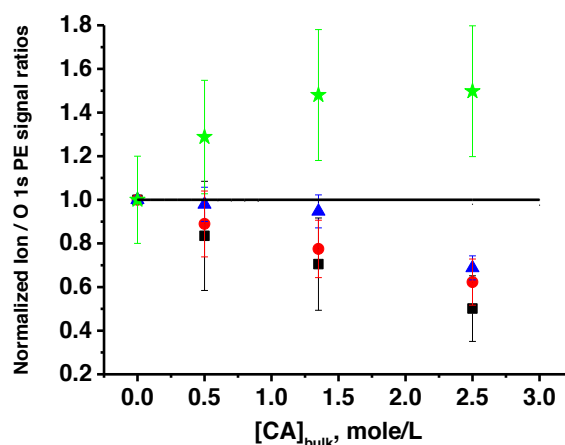

Fig. 5.5. Relative change of Br 3d and Na 2s photoemission signals as a function of citric acid concentration for Br3d, for 0.03 M (squares), 0.06 M (circles), 0.12 M (triangles) NaBr concentrations. For Na 2s, only data for 0.12 M NaBr are shown (stars). The horizontal solid line illustrates the behavior expected for the bulk solution for reference.

Fig. 5.5 summarizes the contrasting behavior of Br^- anions and sodium cations, but now the measured PE signals are plotted as relative departure of the normalized Br 3d and Na 2s PE signals from that of the neat NaBr solution with the same Br^- and sodium concentration, respectively, as a function of the citric acid concentration in the bulk. The horizontal black solid line represents baseline for bulk solution behavior.

For all 3 NaBr concentrations, with increasing citric acid concentration in the bulk, the abundance of Br^- is gradually more suppressed at the interface. The Br^- suppression was up to 40 % at 2.5 M CA. The data seem to indicate that at smaller NaBr concentrations the interfacial Br^- concentration is more effectively suppressed out of the probed volume by citric acid than at higher NaBr concentrations. On the other hand, the abundance of the sodium cations appears to increase with increasing citric acid concentration. For reasons of clarity only Na data for the 0.12 M NaBr solutions are shown (see above). The changing behavior of both ions occurs in the same concentration range of CA, where its surface excess reaches saturation. These results indicate that the presence of citric acid leads to a changing arrangement of both, the Br^- anions and the sodium cations near the aqueous solution–air interface.

Comparable conclusions have been drawn from XPS measurements of the K^+ to I^- elemental ratios on saturated KI solutions (thus at around 7 M salt concentration) in presence of butanol (Krisch, D'Auria et al. 2007). Complementary molecular dynamics (MD) simulations revealed that the propensity of I^- for the topmost surface was retained in presence of butanol, but that the K^+ ions were attracted by the alcohol headgroups and thus resided closer to the aqueous solution–air interface than in the neat salt solution (Tobias and Hemminger 2008). Such cation specific effects have been studied in detail before due to their relevance also in many other chemical and biochemical processes (Tang and Allen 2009, Okur, Kherb et al. 2013). Onorato *et al.* (Onorato, Otten et al. 2010) observed a significantly stronger resonant enhancement of the Second Harmonic Generation (SHG) spectroscopy signal of Br^- at the water–dodecanol interface than at the water–air interface. They suggested that the enhancement is due to either more Br^- ions being absorbed at the water–dodecanol interface than at the water–air interface or due to the contribution of the hydroxyl group of the dodecanol that changes the solvation shell of interfacial Br^-, which gives rise to a stronger SHG signal, or some combination of both. In addition, Huang *et al.* (Huang, Hua et al. 2013) found from the analysis of vibrational sum frequency generation (SFG) spectra in the OH

stretching region that Br⁻ had a different effect on the hydrogen bonding environment at the glycerol–air than at the aqueous solution–air interface. This was in line with their measurements of surface tension, which exhibited a smaller increase in NaBr–glycerol solutions than in the corresponding aqueous solution. Moreover, even the presence of extremely small impurity cations may have a significant effect on the interactions of sodium cations with the carboxyl group of a surfactant (Huang, Hua et al. 2013). The non-linear optical spectroscopy studies provide substantial insight into the hydrogen bonding structure as affected by the various chemical environments. Our XPS technique provides direct insight into the relative abundance of the involved solutes, in the case considered here, the contrasting behavior of sodium cations and Br⁻ anions. It is the subtle effects of the functional groups, in this case carboxyls and alcohols and their arrangement in the interfacial region that controls the relative abundance of the other solutes.

Coming back to the motivation for the XPS experiments of this study, citric acid, due to its role as a weak surfactant affects the local abundance of Br⁻ in the interfacial region. Therefore, at first glance, the origin of the reactivity enhancement with increasing citric acid concentration observed in the O_3 uptake experiments is not necessarily due to a surface reaction, since the abundance of Br⁻ at the surface is obviously decreasing. On the other hand, our experiment does not resolve the topmost layer, but, from a molecular level perspective, it provides an integral over a significant depth (about three times the electron mean free path of 1.2 nm). From the perspective of the kinetic experiments, in the context of the bulk reaction scenario, the reacto-diffusive depth for O_3 (about 5 μm) is completely insensitive to the local Ångström scale structure of Br⁻ concentration profile at the interface. In turn, if some Br⁻ would remain at the surface itself, inspite of the apparent depletion observed when integrated over the XPS probe depth, it would require a massive enhancement of the acid catalyzed mechanism at the surface itself to become rate limiting. The surface excess alone of citric acid as a proton donor may not be sufficient to drive this.

The observations in this study indicate that the concentration of Br⁻ and that of citric acid, which plays a role in the acid catalyzed oxidation of Br⁻, at the aqueous solution – air interface may be controlled by subtle effects of functional groups and their abundance in the interfacial region. These subtleties justify to some degree the apparently inconsistent implications about the presence or not of a surface reaction component in the reaction of Br⁻ with O_3 from kinetic experiments in different concentration ranges of Br⁻, in presence of

other co-solutes and different acidifying species. The reaction of O_3 with I^- solutions might be affected in a different way due to the orders of magnitude higher reactivity and thus sub-nanometer reacto-diffusive depth, bringing the probe depths of XPS and uptake kinetics into the same range.

5.5. Conclusion

The uptake kinetics of O_3 to neat NaBr solutions is consistent with bulk reaction limited uptake. In presence of citric acid, a proxy for oxidised organics in the atmosphere, bulk reaction limited uptake is still a likely scenario, where the enhanced reactivity may be explained by an acid catalyzed mechanism and possibly an increase in solubility of O_3. The uncertainty in the underlying kinetic parameters leaves room for a surface reaction. On the other hand, the photoelectron spectroscopic investigation of the same solutions by LJ-XPS demonstrate that citric acid exhibits weak surfactant behavior in line with known surface tension data and suppresses Br^- at the interface. Interestingly, the abundance of the sodium cations increased in presence of citric acid possibly through specific interactions of sodium with the alcohol or carboxylic acid groups of citric acid suggested before. These subtle effects of an organic surfactant on the changing struture at the interface do not allow to conclusively clarify the role of organics on interfacial reactivity in general.
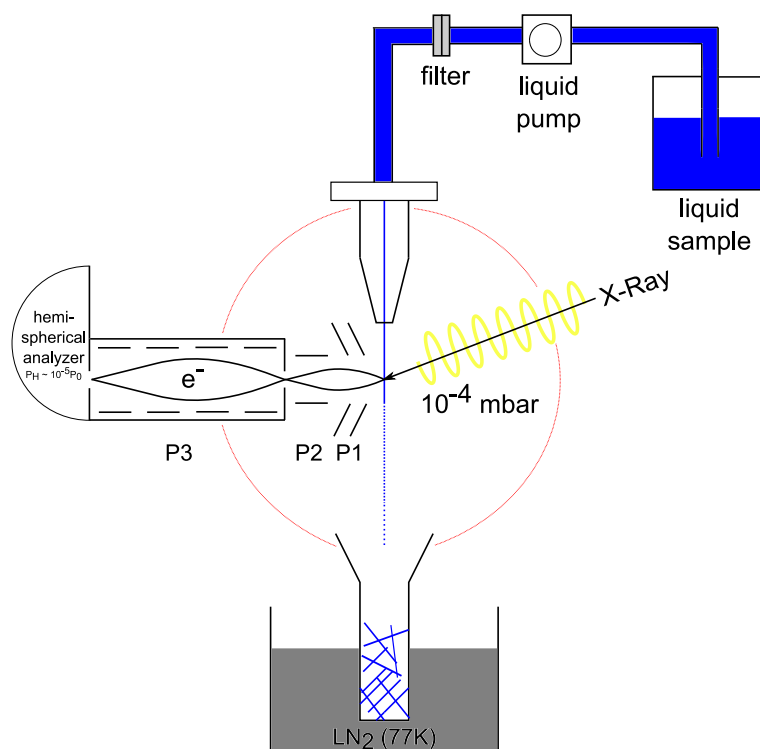
Supporting Information

Fig. S5.1. Schematic illustration of the experimental setup for photoemission studies using a liquid micro-jet. For the present experiments, a quartz nozzle, forming a liquid micro-jet with diameter of 19 um was used to conduct liquid samples into a vacuum chamber, operating at 279 K (measured immediately before entry into the ionization chamber) and a flow rate of 0.35 mL/min. The jet was adjusted to spatially overlap with the synchrotron light beam. The ejected photoelectrons from the liquid surface entered the analyzer through an orifice (skimmer) with a diameter of 500 µm to obtain photoelectron spectra.
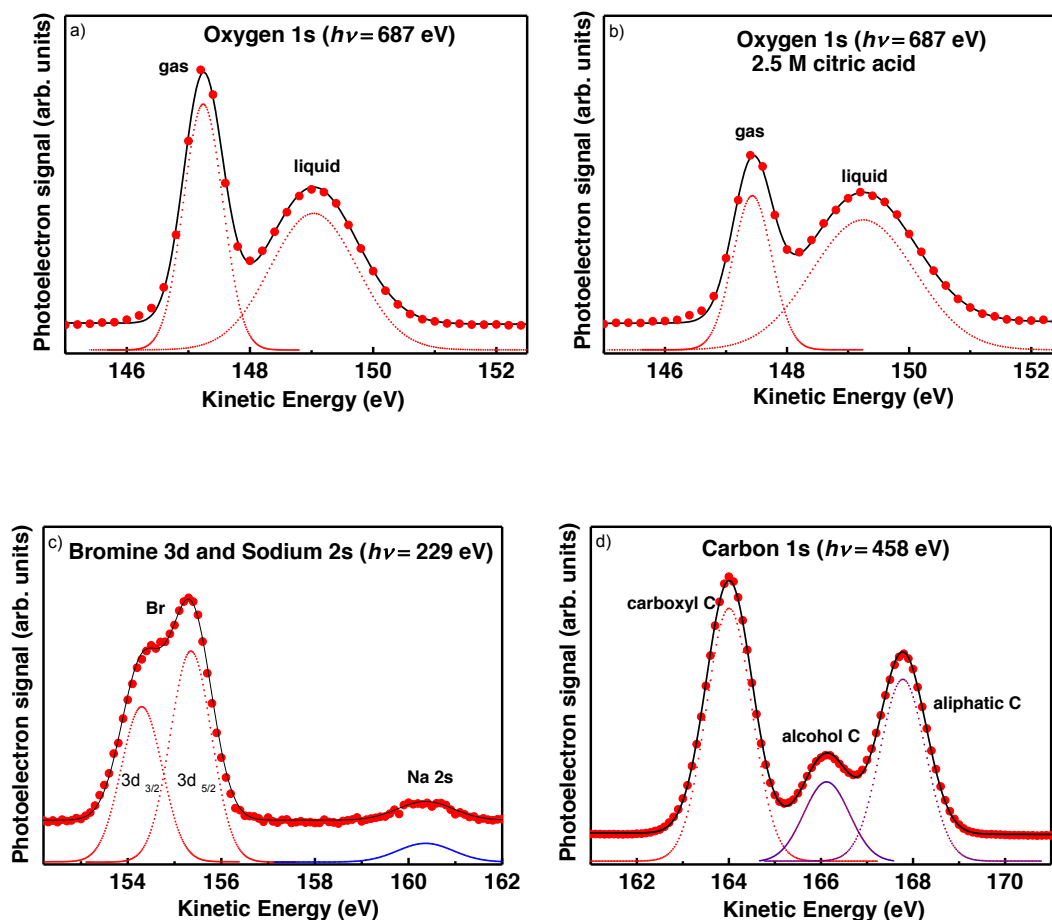
Fig. S5.2. Set of representative LJ-XPS spectra of aqueous solutions of NaBr and citric acid. Experimental data are shown by circles, fits to the data are shown by black lines, and fit components as dashed lines. (a) and (b) O 1s in absence and presence of citric acid, respectively, measured at 687 eV. (c) Br 3d and Na 2s, measured at 229 eV. (d) C 1s, measured at 458 eV. These spectra were measured with the beamline set to the corresponding photon energy, and not making use of higher order light components as in the case of those described in the main paper. The spectra were fitted using linear background subtraction and Gaussian line shapes. For Br 3d, the 3d spin-orbit split was fixed at 1.05 eV. For C 1s, the fwhm was the same for the three components assigned to carboxyl, alcohol and aliphatic carbon, respectively (Ketteler et al., 2008; Krisch et al., 2007). For O 1s, the entire O 1s envelope was fit with two Gaussian components. The one at low KE is assigned to gas phase H_2O (Winter and Faubel, 2006). The second peak at higher KE accounts for all condensed phase oxygen within the probe volume, from both H_2O and citric acid. The presence of carboxyl-oxygens (two O 1s peaks separated by about 1.5 eV) (Pruyne et al., 2014) and of alcohol-oxygen (at around 532.9 eV binding energy, Ketteler et al., 2008) in citric acid results in the wider condensed phase O 1s contribution for the 2.5 M citric acid solution (mole fraction X = 0.060).
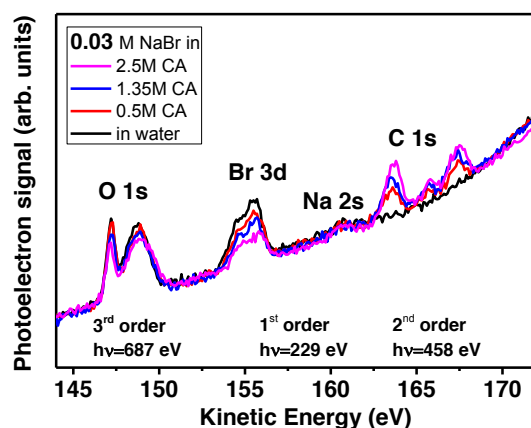
Fig. S5.3. Photoelectron spectra from aqueous solutions containing 0.03 M NaBr and varying amounts of citric acid excited by X-rays with a nominal photon energy of 229 eV, leading to photoelectron KE of ca. 155 eV deriving from Br $3d_{3/2,5/2}$ and of 160.7 eV from Na 2s. C 1s photoelectrons of KEs in the range of approximately 164–168 are excited by second order light at 458 eV. O 1s is excited by third order light at 687 eV.
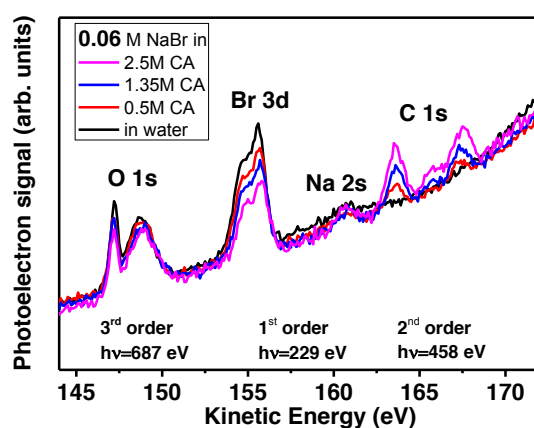

Fig. S5.4. Photoelectron spectra from aqueous solutions containing 0.06 M NaBr and varying amounts of citric acid excited by X-rays with a nominal photon energy of 229 eV, leading to photoelectron KE of ca. 155 eV deriving from Br $3d_{3/2,5/2}$ and of 160.7 eV from Na 2s. C 1s photoelectrons of KEs in the range of approximately 164–168 are excited by second order light at 458 eV. O 1s is excited by third order light at 687 eV.
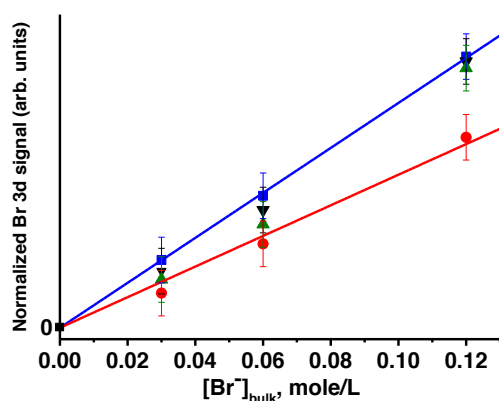
Fig. S5.5. Normalized Br 3d photoemission signals as a function of NaBr bulk concentration for 0 M (blue squares), 0.5 M (green upward triangles), 1.35 M (black downward triangles) and 2.5 M CA (red circles). The lines are linear fits to the measured Br 3d PE signal for the neat NaBr (blue) and the NaBr in 2.5 M citric acid (red) solutions, respectively.
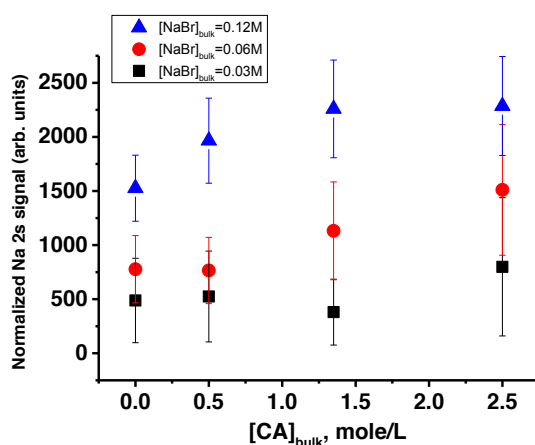

Fig. S5.6. Normalised Na 2s photoemission signals as a function of the citric acid concentration and for 0.03 M (black squares), 0.06 M (red circles), 0.12 M (blue triangles) NaBr concentrations.

Acknowledgments

References

Ammann, M., R. A. Cox, J. N. Crowley, M. E. Jenkin, A. Mellouki, M. J. Rossi, J. Troe and T. J. Wallington (2013). "Evaluated kinetic and photochemical data for atmospheric chemistry: Volume VI - heterogeneous reactions with liquid substrates." Atmospheric Chemistry and Physics **13**(16): 8045-8228.

Bin, A. K. (2006). "Ozone solubility in liquids." Ozone-Science & Engineering **28**(2): 67-75.

Brown, M. A., A. Beloqui Redondo, M. Sterrer, B. Winter, G. Pacchioni, Z. Abbas and J. A. van Bokhoven (2013). "Measure of Surface Potential at the Aqueous-Oxide Nanoparticle Interface by XPS from a Liquid Microjet." Nano Letters **13**: 5403-5407.

Brown, M. A., M. Faubel and B. Winter (2009). "X-Ray photo- and resonant Auger-electron spectroscopy studies of liquid water and aqueous solutions." Annual Reports Section "C" (Physical Chemistry) **105**(0): 174-212.

Brown, M. A., A. B. Redondo, I. Jordan, N. Duyckaerts, M.-T. Lee, M. Ammann, F. Nolting, A. Kleibert, T. Huthwelker, J.-P. Maechler, M. Birrer, J. Honegger, R. Wetter, H. J. Woerner and J. A. van Bokhoven (2013). "A new endstation at the Swiss Light Source for ultraviolet photoelectron spectroscopy, X-ray photoelectron spectroscopy, and X-ray absorption spectroscopy measurements of liquid solutions." Review of Scientific Instruments **84**(7).

Carpenter, L. J., S. M. MacDonald, M. D. Shaw, R. Kumar, R. W. Saunders, R. Parthipan, J. Wilson and J. M. C. Plane (2013). "Atmospheric iodine levels influenced by sea surface emissions of inorganic iodine." Nature Geoscience **6**(2): 108-111.

Chameides, W. L. (1984). "THE PHOTOCHEMISTRY OF A REMOTE MARINE STRATIFORM CLOUD." Journal of Geophysical Research-Atmospheres **89**(ND3): 4739-4755.

Clifford, D. and D. J. Donaldson (2007). "Direct experimental evidence for a heterogeneous reaction of ozone with bromide at the air-aqueous interface." Journal of Physical Chemistry A **111**(39): 9809-9814.

Donaldson, D. J. and C. George (2012). "Sea-Surface Chemistry and Its Impact on the Marine Boundary Layer." Environmental Science & Technology **46**(19): 10385-10389.

Faubel, M., B. Steiner and J. P. Toennies (1997). "Photoelectron spectroscopy of liquid water, some alcohols, and pure nonane in free micro jets." Journal of Chemical Physics **106**(22): 9013-9031.

Faust, J. A., L. P. Dempsey and G. M. Nathanson (2013). "Surfactant-Promoted Reactions of Cl_2 and Br_2 with Br^- in Glycerol." Journal of Physical Chemistry B **117**(41): 12602-12612.

Flechsig, U., F. Nolting, A. F. Rodriguez, J. Krempasky, C. Quitmann, T. Schmidt, S. Spielmann and D. Zimoch (2010). "Performance measurements at the SLS SIM beamline." AIP Conference Proceedings **1234**: 319-322.

Fono, L. J. and D. L. Sedlak (2007). "A simple method for the measurement of organic iodine in wastewater and surface water." Water Research **41**(7): 1580-1586.

Foster, K. L., R. A. Plastridge, J. W. Bottenheim, P. B. Shepson, B. J. Finlayson-Pitts and C. W. Spicer (2001). "The role of Br_2 and BrCl in surface ozone destruction at polar sunrise." Science **291**(5503): 471-474.

Garland, J. A., A. W. Elzerman and S. A. Penkett (1980). "THE MECHANISM FOR DRY DEPOSITION OF OZONE TO SEAWATER SURFACES." Journal of Geophysical Research-Oceans and Atmospheres **85**(NC12): 7488-7492.

Ghosal, S., M. A. Brown, H. Bluhm, M. J. Krisch, M. Salmeron, P. Jungwirth and J. C. Hemminger (2008). "Ion Partitioning at the Liquid/Vapor Interface of a Multicomponent Alkali Halide Solution: A Model for Aqueous Sea Salt Aerosols." Journal of Physical Chemistry A **112**(48): 12378-12384.

Ghosal, S., J. C. Hemminger, H. Bluhm, B. S. Mun, E. L. D. Hebenstreit, G. Ketteler, D. F. Ogletree, F. G. Requejo and M. Salmeron (2005). "Electron spectroscopy of aqueous solution interfaces reveals surface enhancement of halides." Science **307**(5709): 563-566.

Haag, W. R. and J. Hoigne (1983). "Ozonation of Bromide-Containing Waters - Kinetics of Formation of Hypobromous Acid and Bromate." Environmental Science & Technology **17**(5): 261-267.

Hanson, D. R., A. R. Ravishankara and S. Solomon (1994). "HETEROGENEOUS REACTIONS IN SULFURIC-ACID AEROSOLS - A FRAMEWORK FOR MODEL-CALCULATIONS." Journal of Geophysical Research-Atmospheres **99**(D2): 3615-3629.

Hu, J. H., Q. Shi, P. Davidovits, D. R. Worsnop, M. S. Zahniser and C. E. Kolb (1995). "REACTIVE UPTAKE OF CL2(G) AND BR2(G) BY AQUEOUS SURFACES AS A FUNCTION OF BR^- AND I^- ION CONCENTRATION - THE EFFECT OF CHEMICAL-REACTION AT THE INTERFACE." Journal of Physical Chemistry **99**(21): 8768-8776.

Huang, Z., W. Hua, D. Verreault and H. C. Allen (2013). "Influence of Salt Purity on Na+ and Palmitic Acid Interactions." Journal of Physical Chemistry A **117**(50): 13412-13418.

Huang, Z., W. Hua, D. Verreault and H. C. Allen (2013). "Salty Glycerol versus Salty Water Surface Organization: Bromide and Iodide Surface Propensities." Journal of Physical Chemistry A **117**(29): 6346-6353.

Hunt, S. W., M. Roeselova, W. Wang, L. M. Wingen, E. M. Knipping, D. J. Tobias, D. Dabdub and B. J. Finlayson-Pitts (2004). "Formation of molecular bromine from the reaction of ozone with deliquesced NaBr aerosol: Evidence for interface chemistry." Journal of Physical Chemistry A **108**(52): 11559-11572.

Johnson, P. N. and R. A. Davis (1996). "Diffusivity of ozone in water." Journal of Chemical and Engineering Data **41**(6): 1485-1487.

Jungwirth, P. and D. J. Tobias (2001). "Molecular structure of salt solutions: A new view of the interface with implications for heterogeneous atmospheric chemistry." Journal of Physical Chemistry B **105**(43): 10468-10472.

Jungwirth, P. and D. J. Tobias (2002). "Ions at the air/water interface." Journal of Physical Chemistry B **106**(25): 6361-6373.

Jungwirth, P. and D. J. Tobias (2006). "Specific Ion Effects at the Air/Water Interface." Chem. Rev. **106**(4): 1259-1281.

Kanakidou, M., J. H. Seinfeld, S. N. Pandis, I. Barnes, F. J. Dentener, M. C. Facchini, R. Van Dingenen, B. Ervens, A. Nenes, C. J. Nielsen, E. Swietlicki, J. P. Putaud, Y. Balkanski, S. Fuzzi, J. Horth, G. K. Moortgat, R. Winterhalter, C. E. L. Myhre, K. Tsigaridis, E. Vignati, E. G. Stephanou and J. Wilson (2005). "Organic aerosol and global climate modelling: a review." Atmospheric Chemistry and Physics **5**: 1053-1123.

Ketteler, G., P. Ashby, B. S. Mun, I. Ratera, H. Bluhm, B. Kasemo and M. Salmeron (2008). "In situ photoelectron spectroscopy study of water adsorption on model biomaterial surfaces." Journal of Physics-Condensed Matter **20**(18).

Khoshkbarchi, M. K. and J. H. Vera (1996). "Measurement and correlation of ion activity in aqueous single electrolyte solutions." Aiche Journal **42**(1): 249-258.

Knopf, D. A., L. M. Cosman, P. Mousavi, S. Mokamati and A. K. Bertram (2007). "A novel flow reactor for studying reactions on liquid surfaces coated by organic monolayers: Methods, validation, and initial results." Journal of Physical Chemistry A **111**(43): 11021-11032.

Krisch, M. J., R. D'Auria, M. A. Brown, D. J. Tobias, J. C. Hemminger, M. Ammann, D. E. Starr and H. Bluhm (2007). "The effect of an organic surfactant on the liquid-vapor interface of an electrolyte solution." Journal of Physical Chemistry C **111**(36): 13497-13509.

Laguerie, C., M. Aubry and J. P. Couderc (1976). "SOME PHYSICOCHEMICAL DATA ON MONOHYDRATE CITRIC-ACID SOLUTIONS IN WATER - SOLUBILITY, DENSITY, VISCOSITY, DIFFUSIVITY, PH OF STANDARD SOLUTION, AND REFRACTIVE-INDEX." Journal of Chemical and Engineering Data **21**(1): 85-87.

Lienhard, D. M., D. L. Bones, A. Zuend, U. K. Krieger, J. P. Reid and T. Peter (2012). "Measurements of Thermodynamic and Optical Properties of Selected Aqueous Organic and Organic-Inorganic Mixtures of Atmospheric Relevance." Journal of Physical Chemistry A **116**(40): 9954-9968.

Lienhard, D. M., A. J. Huisman, D. L. Bones, Y.-F. Te, B. P. Luo, U. K. Krieger and J. P. Reid (2014). "Retrieving the translational diffusion coefficient of water from experiments on single levitated aerosol droplets." Physical Chemistry Chemical Physics **16**(31): 16677-16683.

Liu, Q., L. M. Schurter, C. E. Muller, S. Aloisio, J. S. Francisco and D. W. Margerum (2001). "Kinetics and mechanisms of aqueous ozone reactions with bromide, sulfite, hydrogen sulfite, iodide, and nitrite ions." Inorganic Chemistry **40**(17): 4436-4442.

Mahiuddin, S., B. Minofar, J. M. Borah, M. R. Das and P. Jungwirth (2008). "Propensies of oxalic, citric, succinic, and maleic acids for the aqueous solution/vapour interface: Surface tension measurements and molecular dynamics simulations." Chemical Physics Letters **462**(4-6): 217-221.

Morris, J. R. (2013). "Developing a Molecular-Level Understanding of Organic Chemistry and Physics at the Gas-Surface Interface." Journal of Physical Chemistry Letters **4**(23): 4055-4057.

O'Dowd, C. D., M. C. Facchini, F. Cavalli, D. Ceburnis, M. Mircea, S. Decesari, S. Fuzzi, Y. J. Yoon and J. P. Putaud (2004). "Biogenically driven organic contribution to marine aerosol." Nature **431**(7009): 676-680.

Okur, H. I., J. Kherb and P. S. Cremer (2013). "Cations Bind Only Weakly to Amides in Aqueous Solutions." Journal of the American Chemical Society **135**(13): 5062-5067.

Oldridge, N. W. and J. P. D. Abbatt (2011). "Formation of Gas-Phase Bromine from Interaction of Ozone with Frozen and Liquid NaCl/NaBr Solutions: Quantitative Separation of Surficial Chemistry from Bulk-Phase Reaction." Journal of Physical Chemistry A **115**(12): 2590-2598.

Onorato, R. M., D. E. Otten and R. J. Saykally (2010). "Measurement of Bromide Ion Affinities for the Air/Water and Dodecanol/Water Interfaces at Molar Concentrations by UV Second Harmonic Generation Spectroscopy." Journal of Physical Chemistry C **114**(32): 13746-13751.

Prather, K. A., T. H. Bertram, V. H. Grassian, G. B. Deane, M. D. Stokes, P. J. DeMott, L. I. Aluwihare, B. P. Palenik, F. Azam, J. H. Seinfeld, R. C. Moffet, M. J. Molina, C. D. Cappa, F. M. Geiger, G. C. Roberts, L. M. Russell, A. P. Ault, J. Baltrusaitis, D. B. Collins, C. E. Corrigan, L. A. Cuadra-Rodriguez, C. J. Ebben, S. D. Forestieri, T. L. Guasco, S. P. Hersey, M. J. Kim, W. F. Lambert, R. L. Modini, W. Mui, B. E. Pedler, M. J. Ruppel, O. S. Ryder, N. G. Schoepp, R. C. Sullivan and D. Zhao (2013). "Bringing the ocean into the laboratory to probe the chemical complexity of sea spray aerosol." Proceedings of the National Academy of Sciences of the United States of America **110**(19): 7550-7555.

Pruyne, J. G., M.-T. Lee, C. Fábri, A. Beloqui Redondo, A. Kleibert, M. Ammann, M. A. Brown and M. J. Krisch (2014). "Liquid–Vapor Interface of Formic Acid Solutions in Salt Water: A Comparison of Macroscopic Surface Tension and Microscopic in Situ X-ray Photoelectron Spectroscopy Measurements." The Journal of Physical Chemistry C.

Rouviere, A. and M. Ammann (2010). "The effect of fatty acid surfactants on the uptake of ozone to aqueous halogenide particles." Atmospheric Chemistry and Physics **10**(23): 11489-11500.

Rouviere, A., Y. Sosedova and M. Ammann (2010). "Uptake of Ozone to Deliquesced KI and Mixed KI/NaCl Aerosol Particles." Journal of Physical Chemistry A **114**(26): 7085-7093.

Saiz-Lopez, A., J. F. Lamarque, D. E. Kinnison, S. Tilmes, C. Ordonez, J. J. Orlando, A. J. Conley, J. M. C. Plane, A. S. Mahajan, G. S. Santos, E. L. Atlas, D. R. Blake, S. P. Sander, S. Schauffler, A. M. Thompson and G. Brasseur (2012). "Estimating the climate significance of halogen-driven ozone loss in the tropical marine troposphere." Atmospheric Chemistry and Physics **12**(9): 3939-3949.

Simpson, W. R., R. von Glasow, K. Riedel, P. Anderson, P. Ariya, J. Bottenheim, J. Burrows, L. J. Carpenter, U. Friess, M. E. Goodsite, D. Heard, M. Hutterli, H. W. Jacobi, L. Kaleschke, B. Neff, J. Plane, U. Platt, A. Richter, H. Roscoe, R. Sander, P. Shepson, J. Sodeau, A. Steffen, T. Wagner and E. Wolff (2007). "Halogens and their role in polar boundary-layer ozone depletion." Atmospheric Chemistry and Physics **7**(16): 4375-4418.

Tang, C. Y. and H. C. Allen (2009). "Ionic Binding of Na+ versus K+ to the Carboxylic Acid Headgroup of Palmitic Acid Monolayers Studied by Vibrational Sum Frequency Generation Spectroscopy." Journal of Physical Chemistry A **113**(26): 7383-7393.

Thurmer, S., R. Seidel, M. Faubel, W. Eberhardt, J. C. Hemminger, S. E. Bradforth and B. Winter (2013). "Photoelectron Angular Distributions from Liquid Water: Effects of Electron Scattering." Physical Review Letters **111**(17).

Tobias, D. J. and J. C. Hemminger (2008). "Chemistry - Getting specific about specific ion effects." Science **319**(5867): 1197-1198.

Varga, Z., G. Kiss and H. C. Hansson (2007). "Modelling the cloud condensation nucleus activity of organic acids on the basis of surface tension and osmolality measurements." Atmospheric Chemistry and Physics **7**(17): 4601-4611.

Vignati, E., M. C. Facchini, M. Rinaldi, C. Scannell, D. Ceburnis, J. Sciare, M. Kanakidou, S. Myriokefalitakis, F. Dentener and C. D. O'Dowd (2010). "Global scale emission and distribution of sea-spray aerosol: Sea-salt and organic enrichment." Atmospheric Environment **44**(5): 670-677.

Winter, B. (2009). "Liquid microjet for photoelectron spectroscopy." Nuclear Instruments & Methods in Physics Research Section a-Accelerators Spectrometers Detectors and Associated Equipment **601**(1-2): 139-150.

Winter, B. and M. Faubel (2006). "Photoemission from liquid aqueous solutions." Chemical Reviews **106**(4): 1176-1211.

Yeh, J. J. and I. Lindau (1985). "ATOMIC SUBSHELL PHOTOIONIZATION CROSS-SECTIONS AND ASYMMETRY PARAMETERS - 1 LESS-THAN-OR-EQUAL-TO Z LESS-THAN-OR-EQUAL-TO 103." Atomic Data and Nuclear Data Tables **32**(1): 1-155.

Zardini, A. A., S. Sjogren, C. Marcolli, U. K. Krieger, M. Gysel, E. Weingartner, U. Baltensperger and T. Peter (2008). "A combined particle trap/HTDMA hygroscopicity study of mixed inorganic/organic aerosol particles." Atmospheric Chemistry and Physics **8**(18): 5589-5601.

Chapter 6

6. Contrasting the effect of an alcohol and a carboxylic acid surfactant on the ion distribution at the aqueous solution - air interface

Ming-Tao Lee, Fabrizio Orlando, Morteza Khabiri, Shunsuke Kato, Matthew A. Brown, Andreas Türler, Martina Roeselová, Markus Ammann

Manuscript in preparation

6.1. Abstract

We use in situ X-ray photoelectron spectroscopy with a micro liquid jet to obtain chemical composition information at the liquid−vapor interface from mixed aqueous solutions containing bromide/iodide and organic surfactants. Core level spectra of Br 3d, Na 2s, C 1s and O 1s at about 160 eV kinetic; core level spectra of I 4d at about 400 eV kinetic energy will be compared for solutions with 1-butanol and butyric acid as a function of organic concentration. We observe that butyric acid pushes the anion, bromide, and the cation, sodium away from the interface more than 1-butanol does in the region of the liquid interface. Similar to the case of the bromide solutions, we observe that butyric acid displaces the anion, iodide, away from the interface more strongly than 1-butanol. Molecular dynamics simulations (MD) of 1-butanol and butyric acid in aqueous sodium halide solutions are used to develop a detailed understanding of ternary solutions i.e. ion-organics-water interactions in the interfacial region.

6.2. Introduction

The ozone budget in the marine boundary layer has remained a hot topic in the atmospheric chemistry community (Abbatt, Thomas et al. 2012). The oxidation of bromide (Br^-) and iodide (I^-) at the aqueous liquid−vapor interface by atmospheric oxidants, such as ozone (O_3) or hydroxyl OH radicals, has been found critical in initiating halogen cycling reactions in marine air and particularly important for the global budgets of bromine and iodine and also the O_3 budget (Carpenter, MacDonald et al. 2013). Recently, the fact that the ocean surface carries a layer consisting of a wealth of organic compounds deriving from marine biota has received a lot of attention, and the details on the impact of these organics on marine halogen chemistry has remained unclear (Donaldson and George 2012). The halide oxidation reactions mentioned above have been suggested to be enhanced at the aqueous liquid−vapor interface (Hunt, Roeselova et al. 2004, Clifford and Donaldson 2007, Oldridge and Abbatt 2011) possibly induced by the specific molecular scale profile halide ions exhibit at this interface. These profiles have been confirmed by both experiment (Ghosal, Hemminger et al. 2005, Brown, D'Auria et al. 2008) and theory (Jungwirth and Tobias 2001, Dang and Chang 2002, Chang and Dang 2006, Jungwirth and Tobias 2006, Petersen and Saykally 2006, Ishiyama and Morita 2007, Horinek, Herz et al. 2009, Caleman, Hub et al. 2011, Vazdar, Pluharova et al. 2012). Insight into the behavior of the halide ions at mixed organic/aqueous

liquid surfaces is, therefore, crucial for understanding the chemistry of marine aerosols and brines associated with arctic sea ice or snow packs, which are more complex than just halide solutions. Understanding the feedbacks mechanisms between physical conditions and chemical composition are important for assessing the release of halogen compounds from the ocean surface, snowpacks or sea spray aerosol particles.

Earlier, X-ray photoelectron spectroscopy experiments (XPS) have provided first indications for the entanglement of I^- anions, K^+ cations and the surfactant headgroup (alcohol) (Krisch, D'Auria et al. 2007). XPS provides important information for this purpose via its high surface sensitivity, typically in the nm range, which arises due to the short inelastic mean free path (IMFP) of electrons in condensed matter (Seah and Dench 1979), and in aqueous solution (Ottosson, Faubel et al. 2010). Our recent development of the near-ambient pressure photoelectron spectroscopy endstation (NAPP) enables electron spectroscopy of volatile liquids by using the liquid micro-jet (LJ) technique (Brown, Faubel et al. 2009, Winter 2009, Brown, Redondo et al. 2013). The liquid jet provides a continuously renewed interface that is devoid of carbonaceous impurities and of radiation damage that have previously been reported for similar systems for static deliquesced solutions (Ghosal, Hemminger et al. 2005, Krisch, D'Auria et al. 2007, Ghosal, Brown et al. 2008). Therefore, LJ-XPS is the ideal tool for furthering our understanding of halide ions co-adsorbed with organic matter at the liquid−vapor interface.

In a first study of the surface composition, combining kinetic experiments of the oxidation of Br^- by O_3 and LJ-XPS, we have made a attempt to assess the impact of organics on the prevalence of Br^- at liquid−vapor interface and on the heterogeneous chemistry of them. In that study we chose citric acid as a representative of highly oxidized organic compounds in the atmosphere. Together with other studies (Tobias and Hemminger 2008, Tang and Allen 2009, Onorato, Otten et al. 2010, Huang, Hua et al. 2013, Huang, Hua et al. 2013, Okur, Kherb et al. 2013), it has become apparent that subtle effects control the impact of organic species on the ion profiles. While Br^- was observed to be displaced from the interface by citric acid, sodium seemed to be rather attracted further towards the interface in presence of citric acid, which has three carboxylic groups and one alcohol group (Lee, Brown et al. 2015). Therefore, a more systematic approach into the interplay of both ions with different functional groups at the interface is warranted. In this study, we address the difference between an alcohol and a carboxylic acid headgroup of the surfactant on the distribution of

Na$^+$, Br$^-$, and I$^-$ at the interface within the probe depth using LJ-XPS (Brown, Redondo et al. 2013). The surfactants chosen were 1-butanol and butyric acid, which exhibit well characterized surface excess for the concentration range used in our experiments. In addition to LJ-XPS measurements, we report classical MD simulations employing polarizable force fields to elucidate specific cation effects on the interfacial composition of sodium Br$^-$ and sodium I$^-$ solutions. Such MD simulations were instrumental in assessing the propensity of halide ions for the interface (Jungwirth and Tobias 2001, Dang and Chang 2002, Chang and Dang 2006, Jungwirth and Tobias 2006, Petersen and Saykally 2006, Ishiyama and Morita 2007, Horinek, Herz et al. 2009, Caleman, Hub et al. 2011, Vazdar, Pluharova et al. 2012) and provide useful insights into the relative effects of surfactants in this study.

6.3. Methods

6.3.1. Liquid microjet XPS

We made use of the NAPP endstation with the liquid microjet setup at the Surfaces/Interfaces: Microscopy (SIM) beamline of the Swiss Light Source (SLS) at Paul Scherrer Institute (PSI) (Flechsig, Nolting et al. 2010). The electron analyzer uses a three-stage differentially pumped electrostatic lens system and a hemispherical analyzer to collect photoelectrons from samples at chamber pressures up to a few mbar. For the present experiments, a quartz nozzle, forming a liquid microjet with a diameter of 26 μm, was used to deliver a liquid sample into the vacuum chamber. The liquid was cooled to 279 K immediately before entry into the ionization chamber and a flow rate of 0.35 mL/min was used. The chamber pressure with the jet running was between 1.0×10^{-3} and 1.0×10^{-4} mbar. The photoelectrons from the liquid surface entered the analyzer through an orifice (skimmer) with a diameter of 500 μm. The working distance between the liquid jet and the detector orifice was 500 μm.

A complete description of the equilibrated nature of a liquid microjet under the conditions of photoemission experiments has previously been given in the literature (Faubel, Steiner et al. 1997, Brown, Faubel et al. 2009). In the context of this study, it is important that the surface active organic species (1-butanol and butyric acid) can reach equilibrium concentration at the surface until the jet is hit by the X-ray beam (Faubel, Steiner et al. 1997, Pruyne, Lee et al. 2014, Lee, Brown et al. 2015).

For bromide containing solutions, the primary photon energy for the detection of Br 3d and Na 2s was set to 229 eV, resulting in a photoelectron KE of about 155 eV and 160 eV,

respectively. We made use of the around 10% of photon flux associated with 2nd order light, which simultaneously passes the monochromator with photon energies of 458 eV, to ionize the C 1s orbital for a KE of 163-168 eV. The even smaller amounts of 3rd order light at 687 eV were used to excite the O 1s orbital for a KE of 148.9 eV for liquid water. This procedure allowed determining photoemission signals for each element within one sweep of the electron analyzer in a relatively narrow kinetic energy range. 50 sweeps were averaged to create one spectrum.

For spectroscopic reasons, this was not possible with iodide solutions. In that case, we have measured the sodium 2s and iodine 4d PE at a KE of around 382 and 395 eV, respectively, with a primary photon energy of 450 eV, and oxygen 1s at around 400 eV KE excited by 2nd order light at 900 eV. This allowed us obtaining iodide and sodium concentrations as a function of 1-butanol and butyric acid concentrations within the probe depth of around 1.5 nm (Thurmer, Seidel et al. 2013). The core level carbon 1s was assessed from separate spectra measured at the same photon energy with KE around 150 eV. 50 sweeps were averaged to create one spectrum.

A constant concentration (0.12 mole/L) of sodium bromide (NaBr, BioXtra ≥99.0%, Sigma-Aldrich) and sodium iodide (NaI, ACS reagent ≥99.5%, Sigma-Aldrich) in 0.001, 0.002, 0.004, and 0.008 mole fraction 1-butanol (1-BuOH, 99.9%, Sigma-Aldrich) and butyric acid (BuOOH, ≥99+%, Alfa Aesar), respectively, were prepared for analysis. The solutions were prepared by adding stock solutions of NaBr and the organics to Milli-Q water (Millipore, 18.2 MΩ cm at 25 °C).

6.3.2. MD simulations

Classical molecular dynamics simulations were employed to study interactions of NaBr and NaI with 1-BuOH and BuOOH in solution. A slab geometry was constructed in which two monolayers, each containing 116 1-BuOH/BuOOH molecules (Fig. 6.1), were placed at the two air/liquid interfaces of a water slab, with the -C-OH/-C-OOH head groups immersed in water. The water slab was placed in the center of a prismatic simulation box, elongated along the interface normal in order to create a vacuum layer over both monolayers. Standard 3D periodic boundary conditions were applied. First, a pure monolayer system was simulated to obtain an equilibrated monolayer at lateral compressions by NVT (Canonical ensemble) simulations with 0.12 M of NaBr or NaI ionic solutions. Parameters for I^- and Br^- anions were taken from the force field introduced by Horinek et al. (Horinek, Mamatkulov et al.

2009). Both systems were constructed with 4.5 nm size in X and Y, which represents a fairly relaxed monolayer. In all cases, the size of the system in Z direction was taken as 15 nm. Following short energy minimization, a 120 ns MD run was performed for scaled systems equilibration from which the last 20 ns were used for analysis. Results obtained for both monolayers were averaged during the analysis of simulation trajectories. MD simulations were performed employing the empirical OPLS (Optimized Potentials for Liquid Simulations) all-atom force field (Jorgensen, Maxwell et al. 1996) for the organic molecules and the SPC/E model of water (Berendsen, Grigera et al. 1987). The lengths of bonds were constrained using the SETTLE/LINCS algorithms (Hess, Bekker et al. 1997). The short-range interaction cutoff of 10 Å was employed, while the long-range electrostatic energy was accounted for using the PME (Particle mesh Ewald) scheme. Temperature in all simulations was set to 310 K and controlled using the Nosé–Hoover thermostat with a coupling constant of 1 ps (Nose 1984, Hoover 1985). Each simulation was carried out at a constant volume and a constant lateral cross-section of the simulation box. Equations of motion were integrated using the leap-frog algorithm with a time step of 2 fs. MD simulations were performed using the GROMACS 4.6.7 program package (Hess, Kutzner et al. 2008). The density profile for different groups was calculated based on particle mass at a certain coordinate.
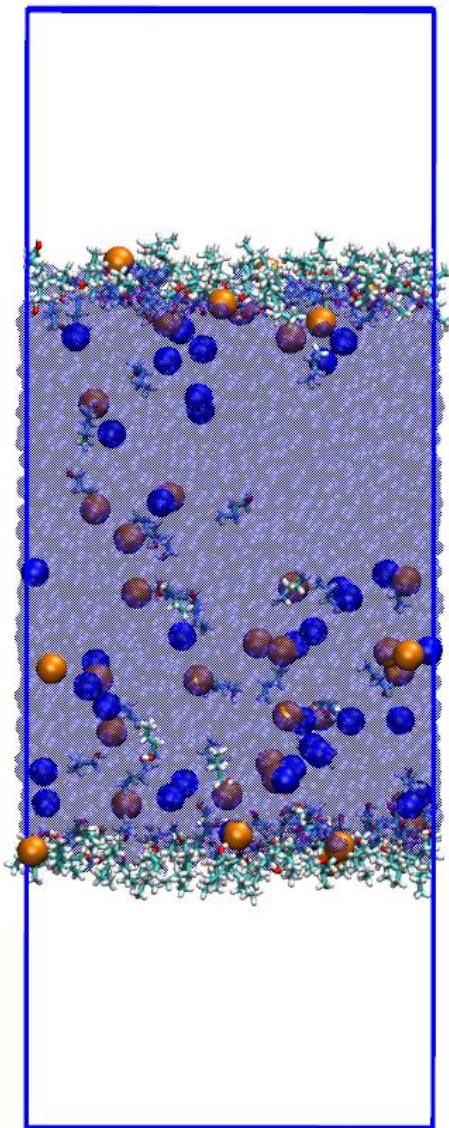
Fig. 6.1. Last snapshot of the simulation models (120 ns) for 1-BuOH in NaI solution. Water molecules are shown as transparent in light blue, Na$^+$ ions in dark blue, I$^-$ ions in orange and 1-BuOH molecules which are shown by their ball-and-stick model representations.

6.4. Results and discussion

6.4.1. Liquid microjet XPS

Fig. 6.2 (a, b) shows example of combined O 1s, Br 3d, Na 2s, and C 1s photoelectron spectra from 0.12 M NaBr aqueous solutions as a function of the 1-BuOH (a) and the BuOOH (b) concentration (in the mole fraction of 0 and 0.008) taken at a nominal photon energy of 229 eV and making use of the higher order light components to obtain C 1s and O 1s in the same kinetic energy (KE) window as described in the previous chapter. This obviously goes at the expense of signal-to-noise ratio for O 1s and C 1s, but has the advantage to provide

photoemission signals for all four elements within one sweep of the electron analyzer and thereby allows keeping track of variations induced by small movements of the liquid jet.
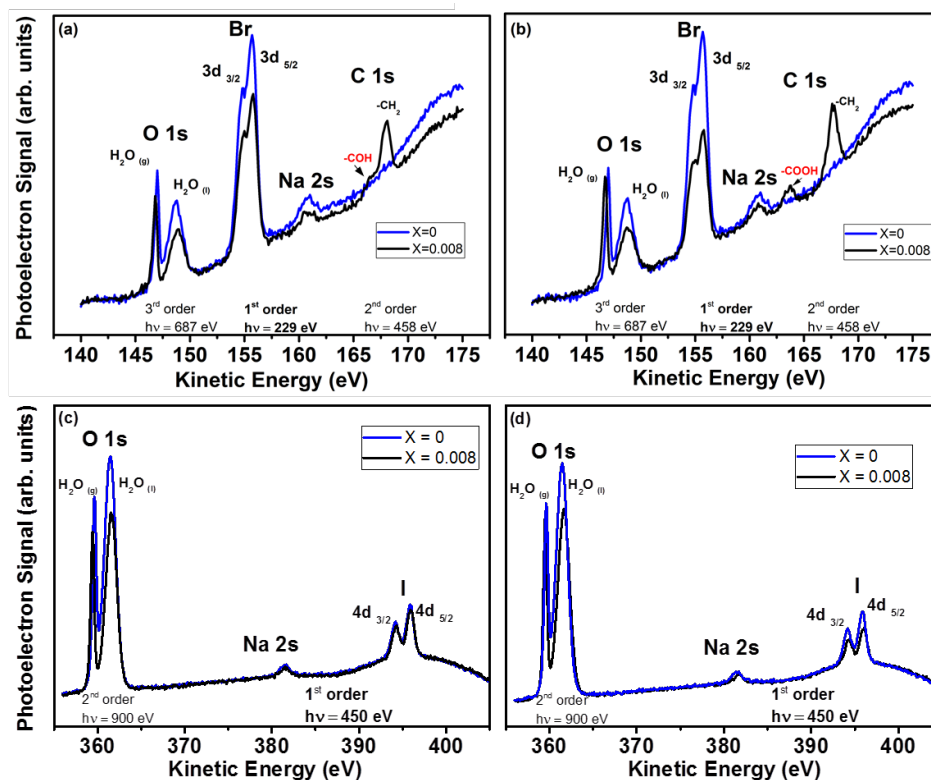
Fig. 6.2. (a) Examples of photoelectron spectra from aqueous solutions containing 0.12 M NaBr and varying amounts of 1-BuOH (0, blue; X=0.001, black, where X is the mole fraction of organics within water) excited by X-rays with a nominal photon energy of 229 eV. (b) The same experiments as in (a) but with BuOOH. (c) Examples of photoelectron spectra from aqueous solutions containing 0.12 M NaI and varying amounts of 1-BuOH (0, blue; X=0.008, black) excited by X-rays with a nominal photon energy of 450 eV. (d) The same experiments as in (c) but now with BuOOH.

In Fig. S5.2. higher signal-to-noise spectra obtained separately for each core level region measured with standard first order light along with the details of how the peaks were fit are shown. The spin-orbit splitted bromine levels Br $3d_{3/2,5/2}$ appear at a photoelectron KE of about 155 eV. The Na 2s level is observed at 160.7 eV KE. The C 1s signal, excited by photons at around 458 eV, appears in the spectrum at photoelectron KEs of 164.4 eV (carboxyl C of BuOOH), 166.6 eV (alcohol C from 1-BuOH) and 168.2 eV (aliphatic C for both organics) (Krisch, D'Auria et al. 2007, Ketteler, Ashby et al. 2008). The O 1s level was excited at a photon energy of 687 eV. The lower KE peak (147.1 eV) with smaller full width at half maximum (FWHM) is assigned to gas phase water molecules (Brown, Vila et al. 2012). Within the broader condensed phase O 1s peak two components should be present:

oxygen present in solvent water at ~55 M and oxygen present in the functional group of the two organic solutes at 0.5 M. Due to the strong overlap of these signals, we are unable to resolve the individual contributions and fitted the condensed phase O 1s region with a single component (as has been described in *Chapter 4*). Apparently, the Br 3d and Na 2s peaks were found to decrease with the presence of organics, while the C 1s peaks were found to increase with the presence of organics for either 1-BuOH or BuOOH, as expected.

Fig. 6.2 (c, d) show examples of PE spectra with combined O 1s, Na 2s, and I 4d signals from 0.12 M NaI aqueous solutions as a function of the 1-BuOH (c) and BuOOH (d) concentration (at mole fractions of 0 and 0.008) taken at a nominal photon energy of 450 eV and making use of the 2nd order light components to obtain O 1s signals in the same kinetic energy (KE) window. The trend of decreasing Na 2s and I 4d signals with increasing organic mole fraction is comparable to that of the corresponding Br^- solutions.

At the photon energies used in the present experiments, 229 eV and 450 eV, the photoionization cross section for the excitation of the Na 2s core level is relatively low, so that the analysis of sodium is affected by a larger error (Yeh and Lindau 1985).

The C 1s PE signal (left axis) of 0.12 M NaBr and 0.12 M NaI solutions, each mixed with 1-BuOH or BuOOH in the mole fraction range of 0.001 to 0.008 as well as their corresponding surface excess (right axis) in the absence of salt are both shown in Fig. 6.3. The surface excess, derived from surface tension measurements (Donaldson and Anderson 1999), indicates that both surface active organic compounds exhibit saturated surface excess above 0.002 mole fraction, which seems also to be confirmed by the XPS measurements. Note that XPS probes deeper than just the topmost surface layer, so that the signal also contains a contribution from bulk solute molecules. The latter increases linearly with the bulk concentration, which explains the continuing increase of the photoemission signal even if the surface coverage levels off. Furthermore, the shape of the curvature of the C 1s signal does not exactly follow that of the surface excess. This may be attributed to a salting out effect on the organics exerted by the halide ions in solution, which is not reflected by the surface tension measurements. It seems that both Br^- and I^- ions are salting out BuOOH more than 1-BuOH based on the measured C 1s PE signals comparing to the evolution of the corresponding surface excess with the presence of salt. On one hand, according to Krisch et al.'s study (Krisch, D'Auria et al. 2007), their surface excess derived from their surface tension measurements of 1-BuOH solutions in presence of nearly saturated (thus high

molarity) KI concentrations, a significant salting out effect by KI was observed. The surface excess exhibited saturated surface excess below mole fraction 0.001 in the presence of KI. On the other hand, working at much lower salt concentrations, we don't see a difference in salting out of either 1-BuOH or BuOOH between the two halide ions.
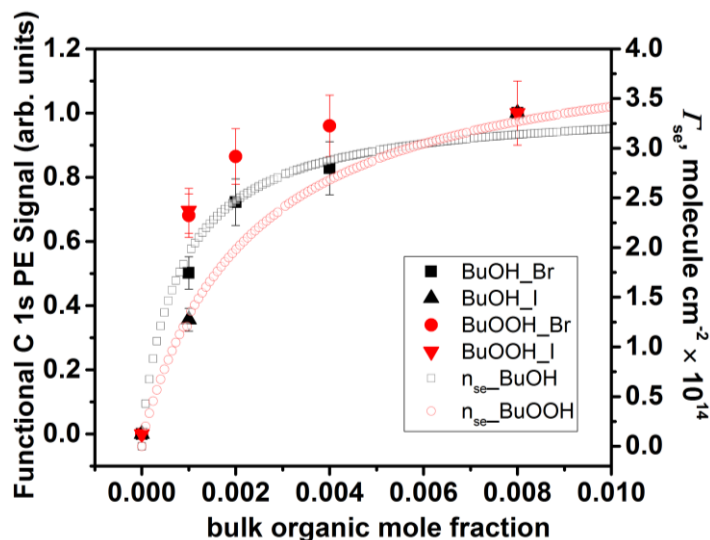

Fig. 6.3. Functional group C 1s PE signal taken at a photon energy of 458 eV (from the raw data as shown in Fig. 6.2 a, b) as a function of 1-BuOH/BuOOH concentration for aqueous solutions of 0.12 M NaBr and of 0.12 M NaI (left axis); and surface excess for aqueous solutions of 1-BuOH/BuOOH as a function of bulk concentration in water.

Fig. 6.4 (a) shows the relative departure of the bromide Br 3d photoemission signal from its value for the neat bromide solutions as a function of mole fraction of organics. The Br 3d signal is proportional to the interfacial concentration in the sense of the total amount of Br^- ions within a characteristic depth of about 1.2 nm from the surface (Thurmer, Seidel et al. 2013). In general, in the presence of 1-BuOH or BuOOH, we observe a distinct suppression of the PE signals for both Na, and Br, by about 15-25% and 15-45%, respectively, for 1-BuOH, and by about 20-50% and 30-40%, respectively, for BuOOH. It seems that BuOOH pushes the anion, Br^-, and the cation, Na^+ away from the interface more than 1-BuOH does. In addition, we did not see an apparent trend of the Br to Na integrated PE peak area ratio as a function of bulk organic concentration within the probe depth (data not shown).
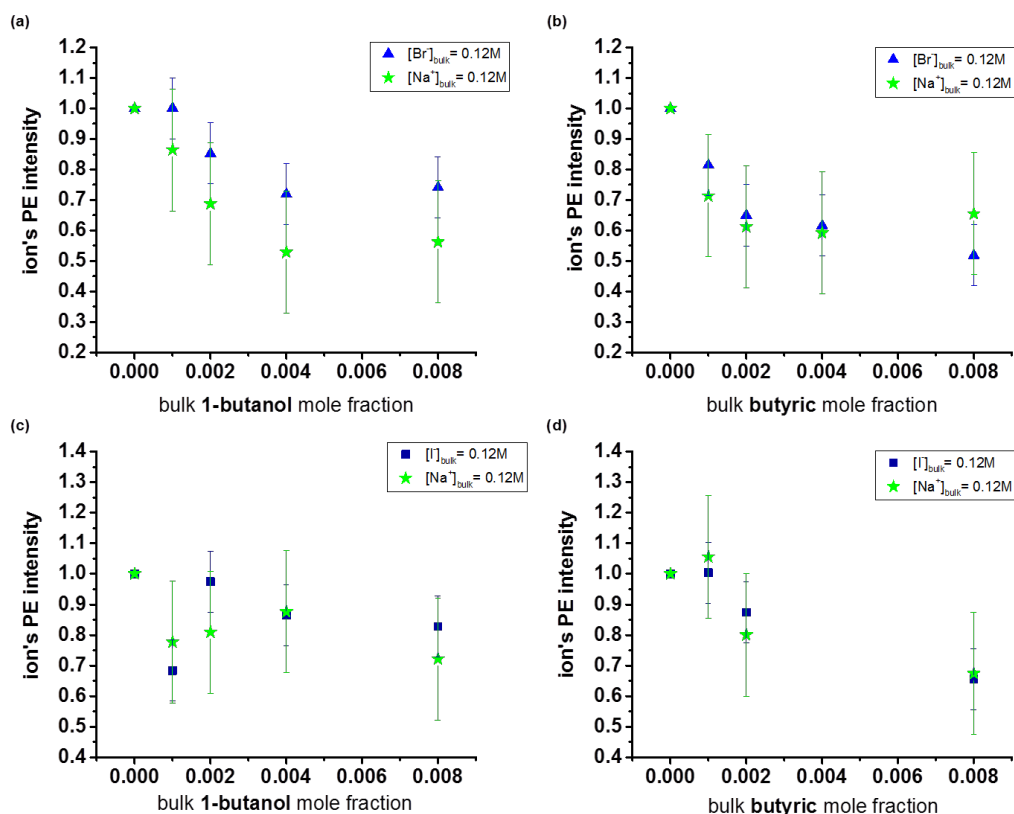
Fig. 6.4. (a, b): Relative change of Br 3d and Na 2s PE signals as a function of organics concentration for aqueous solutions of 0.12 M NaBr. (c, d): Relative change of I 4d and Na 2s PE signals as a function of organics concentration for aqueous solutions of 0.12 M NaI.

In Fig. 6.4 (c,d), the measured PE signals for the mixed organic-NaI solutions are plotted as relative departure of the I 4d and Na 2s PE signals measured at a photon energy of 450 eV from that of the neat NaI solution with the same NaI concentration as a function of the 1-BuOH and BuOOH concentration in the bulk. The I⁻ solutions with 1-BuOH exhibited a decrease of the I 4d signal by ca. 10-15% and of the Na 2s signal by ca. 10-30%, while with BuOOH the I 4d signal was observed to be depleted by ca. 10-35%, and Na 2s by ca. 10-30%, both when compared to the I⁻ solutions without organics present. Similar to the case of the Br⁻ solutions, it seems that butyric acid displaces the anion, iodide, away from the interface more strongly than 1-BuOH. The relative change of the I to Na elemental ratio obtained from the ratio of the I 4d to Na 2s integrated peak area ratio normalized to that for the neat salt solution in absence of organics did not show a clear trend with increasing organic content (not shown). Krisch et al. (Krisch, D'Auria et al. 2007) observed a decrease in the I to K ratio in presence of 1-BuOH at 200 eV KE and around 450 eV KE compared to the neat solution in absence of 1-BuOH, though at much higher KI concentrations.

6.4.2. MD simulation results

To obtain further insight into the above-described behavior of Br¯ and I¯ in the presence of 1-BuOH/BuOOH, we performed MD simulations of the solutions studied here. The simulations were initiated by the group of Martina Roeselová, Institute of Organic Chemistry and Biochemistry, academy of sciences of the Czech Republic and performed by M. Khabiri. Fig. 6.5 a,c show the averaged density profiles of halide anions along the normal to the liquid−vapor interface for the neat solutions in absence of organics.
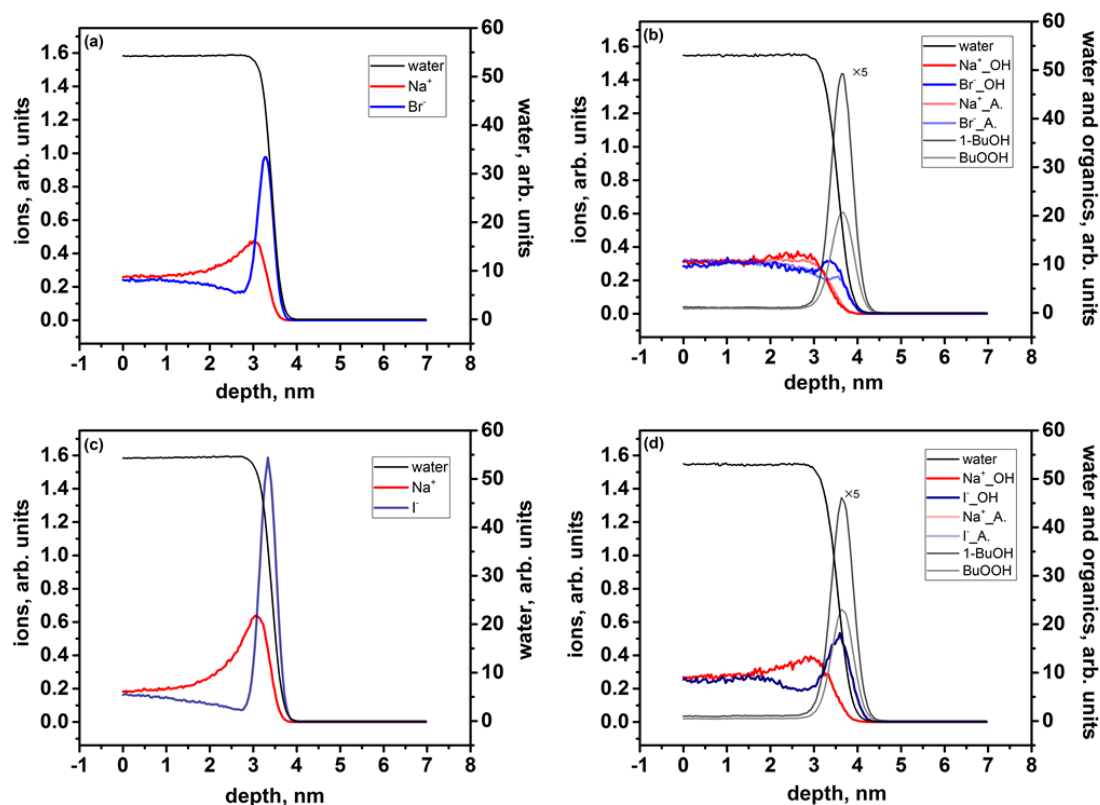
Fig. 6.5. (a) Density profile of Br (blue), Na (red), and water (black) atoms of aqueous 0.12 M NaBr solution. (b) Density profile of Br (blue with 1-BuOH; light blue with BuOOH), Na (red with 1-BuOH; light red with BuOOH), and water (black) atoms of aqueous 0.12 M NaBr solution in the presence of 1-BuOH (grey) or BuOOH (light grey). (c) Density profile of I (navy), Na (red), and water (black) atoms of aqueous 0.12 M NaI solution. (d) Density profile of I (navy with 1-BuOH; light navy with BuOOH), Na (red with 1-BuOH; light navy with BuOOH), and water (black) atoms of aqueous 0.12 M NaI solution in the presence of 1-BuOH (grey) or BuOOH (light grey).

Both I¯ and Br¯ ions display a significant surface affinity with high density at the interface with a layer of enhanced Na ion density underneath, which is accompanied by a depletion zone of the halide ions below the interface. For both solution types, the effect of the organics

is to suppress the density of the halide ions at the interface, Br⁻ being more affected than iodide, and BuOOH having a slightly stronger suppressing effect than 1-BuOH (Fig. 6.5 b,d). It seems that also in presence of both 1-BuOH and BuOOH, both halide ions remain enhanced at the outermost surface in comparison to the Na cations. The somewhat larger near-surface peak of I⁻ is accompanied by an also larger Na⁺ ion peak underneath to equilibrate the overall charge of the bilayer.

In order to compare the density profiles returned by the MD simulations with the XPS data, the density profiles were integrated in a similar way as presented by Krisch et al. (Krisch, D'Auria et al. 2007). They used an approach wherein electron attenuation in the solution was modeled by a simple exponential decay with respect to the depth into solution, as described in the (E 6.1):

$$S(\text{KE}) = \int\limits_{+\infty}^{z(\rho_{50\%})} \rho(z)dz + \int\limits_{z(\rho_{50\%})}^{-\infty} \rho(z)e^{-z/\text{IMFP(KE)}}\,dz \qquad (\text{E 6.1})$$

S denotes a relative photoemission signal obtained from electrons with a given kinetic energy, KE, ρ (z) is the density profile of the core level (photo)electrons of each atom contributing to S, z is the distance from a dividing plane placed at the position where the total density reaches half of its maximum value ($\rho_{50\%}$), and IMFP (KE), is the KE-dependent inelastic mean free path of the photoelectrons. The first term is the integral of all surface components lying above the dividing plane for the neat solution z ($\rho_{50\%}$) = 3.4 nm, while for the other solutions z ($\rho_{50\%}$) = 3.8 or 3.7 nm (corresponding to the x-axis in Fig. 6.5) in the presence of 1-BuOH of BuOOH respectively. Above z ($\rho_{50\%}$) the density is at most 50 % of its bulk value ($\rho_{50\%}$); therefore, attenuation of photoelectrons originating from this region is neglected in this simplified approach. The second term describes the exponential attenuation of photoelectrons originating from atoms in the bulk with the density profiles derived from the MD simulation.

The results, depicted in Fig. 6.6 a (for Br⁻) and b (for I⁻) show the relative departure of the normalized simulated photoemission signal using equation (E 6.1), derived from the density profile of ions from their value for the neat halide-solutions as a function organics. The LJ-XPS results for the corresponding solutions are plotted as hollow symbols in both panels. PE signals for sodium, Br⁻, and I⁻ at the interface, observed in the aqueous salt solution, were decreasing with increasing bulk 1-BuOH or BuOOH concentration in general. The reduction

is more apparent in the presence of BuOOH than 1-BuOH. Qualitatively, this suppression effect also becomes apparent in the simulated signals derived from the MD simulations. At a more quantitative level, differences in the relative effects of 1-BuOH and BuOOH on Br⁻ and I⁻ between simulated and measured signals become apparent. However, it should be noted that on the one hand there is significant scatter in the experimental data, especially for the I⁻ solutions, and on the other hand the simulations rely heavily on simplified assumptions regarding electron scattering in the strongly structured interface.
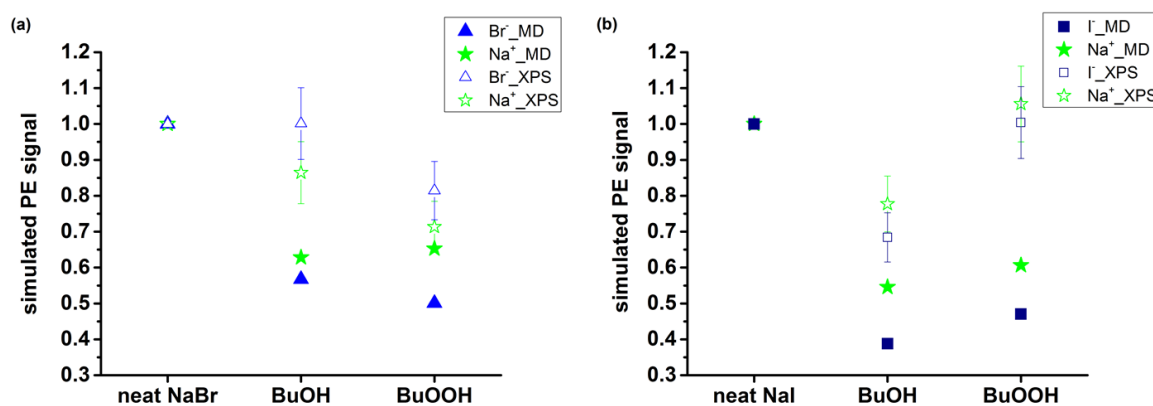
Fig. 6.6. (a) Normalized changes to the simulated photoemission signal, S, of Br⁻ (blue triangle), Na⁺ (green star) of aqueous 0.12 M NaBr solution as a function of functional group of organics with bulk concentrations of 0.12 M as derived from the MD simulations using equation (E 6.1). (b) Normalized changes to the simulated photoemission signal, S, of I⁻ (navy square), sodium (green star) of aqueous 0.12 M NaI solution as a function of functional group of organics with bulk concentration 0.12 M as derived from the MD simulations using equation (E 6.1). The hollow symbols denote the experimental results for the corresponding solutions in both panel (a) and (b).

6.5. Discussion

We observed experimentally that the surface-active organic 1-BuOH and BuOOH can suppress the enhancement of both anions (Br⁻, I⁻) and cations (Na⁺) at the interface. The changing profile may be due to the fact that the alcohol/acid molecules simply occupy the free water surface, so that ions are displaced away from the vapor−organic interface eventually interacting specifically with the alcohol or carboxyl groups on the bulk side of the interface. Therefore, the question arises whether the halide ions simply lose the competition against the surfactants or whether there is something (i.e., the specific interactions) counteracting that. In order to check this for the Br⁻ solutions, where the suppressing effect was more pronounced, and the Br 3d PE signals were considered as a function of the surface

area not occupied by the surfactant. This free surface area was estimated by $X = 1 - (C\ 1s/C\ 1s_{max})$; where X is the fraction of free surface area, C 1s being the photoemission signal of the surfactant head group carbon representing the surface coverage and $C\ 1s_{max}$ being the maximum C 1s signal measured at the highest organic concentration, where the surfactant was likely occupying a full monolayer. Thus the highest organic concentration corresponds to $X = 0$ (no free water surface); the lowest (organics = 0, neat solution) $X = 1$. The corresponding plot of the Br 3d PE signal against X is shown in Fig. 6.7.
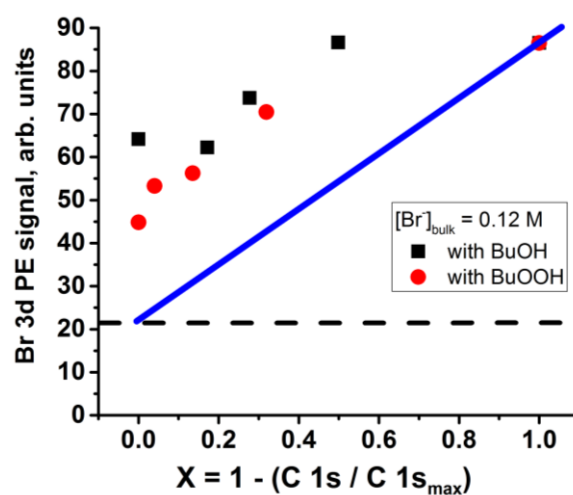
Fig. 6.7. Br 3d PE signals against the surface area not consumed by surface active organics. The photoemission signal also contains a contribution by the solutes present in the bulk. This contribution was estimated by partial integration of the Br density profile according to equation (E 6.1) from 0 to 3nm, which amounted to 25% of the total Br signal. Thus, if the bulk contribution remains independent of the presence of the surfactant and if the surface coverage of Br⁻ would linearly correlate with the free water surface area, we would expect the data points on a straight line (the blue line shown in the plot) passing through the observed Br signal at $X = 1$ and offset at the y-axis by 25 %.

Deviations below or above the line towards $X = 0$ would indicate additional repulsion or attraction, respectively, towards the interface due to the organics. Thus, for both, 1-BuOH and BuOOH, about twice as much Br⁻ is present as expected from the amount of free water surface area estimated via X. This could be due to the fact that even for $X = 0$, a substantial amount of free interfacial water is available in-between the organics to accommodate Br⁻ ions or that there are specific interactions between Br⁻ and alcohol- and carboxyl head groups. Further information on this aspect may be obtained from a future more detailed analysis of the MD simulation results in terms of radial density profiles of the ions to obtain statistical information on their nearest neighbors as a function of depth.

6.6. Conclusion

The photoelectron spectroscopic investigation of the ternary solutions by LJ-XPS demonstrates that 1-butanol and butyric acid exhibit surfactant behavior in line with known surface excess and both suppress Br^- and I^- at the interface. The abundance of the sodium cations also decreased in presence of both organic compounds. Complimentary MD simulations of the same solutions are qualitatively consistent with the experimental observation. The results also indicate that more halide ions remain in the interfacial region than expected from simple competition with the surfactant molecules for surface area. These subtle effects of an organic surfactant on the changing structure at the interface do not allow to conclusively clarify the role of organics on interfacial reactivity.

Acknowledgments

References

Abbatt, J. P. D., J. L. Thomas, K. Abrahamsson, C. Boxe, A. Granfors, A. E. Jones, M. D. King, A. Saiz-Lopez, P. B. Shepson, J. Sodeau, D. W. Toohey, C. Toubin, R. von Glasow, S. N. Wren and X. Yang (2012). "Halogen activation via interactions with environmental ice and snow in the polar lower troposphere and other regions." Atmospheric Chemistry and Physics **12**(14): 6237-6271.

Berendsen, H. J. C., J. R. Grigera and T. P. Straatsma (1987). "THE MISSING TERM IN EFFECTIVE PAIR POTENTIALS." Journal of Physical Chemistry **91**(24): 6269-6271.

Brown, M. A., R. D'Auria, I. F. W. Kuo, M. J. Krisch, D. E. Starr, H. Bluhm, D. J. Tobias and J. C. Hemminger (2008). "Ion spatial distributions at the liquid-vapor interface of aqueous potassium fluoride solutions." Physical Chemistry Chemical Physics **10**(32): 4778-4784.

Brown, M. A., M. Faubel and B. Winter (2009). "X-Ray Photo- and Resonant Auger-Electron Spectroscopy Studies of Liquid Water and Aqueous Solutions." Annual Reports Section "C" (Physical Chemistry) **105**(0): 174-212.

Brown, M. A., A. B. Redondo, I. Jordan, N. Duyckaerts, M.-T. Lee, M. Ammann, F. Nolting, A. Kleibert, T. Huthwelker, J.-P. Maechler, M. Birrer, J. Honegger, R. Wetter, H. J. Woerner and J. A. van Bokhoven (2013). "A new endstation at the Swiss Light Source for ultraviolet photoelectron spectroscopy, X-ray photoelectron spectroscopy, and X-ray absorption spectroscopy measurements of liquid solutions." Review of Scientific Instruments **84**(7).

Brown, M. A., F. Vila, M. Sterrer, S. Thuermer, B. Winter, M. Ammann, J. J. Rehr and J. A. van Bokhoven (2012). "Electronic Structures of Formic Acid (HCOOH) and Formate (HCOO-) in Aqueous Solutions." Journal of Physical Chemistry Letters **3**(13): 1754-1759.

Caleman, C., J. S. Hub, P. J. van Maaren and D. van der Spoel (2011). "Atomistic simulation of ion solvation in water explains surface preference of halides." Proceedings of the National Academy of Sciences of the United States of America **108**(17): 6838-6842.

Carpenter, L. J., S. M. MacDonald, M. D. Shaw, R. Kumar, R. W. Saunders, R. Parthipan, J. Wilson and J. M. C. Plane (2013). "Atmospheric iodine levels influenced by sea surface emissions of inorganic iodine." Nature Geoscience **6**(2): 108-111.

Chang, T. M. and L. X. Dang (2006). "Recent advances in molecular simulations of ion solvation at liquid interfaces." Chemical Reviews **106**(4): 1305-1322.

Clifford, D. and D. J. Donaldson (2007). "Direct experimental evidence for a heterogeneous reaction of ozone with bromide at the air-aqueous interface." Journal of Physical Chemistry A **111**(39): 9809-9814.

Dang, L. X. and T. M. Chang (2002). "Molecular mechanism of ion binding to the liquid/vapor interface of water." Journal of Physical Chemistry B **106**(2): 235-238.

Donaldson, D. J. and D. Anderson (1999). "Adsorption of atmospheric gases at the air-water interface. 2. C-1-C-4 alcohols, acids, and acetone." Journal of Physical Chemistry A **103**(7): 871-876.

Donaldson, D. J. and C. George (2012). "Sea-Surface Chemistry and Its Impact on the Marine Boundary Layer." Environmental Science & Technology **46**(19): 10385-10389.

Faubel, M., B. Steiner and J. P. Toennies (1997). "Photoelectron Spectroscopy of Liquid Water, Some Alcohols, and Pure Nonane in Free Micro Jets." Journal of Chemical Physics **106**(22): 9013-9031.

Flechsig, U., F. Nolting, A. F. Rodriguez, J. Krempasky, C. Quitmann, T. Schmidt, S. Spielmann and D. Zimoch (2010). "Performance Measurements at the SLS SIM Beamline." AIP Conference Proceedings 1234: 319-322.

Ghosal, S., M. A. Brown, H. Bluhm, M. J. Krisch, M. Salmeron, P. Jungwirth and J. C. Hemminger (2008). "Ion Partitioning at the Liquid/Vapor Interface of a Multicomponent Alkali Halide Solution: A Model for Aqueous Sea Salt Aerosols." Journal of Physical Chemistry A **112**(48): 12378-12384.

Ghosal, S., J. C. Hemminger, H. Bluhm, B. S. Mun, E. L. D. Hebenstreit, G. Ketteler, D. F. Ogletree, F. G. Requejo and M. Salmeron (2005). "Electron spectroscopy of aqueous solution interfaces reveals surface enhancement of halides." Science **307**(5709): 563-566.

Hess, B., H. Bekker, H. J. C. Berendsen and J. Fraaije (1997). "LINCS: A linear constraint solver for molecular simulations." Journal of Computational Chemistry **18**(12): 1463-1472.

Hess, B., C. Kutzner, D. van der Spoel and E. Lindahl (2008). "GROMACS 4: Algorithms for highly efficient, load-balanced, and scalable molecular simulation." Journal of Chemical Theory and Computation **4**(3): 435-447.

Hoover, W. G. (1985). "CANONICAL DYNAMICS - EQUILIBRIUM PHASE-SPACE DISTRIBUTIONS." Physical Review A **31**(3): 1695-1697.

Horinek, D., A. Herz, L. Vrbka, F. Sedlmeier, S. I. Mamatkulov and R. R. Netz (2009). "Specific ion adsorption at the air/water interface: The role of hydrophobic solvation." Chemical Physics Letters **479**(4-6): 173-183.

Horinek, D., S. I. Mamatkulov and R. R. Netz (2009). "Rational design of ion force fields based on thermodynamic solvation properties." Journal of Chemical Physics **130**(12).

Huang, Z., W. Hua, D. Verreault and H. C. Allen (2013). "Influence of Salt Purity on Na+ and Palmitic Acid Interactions." Journal of Physical Chemistry A **117**(50): 13412-13418.

Huang, Z., W. Hua, D. Verreault and H. C. Allen (2013). "Salty Glycerol versus Salty Water Surface Organization: Bromide and Iodide Surface Propensities." Journal of Physical Chemistry A **117**(29): 6346-6353.

Hunt, S. W., M. Roeselova, W. Wang, L. M. Wingen, E. M. Knipping, D. J. Tobias, D. Dabdub and B. J. Finlayson-Pitts (2004). "Formation of molecular bromine from the reaction of ozone with deliquesced NaBr aerosol: Evidence for interface chemistry." Journal of Physical Chemistry A **108**(52): 11559-11572.

Ishiyama, T. and A. Morita (2007). "Molecular dynamics study of gas-liquid aqueous sodium halide interfaces. I. Flexible and polarizable molecular modeling and interfacial properties." Journal of Physical Chemistry C **111**(2): 721-737.

Jorgensen, W. L., D. S. Maxwell and J. TiradoRives (1996). "Development and testing of the OPLS all-atom force field on conformational energetics and properties of organic liquids." Journal of the American Chemical Society **118**(45): 11225-11236.

Jungwirth, P. and D. J. Tobias (2001). "Molecular structure of salt solutions: A new view of the interface with implications for heterogeneous atmospheric chemistry." Journal of Physical Chemistry B **105**(43): 10468-10472.

Jungwirth, P. and D. J. Tobias (2006). "Specific ion effects at the air/water interface." Chemical Reviews **106**(4): 1259-1281.

Ketteler, G., P. Ashby, B. S. Mun, I. Ratera, H. Bluhm, B. Kasemo and M. Salmeron (2008). "In situ photoelectron spectroscopy study of water adsorption on model biomaterial surfaces." Journal of Physics-Condensed Matter **20**(18).

Krisch, M. J., R. D'Auria, M. A. Brown, D. J. Tobias, J. C. Hemminger, M. Ammann, D. E. Starr and H. Bluhm (2007). "The effect of an organic surfactant on the liquid-vapor interface of an electrolyte solution." Journal of Physical Chemistry C **111**(36): 13497-13509.

Lee, M.-T., M. A. Brown, S. Kato, A. Kleibert, A. Tuerler and M. Ammann (2015). "Competition between Organics and Bromide at the Aqueous Solution-Air Interface as Seen from Ozone Uptake Kinetics and X-ray Photoelectron Spectroscopy." Journal of Physical Chemistry A **119**(19): 4600-4608.

Nose, S. (1984). "A MOLECULAR-DYNAMICS METHOD FOR SIMULATIONS IN THE CANONICAL ENSEMBLE." Molecular Physics **52**(2): 255-268.

Okur, H. I., J. Kherb and P. S. Cremer (2013). "Cations Bind Only Weakly to Amides in Aqueous Solutions." Journal of the American Chemical Society **135**(13): 5062-5067.

Oldridge, N. W. and J. P. D. Abbatt (2011). "Formation of Gas-Phase Bromine from Interaction of Ozone with Frozen and Liquid NaCl/NaBr Solutions: Quantitative Separation of Surficial Chemistry from Bulk-Phase Reaction." Journal of Physical Chemistry A **115**(12): 2590-2598.

Onorato, R. M., D. E. Otten and R. J. Saykally (2010). "Measurement of Bromide Ion Affinities for the Air/Water and Dodecanol/Water Interfaces at Molar Concentrations by UV Second Harmonic Generation Spectroscopy." Journal of Physical Chemistry C **114**(32): 13746-13751.

Ottosson, N., M. Faubel, S. E. Bradforth, P. Jungwirth and B. Winter (2010). "Photoelectron spectroscopy of liquid water and aqueous solution: Electron effective attenuation lengths and emission-angle anisotropy." Journal of Electron Spectroscopy and Related Phenomena **177**(2-3): 60-70.

Petersen, P. B. and R. J. Saykally (2006). On the nature of ions at the liquid water surface. Annual Review of Physical Chemistry. **57:** 333-364.

Pruyne, J. G., M.-T. Lee, C. Fábri, A. Beloqui Redondo, A. Kleibert, M. Ammann, M. A. Brown and M. J. Krisch (2014). "Liquid–Vapor Interface of Formic Acid Solutions in Salt Water: A Comparison of Macroscopic Surface Tension and Microscopic in Situ X-ray Photoelectron Spectroscopy Measurements." The Journal of Physical Chemistry C.

Seah, M. P. and W. A. Dench (1979). "Quantitative electron spectroscopy of surfaces: a standard data base for electron inelastic mean free paths in solids." Surface and Interface Analysis **1**(1): 2-11.

Tang, C. Y. and H. C. Allen (2009). "Ionic Binding of Na+ versus K+ to the Carboxylic Acid Headgroup of Palmitic Acid Monolayers Studied by Vibrational Sum Frequency Generation Spectroscopy." Journal of Physical Chemistry A **113**(26): 7383-7393.

Thurmer, S., R. Seidel, M. Faubel, W. Eberhardt, J. C. Hemminger, S. E. Bradforth and B. Winter (2013). "Photoelectron Angular Distributions from Liquid Water: Effects of Electron Scattering." Physical Review Letters **111**(17).

Tobias, D. J. and J. C. Hemminger (2008). "Chemistry - Getting specific about specific ion effects." Science **319**(5867): 1197-1198.

Vazdar, M., E. Pluharova, P. E. Mason, R. Vacha and P. Jungwirth (2012). "Ions at Hydrophobic Aqueous Interfaces: Molecular Dynamics with Effective Polarization." Journal of Physical Chemistry Letters **3**(15): 2087-2091.

Winter, B. (2009). "Liquid microjet for photoelectron spectroscopy." Nuclear Instruments & Methods in Physics Research Section a-Accelerators Spectrometers Detectors and Associated Equipment **601**(1-2): 139-150.

Yeh, J. J. and I. Lindau (1985). "ATOMIC SUBSHELL PHOTOIONIZATION CROSS-SECTIONS AND ASYMMETRY PARAMETERS - 1 LESS-THAN-OR-EQUAL-TO Z LESS-THAN-OR-EQUAL-TO 103." Atomic Data and Nuclear Data Tables **32**(1): 1-155.

Chapter 7

7. Summary and Outlook

7.1. Summary

This PhD study has been conducted for a better understanding of heterogeneous kinetics of the reaction of O_3 with Br^- anions at the liquid−vapor interface. The reaction has been further investigated how such reactions are affected by the presence of various relevant organic compounds by measuring the kinetics of O_3 loss over solutions containing mixtures of NaBr and organics in a flow reactor.

In the past, the heterogeneous oxidation of halides has been suspected to involve a rate limiting step with an intermediate on the surface, based on observation of the loss of O_3 from the gas phase under different conditions. Truly assessing the nature of a surface-specific reaction, however, requires selectively probing the surface. Therefore, the key aspect in this work is to use *in situ* X-ray photoelectron spectroscopy (XPS) on liquid micro-jets (LJ) of the parent solutions, which directly provided the composition of inorganic and organic compounds in the aqueous phase at the aqueous liquid−vapor interface, thus, within the top-most molecular layers of the liquid with great chemical selectivity and sensitivity.

Based on this complementary set of approaches, extensive investigations have been made to better understand the reaction kinetics and molecular surface structure to assess the interplay between Br^- ions and citric acid, a proxy compound to represent a class of oxidized organic compounds at the ocean surface or contained in sea spray particles generated therefrom.

The kinetics of O_3 to neat NaBr solutions is found to be consistent with bulk reaction-limited uptake, in some contrast to previous results reported in the literature that were, though, obtained under slightly different conditions. In the presence of citric acid, bulk reaction-limited uptake is still a likely scenario, where the enhanced reactivity may be explained by an

acid-catalyzed mechanism (Liu, Schurter et al. 2001) and possibly an increase in the solubility of O_3 (Bin 2006). The uncertainty in the underlying kinetic parameters, however, leaves room for a surface reaction. The complementary LJ-XPS investigation of the same solutions demonstrated that citric acid exhibits weak surfactant behavior in line with known surface tension data and suppresses Br^- at the interface. In turn, interestingly, the abundance of the sodium cations at the interface increased with the presence of citric acid, possibly through specific interactions with the molecule's alcohol or carboxylic acid groups.

In another study, where the liquid−vapor interface for mixtures of water, and formic acid, an abundant chemical in the atmosphere, was examined, the results of LJ-XPS and surface tension measurements over a wide range of formic acid concentrations have been compared. A simple model replicating the XPS results is under the assumption that the surface excess was strictly contained in the top interfacial layer of the solution.

Moreover, the results of LJ-XPS measurements over a range of organic compounds, i.e. small alcohols, small carboxylic acids, or carboxylates (C1-C4) at 0.5 M bulk concentration have been compared with classic surface tension measurements. A linear correlation was found between the headgroup carbon 1s core-level signal intensity and the surface excess derived from literature values for the surface tension of each investigated compound. Furthermore, the C 1s PE signal intensity was also found to linearly correlate with the octanol-water partition coefficient, P, a hydrophobicity indicator (Valsaraj 1988). The excellent agreement demonstrates that the approach of LJ-XPS is a robust method to study the surface propensity of organic compounds at the liquid−vapor interface. LJ-XPS provided further information on the orientation of the surfactant molecules, and on the relative surface propensity of the carboxylic acids and their conjugate base carboxylate ions.

While the systematic investigation into the relationship between the XPS signals and surface excess served to form a better basis of the interpretation of the liquid jet XPS experiments, further experiments were also needed to address the ion specific effects observed with citric acid, a relatively complex compound with carboxyl and alcohol functions. Therefore, the contrasting effect of an alcohol and a carboxylic acid surfactant on the ion distribution at the aqueous liquid−vapor interface has been studied. The photoelectron spectroscopic investigation of the ternary solutions i.e. NaBr or NaI with 1-butanol or butyric acid by LJ-XPS demonstrated that in the presence of 1-butanol and butyric acid Br^- and I^- at the aqueous liquid−vapor interface are displaced to some degree. The adsorption of sodium also decreased

in the presence of both organic compounds. The experimental results were quantitatively compared with the molecular dynamics simulations performed by M. Khabiri of 1-butanol and butyric acid in similar aqueous halide solutions to develop a detailed understanding of the interfacial region of these ternary solutions. The density profiles resulting from the MD simulations have been integrated to obtain simulated photoemission signals, which turned out to be qualitatively consistent with the experimental results. A more detailed analysis is required for more quantitative comparison. In combination, the results so far indicated that in presence of 1-butanol and butyric acid more Br^- than expected (see Fig. 6.7). They remained at the interface based on the amount of water surface remaining free in presence of organics under sub-monolayer amounts.

The overall aim of this PhD work has been to obtain molecular level insight into halide liquid−vapor interfaces that can further our understanding of fundamental marine atmospheric chemistry as well as be used as input for quantitative atmospheric chemical models. In addition, the work has been particularly useful in expanding our knowledge of interfacial phenomena in the environment.

7.2. Outlook

In *Chapter 2*, the proof-of-principle measurements with our newly developed NAPP endstation with the implementation of the liquid microjet have demonstrated its wide applicability from UV photoemission to soft X-ray photoemission. However, the analyzer can cover kinetic energies up to 7000 eV. The NAPP endstation is prepared to fit to the PHOENIX beamline at SLS for X-ray energies between 2000 and 7000 eV, but has so far only be used in conjunction with solid samples (Kato, Ammann et al. 2015). However, due to geometric constraints, the spot size of the X-ray beam of the PHOENIX beamline at the point where the sample is placed in the NAPP endstation is a few mm, which is unfavorable for the operation of LJ-XPS, because a large volume of gas phase is probed as well leading to strong overlap of spectroscopic features originating from the gas and condensed phases. For this purpose, a refocusing mirror system has been built up and commissioned (not part of this thesis), which will allow LJ-XPS experiments at higher X-ray energies. High-energy measurements increase the probe depth of the experiment and allow for electronic structure measurements of bulk solutions and X-ray absorption spectroscopy (XAS) can also be utilized. For measuring photoemission at low KEs i.e. energy levels of valence electrons, it

would be worth to measure aqueous solutions by offline ultraviolet photoelectron spectroscopy (UPS) on a liquid micro-jet. For instance, bromine (4 p), exhibits a shallow electronic level at 8.8 eV BE, separated from the $1b_1$ level of liquid water (Winter and Faubel 2006), so that some aspects of the experiments studied in this thesis using soft X-rays could be investigated offline without a synchrotron.

Future experiments are also suggested that use a combination of near-ambient X-ray photoelectron spectroscopy (XPS) and sum-frequency generation (SFG) spectroscopy, a second-order (χ^2) non-linear optical technique. The spatial and temporal overlap of two intense ultra-short laser pulses, creates a light field at the sum-frequency of the two, which is detected to study the behavior of ions and organic matter as they co-adsorb at aqueous surfaces (see Fig. 7.1) (Gopalakrishnan, Liu et al. 2006, Yubo, Xin et al. 2009).
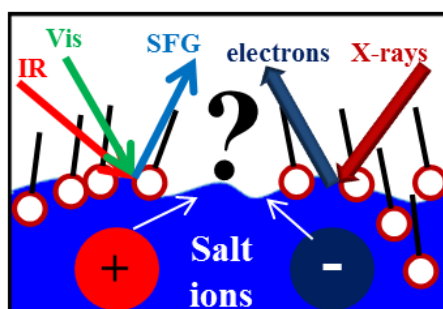
Fig. 7.1. The co-adsorption of ions with surface-active organic matter introduces several non-trivial contributions to the free energy of adsorption of the ions. By using XPS and SFG one can examine the structure of the interface.

On the one hand XPS gives direct information about the spatial distribution of various atomic sites relative to the interface; on the other hand SFG yields complementary information about the structure and orientation of various molecular functional groups, e.g. O-H groups of solvating water (Richmond 2002, Gopalakrishnan, Liu et al. 2006, Shen and Ostroverkhov 2006, Fan, Chen et al. 2009). Together, these experiments may provide molecular-level structural information of unprecedented detail about these highly complex but important and ubiquitous interfaces. By studying how the structure of these aqueous interfaces is evolving as function of the solution temperature this will furthermore unravel the much sought-after details on the thermodynamics of ionic surface hydration of mixed aqueous solutions comprised of both salts and organics relevant for marine aerosol or ocean surface water.

The heterogeneous reaction of O_3 with Br^- has been of significant interest in this thesis. It is believed to be involved in the O_3 depletion chemistry in the troposphere. The reaction of O_3 with Br^- at the aqueous liquid−vapor interface of environmental relevance has been suggested to go through charge-transfer complexes of O_3 as intermediates ($BrOOO^-$, of which the structure is thought to be linear) for HOBr production (Liu, Schurter et al. 2001). Reactions of O_3 with a wide range of organic compounds are also of essential importance for a wide range of other environmentally relevant systems (Shiraiwa, Sosedova et al. 2011). In this thesis, aqueous Br^- solutions were characterized by LJ-XPS, which provided insight into the competition between organic solutes and halide ions that can be put into the context of offline ozonolysis experiments. It would be promising to put these two aspects together. Future experiments are proposed to look at the *in situ* reaction between O_3 and Br^- *in-situ* spectroscopically by XPS with the liquid jet conducting the aqueous Br^- solution into the analysis chamber, with gaseous O_3 provided as background gas.

The application of *in-situ* LJ-XPS (see Fig. 7.2) would demonstrate the evolution of the surface chemistry while flowing O_3 over the liquid surface of a Br^- containing electrolyte. The obtained photoelectron spectra would reveal the nature of the molecular interactions and would display changes in the electronic structure of surface-bound Br and O atoms at the aqueous liquid−vapor interface *in situ* under relevant reaction conditions. Changes of the X-ray absorption spectra using partial electron yield (PEY-XAS, maintaining surface sensitivity) would be used as another experimental observable to address the local structure and to help in the identification of the reaction intermediate.
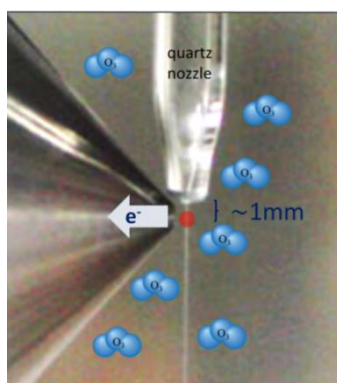

Fig. 7.2. Photograph of the liquid-microjet in action with a flow velocity of 10 m/s. The red spot represents the X-ray beam towards the reader hitting on the jet (continuously refreshed liquid sample). The arrow represents the ejected photoelectrons from the liquid surface. Gaseous O_3 (cartoon representation) is dosed as the background gas in the analyzer chamber.

Experiments as suggested above would also greatly benefit from the large number of other powerful and relevant techniques e.g. Fourier-transform infrared (FT-IR) spectroscopy /microscopy and mid-IR pump-probe spectroscopy. While these may provide a better understanding in terms of more chemical details and may thus also further our knowledge of the role of organics in the chemistry of halide solutions relevant for marine aerosol or ocean surface water, they clearly lack the surface sensitivity of XPS. Also in a broader context of atmospheric sciences, many essential processes involve phase transfer between the gas and the liquid phase or nucleation at solid−liquid or solid−liquid−gas interfaces, so that a detailed understanding of the interfaces with molecular level detail will remain an important niche in atmospheric chemistry.

References

Bin, A. K. (2006). "Ozone solubility in liquids." Ozone-Science & Engineering **28**(2): 67-75.

Fan, Y. B., X. Chen, L. J. Yang, P. S. Cremer and Y. Q. Gao (2009). "On the Structure of Water at the Aqueous/Air Interface." Journal of Physical Chemistry B **113**(34): 11672-11679.

Gopalakrishnan, S., D. F. Liu, H. C. Allen, M. Kuo and M. J. Shultz (2006). "Vibrational spectroscopic studies of aqueous interfaces: Salts, acids, bases, and nanodrops." Chemical Reviews **106**(4): 1155-1175.

Kato, S., M. Ammann, T. Huthwelker, C. Paun, M. Lampimaeki, M.-T. Lee, M. Rothensteiner and J. A. van Bokhoven (2015). "Quantitative depth profiling of Ce3+ in Pt/CeO2 by in situ high-energy XPS in a hydrogen atmosphere." Physical Chemistry Chemical Physics **17**(7): 5078-5083.

Liu, Q., L. M. Schurter, C. E. Muller, S. Aloisio, J. S. Francisco and D. W. Margerum (2001). "Kinetics and mechanisms of aqueous ozone reactions with bromide, sulfite, hydrogen sulfite, iodide, and nitrite ions." Inorganic Chemistry **40**(17): 4436-4442.

Richmond, G. L. (2002). "Molecular bonding and interactions at aqueous surfaces as probed by vibrational sum frequency spectroscopy." Chemical Reviews **102**(8): 2693-2724.

Shen, Y. R. and V. Ostroverkhov (2006). "Sum-frequency vibrational spectroscopy on water interfaces: Polar orientation of water molecules at interfaces." Chemical Reviews **106**(4): 1140-1154.

Shiraiwa, M., Y. Sosedova, A. Rouviere, H. Yang, Y. Zhang, J. P. D. Abbatt, M. Ammann and U. Poeschl (2011). "The role of long-lived reactive oxygen intermediates in the reaction of ozone with aerosol particles." Nature Chemistry **3**(4): 291-295.

Valsaraj, K. T. (1988). "On the Physicochemical Aspects of Partitioning of Non-Polar Hydrophobic Organics at the Air-Water-Interface." Chemosphere **17**(5): 875-887.

Winter, B. and M. Faubel (2006). "Photoemission from Liquid Aqueous Solutions." Chemical Reviews **106**(4): 1176-1211.

Yubo, F., C. Xin, Y. Lijiang, P. Cremer and G. Yi Qin (2009). "On the structure of water at the aqueous/air interface." Journal of Physical Chemistry B **113**(34): 11672-11679.

Acknowledgements

Many people supported this thesis by giving either scientific input or friendly support. Both parts were important, without them this work would not be completed. Thanks to every single one of you. Please forgive me if I forgot to mention you below.

- Andreas Türler for accepting me as a PhD student and for the interesting discussions on this thesis.
- Markus Ammann, for offering me the opportunity to work on this project in the Surface Chemistry group and for being my supervisor, furthermore for helpful discussions about data analyses, manuscript guidance, comments and corrections, and for the scientific input. I am sincerely thankful and am lucky to have such an excellent supervisor.
- Matthew A. Brown, for explanations of the LJ-XPS and for our fruitful cooperation.
- Hendrik Bluhm for reviewing this work.
- Martin Albrecht for accepting to act as the chairman of the thesis committee.
- Mario Birrer for the amazing technical support, your technical expertise in fixing all that we use and break, and making sure NAPP works.
- The whole surface chemistry group, past and present, for the nice working atmosphere. Here I would like to thank Sepp Schreiber and Thomas Ulrich, for helping me a lot in the beginning, and my office mates (OFLA/102), including Astrid Waldner, Xiangrui Kong and Pablo Corral-Arroyo (a very short time), for the pleasant time. I would also like to express my gratitude the following people: Thorsten Bartels-Rausch and Sarah Steimer, who taught me the usage of many instruments in our 2nd floor's Lab; Markus Lampimäki, whom I enjoyed talking to and taught me how to fit XPS peaks; Jacinta Edebeli and Anina Gilgen, who I have had only a short time to work, but was nice to meet both of you; Shunsuke Kato, who spent LJ beamtimes with me at SIM beamline; Goran Gržinić, who is my very good friend, shared your time with me, and provided me great help when I needed. I would like to give special thanks to Fabrizio Orlando, who spent countless LJ beamtime shifts with me at SIM. I thank you for not only the scientific insight, discussions, but also laugh and joke.

Curriculum Vitae

LEE, Ming-Tao

Personal data

Surname, First name:	Lee, Ming-Tao
Date of birth:	19.10.1982
Place of birth:	Taipei, Taiwan

Education

09/2002 – 06/2006
B.Sc., in Physics
Chinese Culture University, Taipei, Taiwan

08/2008 – 10/2010
M.Sc., in Material Physics and Nanotechnology
Linköping University, Linköping, Sweden
Thesis: "Plasmonic Enhanced Fluorescence using Gold Nanorods"

01/2012 – 10/2015
Ph.D., in Chemistry
University of Bern, Bern, Switzerland
Thesis: "The Role of Organics in the Chemistry at the Surface of Halide Solutions Relevant for Marine Aerosol or Ocean Surface Water"

Research Experience

01/2012 – 12/2015
PhD student,
Paul Scherrer Institute (PSI), Switzerland

01/2011 – 12/2011
Research Assistant,
Karlsruhe Institute of Technology (KIT), Germany

03/2008 – 07/2008
Research Assistant,
National Taiwan University Center for Condensed Matter Sciences, Taiwan

Conference contributions

Oral presentations

08/2014	Division of Colloid and Surface Chemistry at the 248th ACS National meeting, San Francisco, USA
12/2014	Surface Chemistry and Near-Ambient Pressure Photoemission; new tools and new paradigms at SOLEIL, Paris, France

Posters (as the presenter)

01/2014; 01/2015	SAOG: Swiss Working Group for Surface and Interface Science meeting, Fribourg, Switzerland
09/2013	Joint (SLS, SINQ, and SµS) Users' Meeting at PSI, Paul Scherrer Institut, Villigen Switzerland
04/2013	European Geosciences Union General Assembly, Vienna, Austria
01/2013	Rigi workshop: Thinking Big in a Small World: Creativity in the Molecular Sciences, Rigi Kulm, Switzerland

Teaching Experience

02/2013 – 05/2013; 02/2014 – 05/2014; 02/2015 – 05/2015	Teaching assistant at the University of Bern for practical courses in physical chemistry

Awards

01/2014	Best poster prize: Swiss Working Group for Surface and Interface Science meeting, Fribourg, Switzerland

Languages

- English (fluent)
- Swedish (basic)
- German (beginner)
- Chinese (mother tongue)

E r k l ä r u n g

gemäss Art. 28 Abs. 2 RSL 05

Name/Vorname:

Matrikelnummer:

Studiengang:

Bachelor ☐   Master ☐   Dissertation ☐

Titel der Arbeit:

LeiterIn der Arbeit:

Ich erkläre hiermit, dass ich diese Arbeit selbständig verfasst und keine anderen als die angegebenen Quellen benutzt habe. Alle Stellen, die wörtlich oder sinngemäss aus Quellen entnommen wurden, habe ich als solche gekennzeichnet. Mir ist bekannt, dass andernfalls der Senat gemäss Artikel 36 Absatz 1 Buchstabe r des Gesetzes vom 5. September 1996 über die Universität zum Entzug des auf Grund dieser Arbeit verliehenen Titels berechtigt ist. Ich gewähre hiermit Einsicht in diese Arbeit.

Ort/Datum

Unterschrift